SKI Report 2008:08

Research

Review of SKB's Work on Coupled THM Processes Within SR-Can

External review contribution in support of SKI's and SSI's review of SR-Can

Jonny Rutqvist
Chin-Fu Tsang

March 2008

ISSN 1104-1374
ISRN SKI-R-08/08-SE

SKI

SKI Report 2008:08

Research

Review of SKB's Work on Coupled THM Processes Within SR-Can

External review contribution in support of SKI's and SSI's review of SR-Can

Jonny Rutqvist
Chin-Fu Tsang

Lawrence Berkeley National Laboratory
Berkeley, California, USA

March 2008

FOREWORD

The work presented in this report is part of the Swedish Nuclear Power Inspectorate's (SKI) and the Swedish Radiation Protection Authority's (SSI) SR-Can review project.

The Swedish Nuclear Fuel and Waste Management Co (SKB) plans to submit a license application for the construction of a repository for spent nuclear fuel in Sweden 2010. In support of this application SKB will present a safety report, SR-Site, on the repository's long-term safety and radiological consequences. As a preparation for SR-Site, SKB published the preliminary safety assessment SR-Can in November 2006. The purposes were to document a first evaluation of long-term safety for the two candidate sites at Forsmark and Laxemar and to provide feedback to SKB's future programme of work.

An important objective of the authorities' review of SR-Can is to provide guidance to SKB on the complete safety reporting for the license application. The authorities have engaged external experts for independent modelling, analysis and review, with the aim to provide a range of expert opinions related to the sufficiency and appropriateness of various aspects of SR-Can. The conclusions and judgments in this report are those of the authors and may not necessarily coincide with those of SKI and SSI. The authorities own review will be published separately (SKI Report 2008:23, SSI Report 2008:04 E).

This report covers the review of issues on coupled thermal, hydrological and mechanical (THM) processes within SR-Can.

Bo Strömberg (project leader SKI) Björn Dverstorp (project leader SSI)

FÖRORD

Denna rapport är en underlagsrapport till Statens kärnkraftinspektions (SKI) och Statens strålskyddsinstituts (SSI) gemensamma granskning av Svensk Kärnbränslehantering AB:s (SKB) säkerhetsredovisning SR-Can.

SKB planerar att lämna in en ansökan om uppförande av ett slutförvar för använt kärnbränsle i Sverige under 2010. Som underlag till ansökan kommer SKB presentera en säkerhetsrapport, SR-Site, som redovisar slutförvarets långsiktiga säkerhet och radiologiska konsekvenser. Som en förberedelse inför SR-Site publicerade SKB den preliminära säkerhetsanalysen SR-Can i november 2006. Syftena med SR-Can är bl.a. att redovisa en första bedömning av den långsiktiga säkerheten för ett KBS-3-förvar vid SKB:s två kandidatplatser Laxemar och Forsmark och att ge återkoppling till SKB:s fortsatta arbete.

Myndigheternas granskning av SR-Can syftar till att ge SKB vägledning om förväntningarna på säkerhetsredovisningen inför den planerade tillståndsansökan. Myndigheterna har i sin granskning tagit hjälp av externa experter för oberoende modellering, analys och granskning. Slutsatserna i denna rapport är författarnas egna och överensstämmer inte nödvändigtvis med SKI:s eller SSI:s ställningstaganden. Myndigheternas egen granskning publiceras i en annan rapport (SKI Rapport 2008:19; SSI Rapport 2008:04).

Denna rapport redovisar granskningen av frågor kring kopplade termiska, hydrologiska och mekaniska (THM) processer inom SR-Can.

Bo Strömberg (projektledare SKI) Björn Dverstorp (projektledare SSI)

SUMMARY

In this report, we scrutinize the work by the Swedish Nuclear Fuel and Waste Management Company (SKB) related to coupled thermal, hydrological and mechanical (THM) processes within the SR-Can project. SR-Can is SKB's preliminary assessment of long-term safety for a KBS-3 nuclear waste repository, and is a preparation stage for the SR-Site assessment, the report that will be used in SKB's application for a final repository. We scrutinize SKB's work related to THM processes through review and detailed analysis, using an independent modeling tool. The modeling tool is applied to analyze coupled THM processes at the two candidate sites, Forsmark and Laxemar, using data defined in SKB's site description models for respective sites. In this report, we first provide a brief overview of SKB's work related to analysis of the evolution of coupled THM processes as presented in SR-Can, as well as supporting documents. In this overview we also identify issues and assumptions that we then analyze using our modeling tool. The overview and subsequent independent model analysis addresses issues related to near-field behavior, such as buffer resaturation and the evolution of the excavation-disturbed zone, as well as far-field behavior, such as stress induced changes in hydrologic properties.

Based on the review and modeling conducted in this report, we conclude by identifying a number of areas of weaknesses, where we believe further work and clarifications are needed. Some of the most important ones are summarized below:

1) We found that SKB's calculation of peak temperature might not have been conducted for the most conservative case—of extreme drying of the buffer under dry rock conditions and an unexpectedly high thermal diffusion coefficient. Our alternative analysis indicates that temperatures close to 100°C might be achieved under unfavorable (and perhaps unexpected) conditions in which the buffer is dried to below 20% near the canister. We believe SKB should conduct further analyses to show that such extreme drying of the buffer to below 20% could not occur, or that such drying would not result in a peak temperature higher than 100°C.

2) We found that SKB's estimates for the time of full resaturation of the buffer might be underestimated, because the analysis is based on models assuming nearby water-feeding conditions. Moreover, SKB's analysis does not consider the potential impact and uncertainties regarding water-retention properties of the rock mass and the potential impact of ventilation-induced drying during the operational phase is not addressed. SKB's estimated time to full resaturation is valid for an assumed distance to water feeding boundary of 12 m and for one single assumed retention curve of the rock. We believe SKB should provide additional analyses to show that the assumed distance to the water-feeding boundary is reasonable and conduct additional sensitivity analyses on water-retention properties and ventilation effects.

3) We found that SKB's reliance on the backfill as an important source for water supply to resaturate the buffer, in the case of extremely dry rock conditions, may be unjustified. If a bentonite-rock mixture (30/70) is used, the buffer may be resaturated by water supply from the backfill, but then the saturation in the backfill would

decrease, preventing it from swelling and thereby keeping it from fulfilling an important safety function indicator criterion. If Friedland Clay is used as backfill, its capillary suction at emplacement would be higher than that of the buffer, and therefore water would be sucked from the buffer into the backfill, effectively keeping the buffer dry. We believe SKB should conduct further studies or reconsider the backfill design, to assure buffer resaturation from the backfill in the case of extremely dry rock conditions.

4) We found that SKB's geomechanical analysis of the potential for rock-mass failure correctly identifies a high potential for spalling failure around the deposition holes at both Laxemar and Forsmark. However, a strong potential for tensile failure in the rock wall of tunnels and its consequence—forming a continuous damaged zone along the tunnels—is not identified. Moreover, SR-Can does not address the possibility of long-term time-dependent degradation of rock-strength parameters. SKB's assumption that the long-term strength is equal to the relatively short-term strength observed in *in situ* experiments might not be sufficiently conservative. We believe SKB needs to address the issue of time-dependence in the mechanical parameters as a part of their safety assessment.

5) We found that SKB correctly identifies possible stress-induced changes in permeability near excavations, as well as thermal-mechanically induced change in the far-field permeability. However, SKB analysis does not consider the possibility of large-scale shear reactivation in the far field. Many fractures at the site might already critically stressed for shear. During the thermal period, shear stresses around the repository will increase. We believe that SKB needs to evaluate potential permeability changes due to such shear reactivation and their importance for radionuclide transport.

Modeling results developed by the SKB and in this report involve application of complex coupled-processes modeling. An independent analysis using a different model simulator than SKB, is necessary for an in-depth check of SKB's results, to identify issues that might have been overlooked, to test assumptions, and to evaluate how sensitive their results are to such assumptions. The results presented in this report are related to SR-Can, but should also be considered by the SKB when defining their work scope on coupled THM processes for the upcoming SR-Site assessment. Thus, further site-specific analyses on these important aspects for the performance assessment of the future Swedish deep geological disposal of spent nuclear fuel should be conducted.

TABLE OF CONTENTS

1 INTRODUCTION 1

2 RELEVANT SAFETY-FUNCTION INDICATORS....4

3 OVERVIEW OF SKB'S ANALYSIS OF THE THM EVOLUTION 5

3.1 SKB's modeling tools 5

3.2 Thermal evolution and peak temperature 5

3.3 Hydrological evolution and resaturation time....7

3.4 Mechanical evolution, EDZ, and rock spalling around openings 12

3.5 THM-induced fracture reactivation and permeability change 14

4 ANALYSIS OF NEAR-FIELD THM BEHAVIOR....18

4.1 Finite element discretization and material properties 18

4.2 Modeling sequences, boundary and initial conditions 25

4.3 Approach and parameters for mechanical failure analysis 28

4.4 Results for an ideal base case....29
4.4.1 Temperature evolution and maximum temperature 29
4.4.2 Evolution of buffer saturation and fluid pressure 30
4.4.3 Evolution of stress in the buffer....30
4.4.4 Evolution of stress in the rock and possible failure 31

4.5 Case of extremely low rock permeability 42
4.5.1 Temperature evolution and maximum temperature....42
4.5.2 Evolution of buffer saturation and fluid pressure 42
4.5.3 Evolution of stress in the buffer....43
4.5.4 Evolution of stress in the rock and possible failure 44

4.6 Variation of distance to water feeding boundary....51

4.7 Effect of rock permeability on resaturation time 52

4.8 Variation of retention and relative permeability of the rock....54
4.8.1 Variation of retention curve of the rock....54
4.8.2 Variation of relative permeability of the rock....56

4.9 Case of high (intact) rock-mass modulus....58

4.10 Variation of thermal diffusion coefficient 62

4.11 Peak temperature for an extreme case of dry rock and high vapor diffusion coefficient 63

4.12 Case of optimum tunnel orientation relative to stress field at Laxemar 65

4.13 Extreme case of near isotropic horizontal stress at Forsmark 67

4.14 Extreme case of very anisotropic horizontal stress at Forsmark 69

4.15 Impact of backfill properties—30/70 vs Friedland Clay 71

4.16 Resaturation from water-bearing fractures in low-permeability rock 74
4.16.1 Vertical fracture intersecting the backfilled tunnel 75
4.16.2 Horizontal fracture intersecting the deposition hole 78

5 FRACTURE REACTIVATION AND PERMEBILITY CHANGE 80

5.1 Potential permeability changes with changes in normal stress across fractures 80

5.2 Potential for permeability change by shear reactivation along fractures 85

5.3 Estimating overall changes in permeability by fracture reactivation 88

6 SUMMARY OF RESULTS AND DISCUSSION 89

6.1 Thermal evolution and peak temperature 89

6.2 Hydrological evolution and resaturation time 89

6.3 Mechanical evolution, EDZ and rock spalling around openings 90

6.4 THM induced fracture reactivation and permeability change 91

7 CONCLUSIONS 93

8 REFERENCES 96

APPENDIX A: DESCRIPTION OF THE ROCMAS CODE 99

A1 THE ROCMAS CODE 99

A1.1 Basic approach and assumptions 99

A1.2 General Balance Equations 99

A1.3 Constitutive equations and constraints 100

A1.4 Field equations and solution approach 102

A2 REFERENCES 103

APPENDIX B: VALIDATION AND CALIBRATION OF THE BENTONITE MODEL AGAINST LABORATORY EXPERIMENTS ON MX-80 BENTONITE 105

B1 INTRODUCTION 105

B2 BENTONITE PROPERTIES USED BY SKB 105

B3 MODELING OF SMALL-SCALE LABORATORY TESTS 107

B3.1 Water uptake test 107

B3.2 Thermal gradient tests 107

B3.3 Swelling pressure test 107

B4 MODELING OF CEA MOCK-UP TEST 108

B4.1 Experimental setup 108

B4.2 Bentonite properties 108

B5 Summary and conclusions 109

B6 REFERENCES 110

1 INTRODUCTION

In this report, we scrutinize the work by the Swedish Nuclear Fuel and Waste Management Company (SKB) related to coupled thermal, hydrological and mechanical (THM) processes within the SR-Can project. SR-Can is SKB's assessment of long-term safety for a KBS-3 nuclear waste repository, and is a preparation stage for the SR-Site assessment, the report that will be used in SKB's application for a final repository. The assessment is conducted for the KBS-3 disposal concept (Figure 1-1 and 1-2) using preliminary data from the Forsmark and Laxemar sites, which are presently being investigated by SKB as candidates for a KBS-3 repository.

Coupled THM processes relevant to the performance of a geological nuclear waste repository include thermally driven stress changes, resaturation of the buffer, and THM-induced evolution hydrological properties within both the excavation-disturbed zone (EDZ) and in the far-field fractured rock mass. Resaturation of the buffer after its emplacement in a deposition hole is an important process for the protective function of the buffer. The resaturation process would ideally take place uniformly to assure that the bentonite swells uniformly to prevent high and uneven stressing of the waste canister. Moreover, development of swelling pressure can provide a support load against tunnel walls and the EDZ that can thereby help to prevent rock fall and so-called rock spalling failure of the excavation walls. Ideally, the buffer should be fully resaturated and swelled before the thermal peak, i.e. before the thermal rock stresses are the highest. An elevated temperature prevailing for thousands of years will also induce substantial stress changes in the far field, extending several hundred meters above and below the repository. Such stress changes will act on the existing fracture network, leading to changes in the permeability field. SKB has to assess the importance of such coupled THM processes on the safety of a KBS-3 repository at both Forsmark and Laxemar.

In this report, we scrutinize SKB's work related to THM processes through review and detailed analysis, using an independent modeling tool. The model is applied to analyze coupled THM processes at both Forsmark and Laxemar sites, using data defined in SKB's site descriptive models for respective sites. The purpose of this modeling is not just to verify SKB's analyzes of THM processes, but to identify issues that might have been overlooked, to test assumptions, and to evaluate how sensitive their results are to such assumptions. We conclude by identifying areas of weaknesses, where we believe that further work and clarifications are needed.

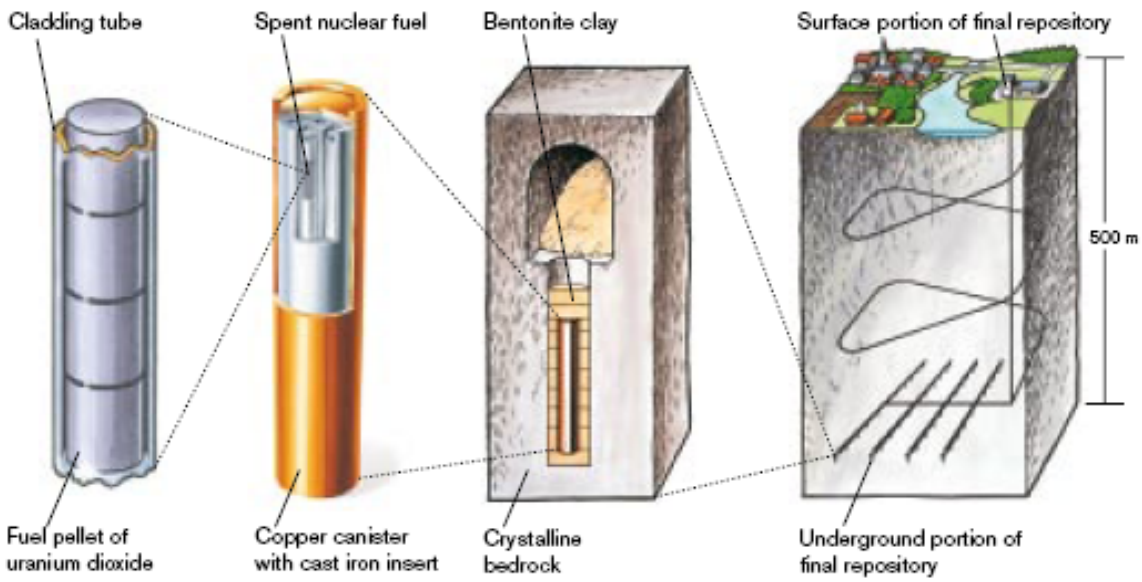

Figure 1-1. KBS-3V concept for disposal of spent nuclear fuel (SKB 2006a).

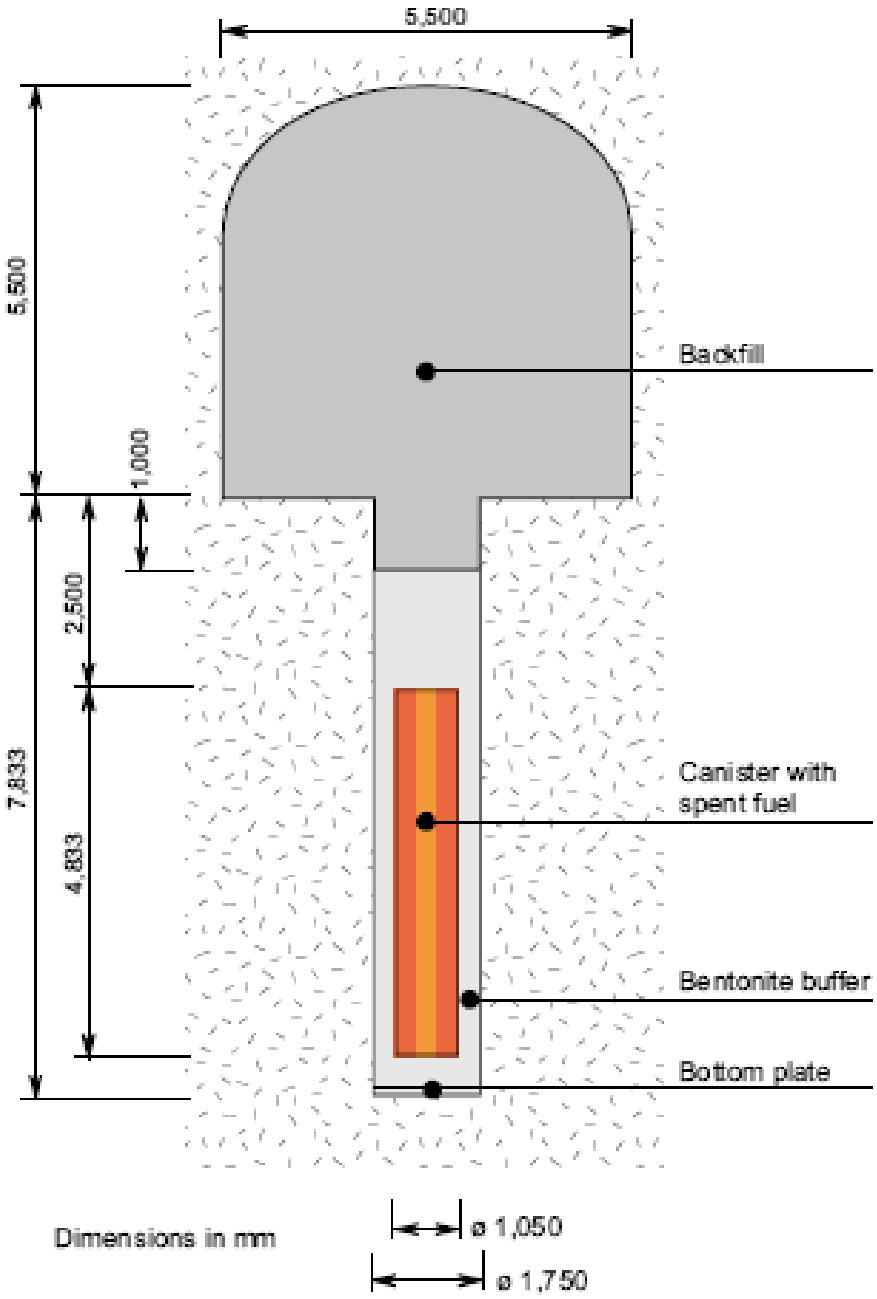

Figure 1-2. KBS-3V concept with backfilled tunnel and canister embedded in bentonited (SKB 2006a).

2 RELEVANT SAFETY-FUNCTION INDICATORS

In SR-Can (SKB 2006a), SKB defines a set of safety functions, which are evaluated using a so-called safety-function indicator, which should meet certain safety-function indicator criteria. Quantitative safety-function indicator criteria are provided for measurable quantities (such as buffer temperature) or (properties such as buffer and backfill density, hydraulic conductivity and swelling pressure). Demonstrating the compliance of these criteria provides arguments that the barriers will function as intended as the repository system evolves. Conversely, should a safety-function indicator criterion be breached, this signals that safety in one way or another is potentially jeopardized, and that the consequences need to be further considered.

The following safety-function indicator criteria are relevant to the evolution of coupled THM processes:

- To assure chemical stability of the buffer, the temperature is required to nowhere exceed 100°C.
- To limit adjective transport the hydraulic conductivity of the buffer should be less than 1×10^{-12} m/s.
- To ensure buffer homogeneity, the buffer swelling stress should exceed 1 MPa
- To prevent canister sinking, the buffer swelling stress should exceed 0.2 MPa.
- To damp the impact of rock shear movement on the canister the density of the buffer should exceed 2,050 kg/m^3.
- To limit colloid transport in the backfill, the backfill density should exceed 1,650 kg/m^3.
- To prevent the backfill from being a preferred pathway for radonuclide transport, the backfill swelling pressure should exceed 0.1 MPa (to assure tightness and homogeneity), and its hydraulic conductivity should be less than 1×10^{-10} m/s.
- To provide favorable hydrologic and transport conditions the fracture transmissivity should be limited.
- To provide mechanically stable conditions, shear movements at the deposition hole should be less than 0.1 m

Although all these safety-function indicator criteria are relevant to coupled THM evolution in general, not all of them are within the scope of the analyses presented in this report.

3 OVERVIEW OF SKB'S ANALYSIS OF THE THM EVOLUTION

In this section, we provide a brief overview of SKB's work related to analysis of the reference evolution of coupled THM processes, as presented in SR-Can (SKB 2006a) and supporting documents. In this overview, we also identify issues and assumptions that we then analyze in Section 4, using our independent modeling tool. The overview includes issues related to near-field behavior, such as buffer resaturation and the evolution of the excavation disturbed zone, as well as far field behavior, such as stress-induced changes in hydrologic properties.

3.1 SKB's modeling tools

SKB's safety case related to coupled THM processes is based on numerical analysis using several codes and models of the proposed KBS-3 repository design. Repository resaturation processes have been analyzed with ABAQUS (Börgesson, 1996), a commercial and widely used finite element code, and CODE-BRIGHT (Olivella et al., 1995), a university-developed finite element code. The issue of spalling and stress induced changes in hydrologic rock-mass properties have been studied using the three-dimensional distinct element code 3DEC (Itasca, 2003). They complement each others in terms of capabilities and applicability. These codes have also been used within the international DECOVALEX project, in which they have been compared to other codes, including those supported and used by SKI's review team. Together, ABAQUS, CODE-BRIGHT, and 3DEC should provide SKB with adequate tools for the analysis of coupled THM processes. However, it is important to scrutinize how these tools are used, including assumptions and conditions for the analysis of coupled THM processes at a proposed KBS-3 repository.

3.2 Thermal evolution and peak temperature

In SR-Can, the peak temperature was estimated using an analytical line source heat transfer solution (SR-Can, SKB 2006a, Section 9.3.2). Using the analytical solution, the peak temperature at a particular site was estimated knowing the heat release from each canister, the canister spacing along tunnels, the axial spacing of deposition tunnels, and the thermal properties of the rock mass and buffer (SR-Can, SKB 2006a, Section 9.3.2). SR-Can specifies an initial thermal output of 1,700 W (SKB 2006a, Section 4.2.3). The resulting heat power function could not be found in the Data Report for SR-Can (Data Report, 2006). However, analytical functions that have been fitted to SKB data on heat release are presented in Börgesson and Hernelind (1999), Börgesson et al. (2006) and Hökmark and Fälth (2003). The function presented in Börgesson and Hernelind (1999) and Börgesson et al. (2006) is the sum of three exponential terms, whereas the function given by Hökmark and Fälth (2003) is the sum of seven exponential terms. We made a comparison of the two functions, shown in Figure 3.1-1. The figure shows that the two functions are very similar. In our independent simulations presented in Section 4 of this report, we use a simpler three-exponential function:

$$P(t) = P_0[0.769 \cdot \exp(-0.02t) + 0.163 \cdot \exp(-0.002t) + 0.067 \cdot \exp(-0.0002t) \qquad (3\text{-}1)$$

where t is time in years after deposition. Note that the equation given in Börgesson and Hernelind (1999) and Börgesson et al. (2006) contains a typo, as they omitted the negative sign of the exponents. Equation (3-1) is the correct function.

SR-Can (SKB 2006a), Sections 4.4.2 and 4.4.3, specifies that the repository layout should be based on 40 m tunnel spacing, whereas the canister spacing should be adapted to the respective site. A canister spacing of 6 and 7.2 m was adopted for the Forsmark and Laxemar sites, respectively. According to SKB's assessment, such canister spacing leads to a peak temperature of about 80°C in the buffer, whereas the maximum allowable temperature is 100°C (see Section 2 of this report).

According to Section 9.3.2 of SR-Can (SKB 2006a), the peak temperature is calculated for a thermal conductivity of the buffer fixed to 1.1 w/mK, and in one case a gap of 3 cm at the buffer/rock interface was assumed. The thermal conductivity of 1.1 w/mK should correspond to the buffer's thermal conductivity at the initial state, i.e., before water resaturation. According to the Data Report (Data Report, 2006) and Hökmark and Fälth (2003), this would represent the thermal conductivity of the buffer at 80% saturation and must be the saturation of the pre-compacted bentonite rings that would be used for installation of the buffer around the canister. The pre-compacted rings would have a dry-density of 1754 kg/m^3 and an initial saturation of 81% (Data Report, 2006, Section 5.3.8).

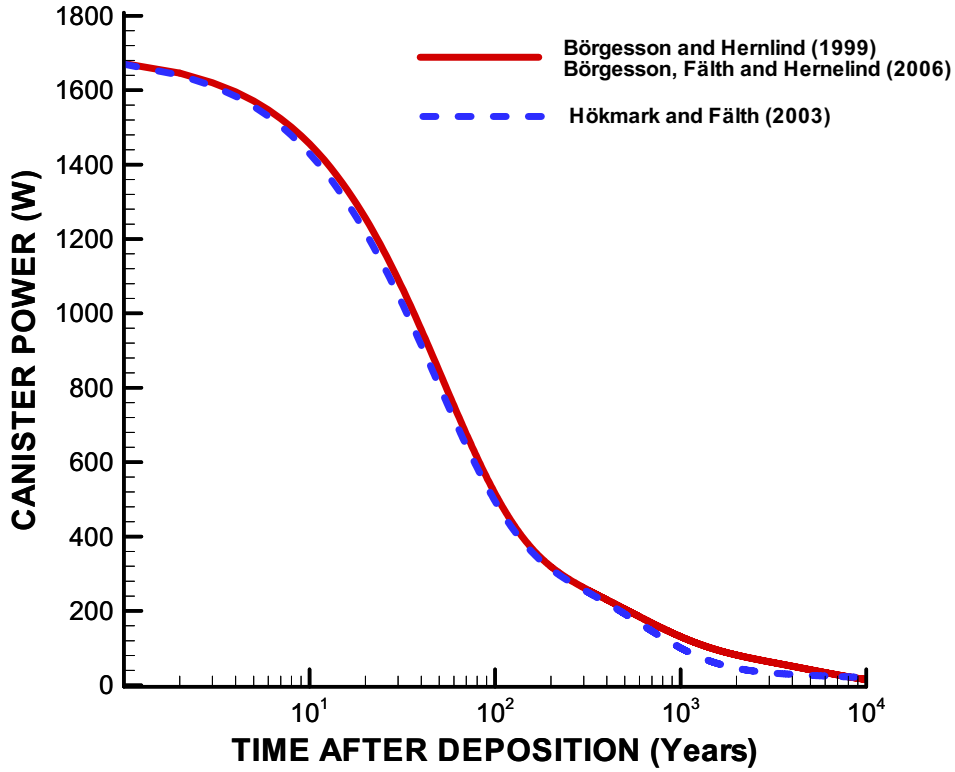

Figure 3.1-1. Plot of two different exponential functions used by SKB to represent heat release from a KBS-3V canister.

After initial swelling of the buffer within the volumetric constraints of the deposition hole, the dry-density would be reduced to ρ_d = 1,570 kg/m^3, with a water ratio of w = 0.17 (according to SR-Can [SKB 2006a], Sections 4.2.8 and 9.3.8). However, in the supporting documents for THM analysis and in the data report, the dry density is given as ρ_d = 1, 670 kg/m^3 with the same initial water content of 0.17. It is not known where this slight inconsistency in targeted dry density comes from, or if it has any relevant impact on the calculations. In all SKB's simulations of the resaturation process, the initial saturation of the buffer was set to between 0.58 and 0.61, corresponding to ρ_d = 1, 670 kg/m^3 (Data Report, 2006, Table 5.3 and 5.7; and Börgesson et al., 2006). At 60% saturation, the thermal conductivity of the buffer would be 0.95 w/mK, which is less than the assumed value of 1.1 w/mK for calculating the peak temperature. Moreover, thermally induced drying of the inner part of the buffer would take place, which could affect the peak temperature, especially in dry rock conditions when the buffer resaturation may be delayed. Thus, there might still be some questions about whether the assumed conditions for calculating the peak temperature cover the most extreme cases of a dry buffer in very low permeable rock.

In Section 4 of this report, we study the evolution of the peak temperature in different conditions, including conditions of tight rock, when the buffer resaturation may be delayed. We also investigate the conditions under which one of the main properties dictating the degree of drying, the thermal vapor diffusivity D_{TV}, is higher than assumed in SKB's current analysis, and thereby causes a stronger buffer drying than expected.

3.3 Hydrological evolution and resaturation time

The time to full resaturation of the buffer is dependent on a number of parameters, most importantly the hydraulic properties of the rock and the bentonite. Ideally, the resaturation time could be accurately estimated with careful characterization of buffer and rock hydraulic properties, and by using an adequate fully coupled THM model. However, our experience from the international code comparison project DECOVALEX shows that model predictions of resaturation time may vary orders of magnitude for different models and model conceptualizations of the same problem setup. The reason for such large variation in calculated resaturation time may be related to the complexity of coupled THM processes and the difficulty in accurately characterizing material properties from available laboratory experiments. Different research teams used slightly different modeling approaches, and characterized and implemented the relatively complex bentonite properties in different ways. These differences show that for the safety assessment of a nuclear waste repository, it will be important not to rely on just one model one approach; indicating several independent models and approaches may be necessary. Moreover, characterization of bentonite properties always involves model calibration at a small scale over a short time period, whereas the repository scale is much larger and the time period is much longer.

Regarding the resaturation processes, SR-Can essentially relies on the recent report by Börgesson et al. (2006), which in turn cites Börgesson and Hernelind (1999). In addition there are a number of reports on coupled THM properties of buffer and backfill. For analysis of the resaturation process, SKB has in large part been using

different generic (rather than site specific) model domains for studying different aspects of the engineered barrier functions. For example, simplified axisymmetric as well as three-dimensional models have been used to calculate resaturation time under various conditions (Börgesson and Hernelind 1999; Börgesson et al., 2006). In SR-Can, the results from these generic simulations were then applied to the hydrological conditions at the Forsmark and Laxemar sites to estimate resaturation times. However, it is important to scrutinize the assumptions and conditions used in the underlying generic simulations. Specifically, the simplified geometries and boundary conditions appear to be unrealistic compared to the real KBS-3V repository, but may be appropriate for parameter studies and analysis of specific issues. One important question is whether these simplified models are useful for quantitative estimates of the buffer resaturation time.

In SR-Can (SKB 2006a), Section 9.3.8, it is stated that if permeability of the rock is very high, $k \geq 1\times10^{-19}$ m^2 (corresponding to a hydraulic conductivity, $K \geq 1\times10^{-12}$ m/s), the resaturation will be controlled by the properties of the buffer and will take 5 to 10 years, with the exact figure depending on where the water-feeding boundary is located. For a low permeability of $k = 1\times10^{-20}$ m^2 ($K = 1\times10^{-13}$ m/s), the resaturation would take about 50 years. If the rock were completely impervious, the buffer would be saturated from the overlying backfill and would take 500 – 2,000 years to resaturate. According to SR-Can (SKB 2006a), the resaturation of the backfill plays an important role in making sure that the buffer gets resaturated even in dry conditions. The resaturation time of the backfill depends on the type of backfill, with water-bearing fractures also expected to play a major role. Based on the above generic modeling applied to the hydrological conditions at respective sites, SR-Can (SKB 2006a) states that the resaturation time is expected to range between 10 to 100 years for Forsmark, whereas the resaturation could be faster at Laxemar.

The water-retention properties (capillary suction and relative permeability) of the rock are parameters that need to be further studied, and their impact on the resaturation process needs to be evaluated. According to SR-Can (SKB 2006a), the resaturation of the buffer would be controlled by the hydraulic properties of the buffer if the rock permeability is larger than 1×10^{-19} m^2. This would indicate that the rock permeability should be about a factor of 15 higher then the permeability of the buffer. However, other studies not related to SR-Can (e.g., Olivella and Gens, 2000), concluded that a factor of 300 would be required. Similar results were obtained by Chijimatsu et al. (2000). Moreover, Olivella and Gens (2000) also showed that the retention curve of the rock is a very important parameter for the bentonite resaturation process. If the suction in the bentonite and backfill is much higher than that in the rock, the rock could be desaturated, which in turn could delay the buffer resaturation. In SR-Can supporting documents (e.g., Börgesson and Hernelind 1999; Börgesson et al., 2006), the rocks retention and relative permeability is represented by a single water-retention curve and a single relative-permeability function. No source is given for the adopted retention and relative-permeability functions. Moreover, uncertainties associated with or their importance for the resaturation process are not discussed at all in SR-Can. Clearly, this is an issue that needs to be studied in more detail, especially with regard to the low-permeability rock at the Forsmask site.

In Figure 3.2-1 we compare the different retention curves used by the SKB for the rock, bentonite buffer and backfill. It can be shown that the potential for desaturation of the rock is high around the MX-80 buffer and around tunnels backfilled with Friedland clay, whereas significant desaturation is unlikely around tunnels backfilled with 30/70 backfill material. The 30/70 backfill consists of a mixture of bentonite and crushed rock with a weight ratio of 30/70, resulting in lower water retention. For example, at an initial saturation of about 60%, the MX-80 bentonite has a suction of about 3×10^4 kPa. Near the bentonite/rock interface pressure will tend to equilibrate or be continuous over the interface. This implies that a pressure of -3×10^4 kPa could develop in the rock adjacent to the bentonite/rock interface, which according to the rock's retentions curve in Figure 3.2-1 would lead to a complete desaturation of the rock (a rock saturation close to zero). Thus, a strong desaturation of the rock surrounding the bentonite buffer is quite likely if the permeability of the rock is low. For a 30/70 backfill, on the other hand, the initial suction is much smaller and cannot induce significant desaturation with the assumed rock retention curve. At an initial saturation of 58%, the 30/70 backfill has a suction of about 1×10^3 kPa, which may induce only a slight desaturation of the rock. However, these speculations about the potential for rock desaturation are only valid if the rock water-retention curve is the one assumed by SKB.

We believe that the retention curve of the rock is a very uncertain parameter, one that would require further studies and sensitivity analysis. In Figure 3.2-2, we compare the retention and relative permeability curve used by SKB (Börgesson and Hernelind, 1999) with two other retention curves reported in the literature to represent crystalline rock. The retention curve assumed by SKB is similar to that of Finsterle and Pruess (1995), which was determined by inverse modeling of a tunnel-ventilation test performed at the Grimsel Test Site in Switzerland. However, rock fractures, as well at the interface between the rock and bentonite, would most likely have different retention properties. For example, Figure 3.2-3 shows retention and permeability curves developed for volcanic tuff at Yucca Mountain, Nevada, which are very different for rock matrix and fracture. Whether desaturation of the rock will take place after emplacement will depend on the complex interaction and retention properties of the different material involved (bentonite, backfill, rock matrix, rock fractures, bentonite/rock interface, spalled zone, etc.). Moreover, additional substantial desaturation could take place during the operation when tunnels are open and subjected to ventilation. In SR-Can or supporting documents there, seems to be no consideration or discussion of these effects. What is the expected relative humidity in the tunnel and how will this affect drying and subsequent resaturation process?

Another issue to consider is uncertainties in thermal-hydrological properties of the buffer. In particular, the thermal vapor diffusivity, D_{TV}, is a very important parameter for the degree of drying that can occur in the buffer before resaturation. The thermally induced drying may also contribute to delay the resaturation of the buffer. From the SR-Can and the supporting documents on the buffer properties, it appears that D_{Tv} has been determined from one small-scale laboratory experiment reported in Börgesson and Hernelind (1999). The model was calibrated against this experiment, but the initial saturation and suction are different in the model and in the experiment. We believe this might be a rather crude and uncertain estimate of the D_{TV}. The adopted D_{TV} needs to be validated against field experiments and/or mock-up experiments, but

in the mean time, this parameter should be varied to investigate the potential unexpected impact on the resaturation time and peak temperature.

In Section 4, we will investigate the key parameters affecting the resaturation time for both Forsmark and Laxemar sites. This includes investigating the role of hydraulic boundary conditions, water-retention curves, and buffer parameters such as D_{TV}.

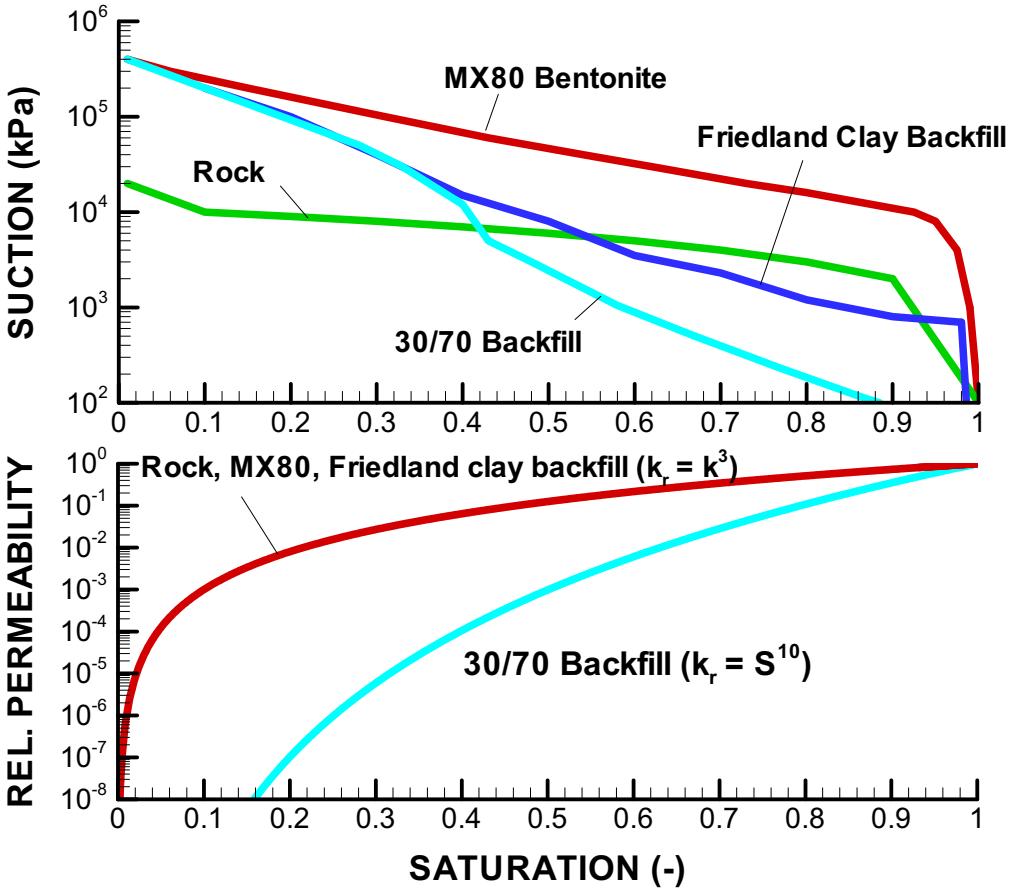

Figure 3.2-1. Water-retention and relative permeability curves used by SKB to represent various components (buffer, backfill and rock) at a KBS-3V repository.

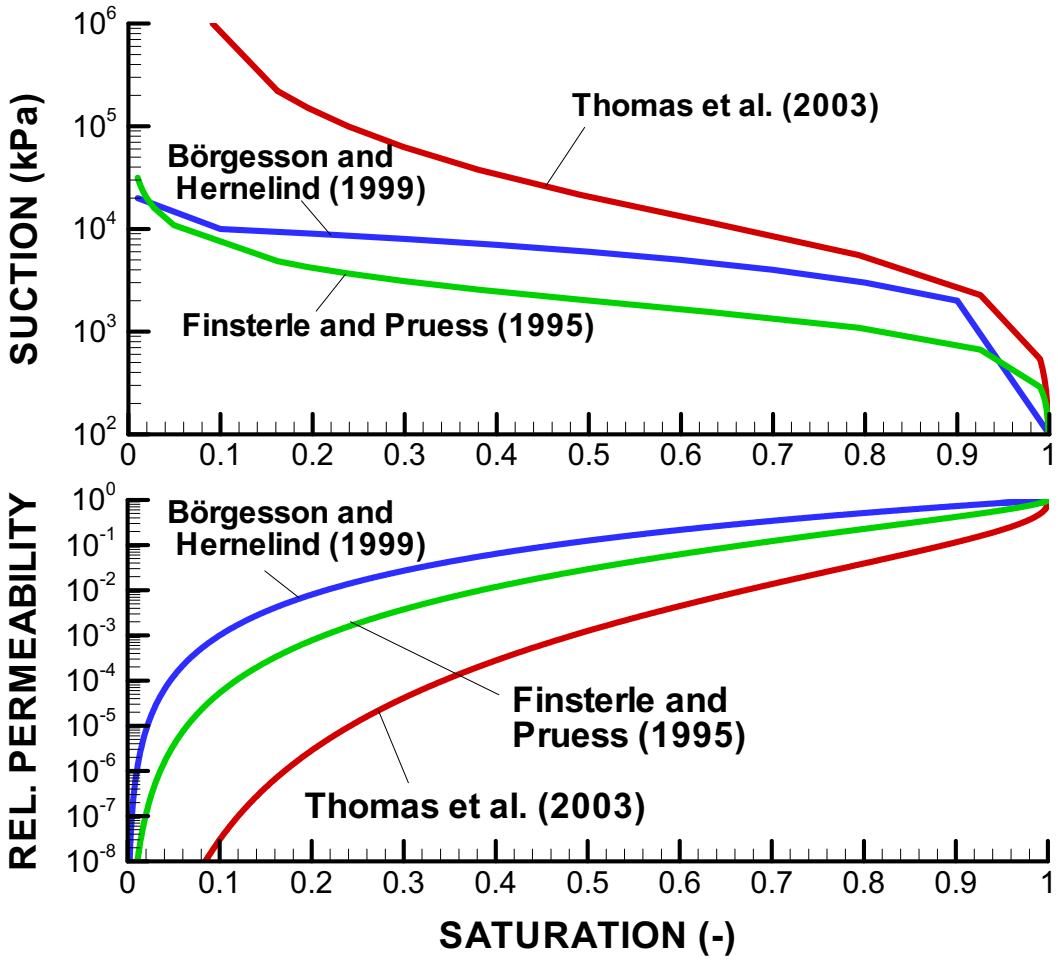

Figure 3.2-2. Alternative water-retention and relative-permeability curves reported in the literature for crystalline rock.

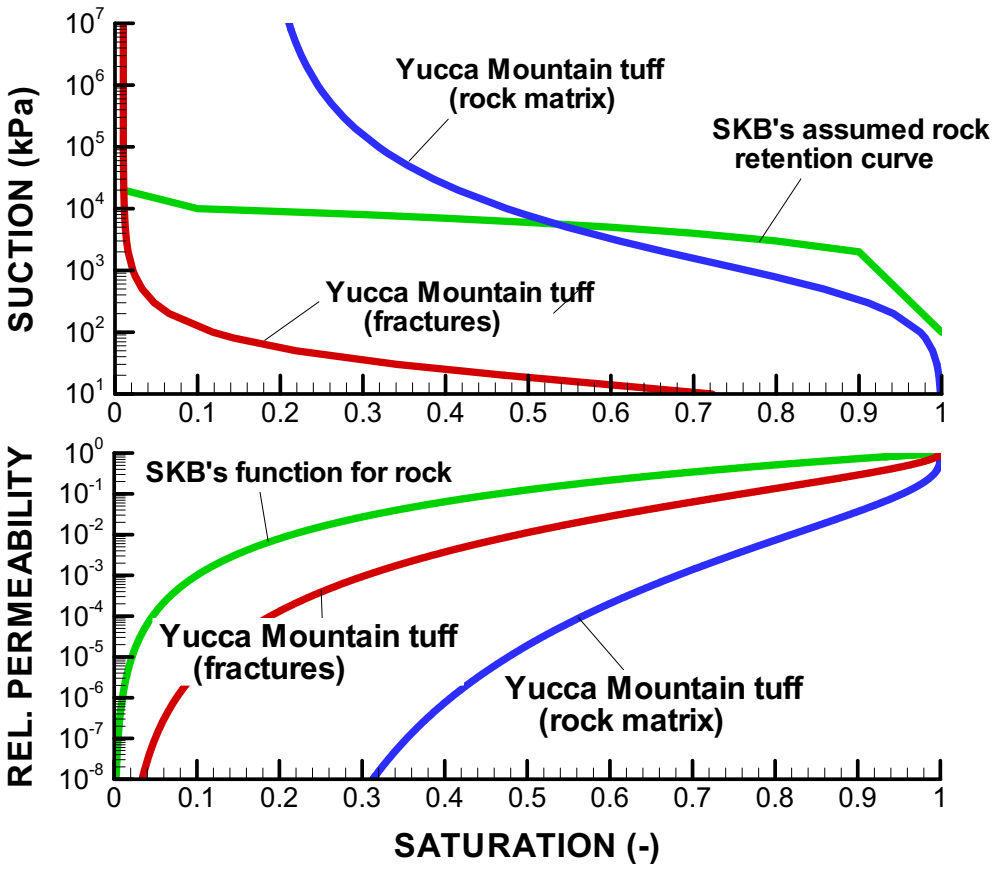

Figure 3.2-3. Water-retention and relative-permeability curves developed for volcanic tuff at the Yucca Mountain site in Nevada, showing the order-of-magnitude difference in the retention properties of matrix rock and fractures. The retention and relative permeability curves used for rock in SKB's analysis is shown in green for comparison.

3.4 Mechanical evolution, EDZ, and rock spalling around openings

The EDZ and the potential for rock spalling have been studied extensively by the SKB, since these are near-field phenomena that might have a significant impact on the release and transport of radioactive nuclides. The EDZ around tunnels have been studied at a number of field experiments at the Äspö Hard Rock Laboratory since the early 1990s. In SR-Can (SKB 2006a), Section 9.2.2, the EDZ is defined as the part of the rock mass closest to the underground opening that has suffered irreversible deformation where shearing of existing fractures (as well as propagation or development of new fractures) has occurred (Bäckblom et al. 2004). SR-Can (SKB 2006a), Section 9.2.2 states that experience from EDZ studies at ZEDEX and TASQ tunnels at Äspö shows that the EDZ along tunnels can be managed and controlled by careful drill and blast design and quality assurance control during excavation. Specifically, the drill and blast technique leads to an EDZ that is discontinuous along the tunnel, and therefore the effects on the continuous permeability along the tunnel would be small. For the SR-Can, two cases of EDZ was studied, the first one a limited and discontinuous zone (i.e. intact rock zones between damaged zones along the

tunnel), and the second one a zone with a two-orders-of-magnitude increase in permeability along a continuous skin-zone around the tunnel. Note that these EDZ estimates are those caused by the excavation process and present already during the operational phase. It is then important to investigate how the EDZ may change as a result of thermal stressing that will occur after closure of the repository.

Rock spalling is caused by high compressive uniaxial stress, for example near an unsupported tunnel wall or deposition hole, and results in formation of tensile cracks parallel to the wall surfaces. The formation of fractures parallel to a wall surface of a tunnel or deposition hole may lead to a significantly increased permeability within the spalled zone, especially along the axial direction of the tunnel or deposition hole. Moreover, the spalled rock may loosen and affect the hydraulic properties at the interface between the buffer/rock or backfill/rock. Such increased permeability in the spalled zone may affect radionuclide transport.

SKB estimates the likelihood and extent of spalling in deposition holes using the 3DEC near-field THM analyses (Hökmark et al., 2006), and the use of observations from a pillar stability experiment at Äspö. These are complemented by analytical analyses described in Martin (2005). The present view, as observed from the pillar stability experiment at Äspö, is that spalling can occur when the maximum principal stress exceeds 55% of the intact rock strength (SR-Can, SKB2006a, Section 9.2).

For the layout of the repository, the earlier analytical analysis by Martin et al. (2005) was utilized to assess the potential for spalling during excavation and the operational phase (without heat load). The analysis by Martin et al. (2005) indicated that high stress at Forsmark would lead to a high potential for rock spalling during the operational phase. Therefore, to minimize the risk of spalling at Forsmark, the preliminary layout limits the depths of the repository to 400 m and the tunnels are oriented parallel to the maximum principal stress (SR-Can, SKB 2006a, Section 4.4.2). In the design of the Laxemar repository, on the other hand, SKB assessed—based on Martin (2005)—that there would be a negligible risk of spalling if the repository depth was limited to 500 m (SR-Can, SKB 2006a, Section 4.4-3). This assessment is an obvious contradiction with that of Hökmark et al. (2006) who made the reverse assessment: no spalling at Forsmark during operational phase, but there will probably be in Laxemar (Hökmark et al., 2006, Section 6.5.2). Because in one of their analyses SKB assessed negligible risk of spalling during the operation phase at Laxemar, the tunnels at Laxemar 500 m depth option would be oriented to make best use of available space without consideration of stress orientation. This might be a mistake, especially since the thermal mechanical analysis by Hökmark et al. (2006) indicates that the risk of spalling increases during the thermal phase as thermal stress leads to increased tangential compressive stresses around the deposition holes. Specifically, the analysis by Hökmark et al. (2006) shows that during the thermal phase there will be some spalling induced both at Forsmark and Laxemar sites unless there is some supporting bentonite swelling pressure (SR-Can, SBK 2006a, Section 9.3.5). It is expected that the extent of failure will be confined within a notch shape zone, extending about 0.1 m deep and 0.14 m wide.

In SR-Can, it is concluded that the spalling around the deposition holes could have considerable impact on the flow rate and radionuclide mass transfer around the

deposition holes (SR-Can, SKB 2006a, Section 9.3.13). Water will be drawn into the damaged zone from fractures intersecting the deposition hole, leading to an increased mass transfer between the buffer and the rock. For the pessimistic case of a very high hydraulic conductivity in the spalled zone, SKB estimates that the thermal spalling would increase the dose that could be released from the geosphere by almost an order of magnitude (SR-Can, SKB 2006a, Section 10.5.7).

In Section 4, we will study the potential for rock spalling and rock failure both around the deposition holes and overlying tunnels. The approach is similar to that of SKB, i.e., calculating the evolution of the stress field and then applying various failure or spalling criteria to evaluating the likelihood of failure. The results can be directly compared with those of SKB's analysis.

3.5 THM-induced fracture reactivation and permeability change

The induced fracture reactivation and associated permeability changes have been estimated using a set of numerical models with 3DEC (Hökmark et al., 2006). The potential for fracture reactivation and associated permeability changes were evaluated for both near field and far field. The near-field analysis was conducted for both Forsmark and Laxemar sites using a near-field 3DEC model of a KBS-3V repository. The model included a few fractures of various orientations. The 3DEC analysis was used to calculate the mechanical responses (e.g., stress changes across fractures and associated fracture deformations). Based on mechanical responses calculated with 3DEC, permeability changes were estimated using various relationships between fracture transmissivity and normal stress or transmissivity and fracture shear displacement. We believe this is an adequate approach for estimating THM-induced permeability changes. However, the amount of permeability change obtained will depend strongly on the applied relationships between fracture transmissivity and normal stress or shear displacement.

The results of the analysis by Hökmark et al. (2006) show that, during excavation of the tunnels, permeability may increase by one or two orders of magnitude, but only close to tunnels (within about 1.5 m from the tunnel walls). Hökmark et al. (2006) attributed the permeability changes to relief stress normal across existing fractures rather than shear dilation. During heating, the permeability generally tends to decrease as results of thermal compressive stress that would tend to compress fractures to smaller aperture. After the thermal period, these permeability changes were essentially reversed, although locally small irreversible changes were observed. At the Forsmark site, some fracture shear displacements up to 4 and 5 mm were calculated. Hökmark et al. (2006) estimated that permeability in these fractures could increase by (at the most) one or two orders or magnitude. However, Hökmark et al. (2006) did not find widespread shearing and concluded that shearing might result in mostly local changes.

Reactivation of fractures in the far field was also evaluated in Hökmark et al. (2006). A far field thermal-elastic 3DEC model was used without explicit representation of fractures. Hökmark et al. (2006) calculated increased horizontal compressive stresses near the repository, whereas there is a relief of horizontal stresses near the ground surface. Based on changes in compressive stresses, and the applied stress-versus-

permeability relationships, Hökmark et al. (2006) found an unchanged or modest permeability decrease at depths below 300 m. Most permeability increases could occur near the ground surface, where the stresses would be relieved. However, the effects on permeability of those near-surface changes were not estimated by Hökmark et al (2006).

For estimating changes in fracture transmissivity caused by changes in fracture normal stress, Hökmark et al. (2006) utilize two empirical stress-vs-aperture functions and the cubic law. The first is based on the fracture normal closure model of the so-called continuous yielding model, which is a standard model in the 3DEC code. The second is an exponential function proposed by Rutqvist et al. (2002). Both models can be fitted to experimental data showing typical nonlinear stress-versus-aperture relationships. For this analysis, data from laboratory experiments on Stripa Granite and Sellafield volcanic tuff were used. An alternative stress-versus-transmissivity function, which had been fitted to experimental data at Stripa Granite by Dershowitz et al. (1991), was also explored. In Hökmark et al. (2006), the empirical function derived from data of the Sellafield volcanic tuff (Liu et al., 2004) was used as a reference model, because the alternative models derived from data on granite "would likely over predict the normal closure at high stress." This does not appear to be reasonable justification for dismissing data from granite samples and adopting data from volcanic tuff samples. It appears the other two alternative models did not include a residual hydraulic aperture, which is an important parameter at high normal stress. Moreover, the estimated changes are then based on experimental data from one rock sample and the residual aperture was fixed to 10 μm, which would correspond to a fracture transmissivity of 8×10^{-10} m^2/s.

One potentially very important aspect missing from the far-field analysis is the potential for shear-induced fracture permeability in a rock mass that is critically stressed for shear. Many studies have shown that fractures favorably oriented for shear-slip, so-called critically stressed fractures, tend to be active groundwater flow paths (Barton et al., 1995, Ferill et al., 1999, Rutqvist and Stephansson, 2003). The rational for bulk permeability being dominated by critically stressed fractures is that most fractures in the bedrock are cemented because of water/rock chemical reactions. If shear slip occurs on a critically stressed fracture, it can raise the permeability through several mechanisms, including brecciation, surface roughness, and breakdown of seals (Barton et al., 1995). In fact, a correlation between shear stress and hydraulic conducting fractures has also been reported for the rock mass at Äspö Hard Rock Laboratory (Talbot and Sirat, 2001). Moreover, the stress field models developed by SKB for the Laxemar site (stress dominant I and II) are strongly anisotropic, in fact it is questionable whether the rock mass could sustain such an anisotropic stress field without frictional reactivation. Figure 3.4-1 illustrates how the current permeability field may have been developed over past geological history, based on mechanical and chemical processes that perhaps compete with each other. The present-day permeability field may be an equilibrium reached between the competing mechanical forces that would tend to promote shearing and the chemical processes that might tend to seal fractures. Regional tectonic forces might primarily cause the mechanical deformations and the resulting long-term strain rate. However, during the thermal pulse from the repository, this equilibrium will be broken because the horizontal stress will increase substantially, causing much higher strain-rate than

the long-term tectonic strain-rate—resulting in a rapid increase in shear stresses. Figure 3.4-2 shows the results from a discrete element analysis, indicating how large shear stress can create hydraulic active channels in the fracture network, channels that could substantially increase rock-mass permeability (Min et al., 2004). At the Laxemar and Forsmark sites, the substantial increase in horizontal stress could produce more widespread shearing of fractures in the fractured rock mass, which could open fractures and enhance existing fracture permeability. This possibility needs to be further investigated, because it could lead to an increase in the permeability field that could be irreversible.

In Section 4, we will analyze and discuss potential THM-induced changes in the far field. However, we will consider alternative stress-versus-transmissivity functions derived from *in situ* experiments, including borehole injection tests at the Laxemar site. Moreover, we will investigate the likelihood for more widespread shearing in the far field.

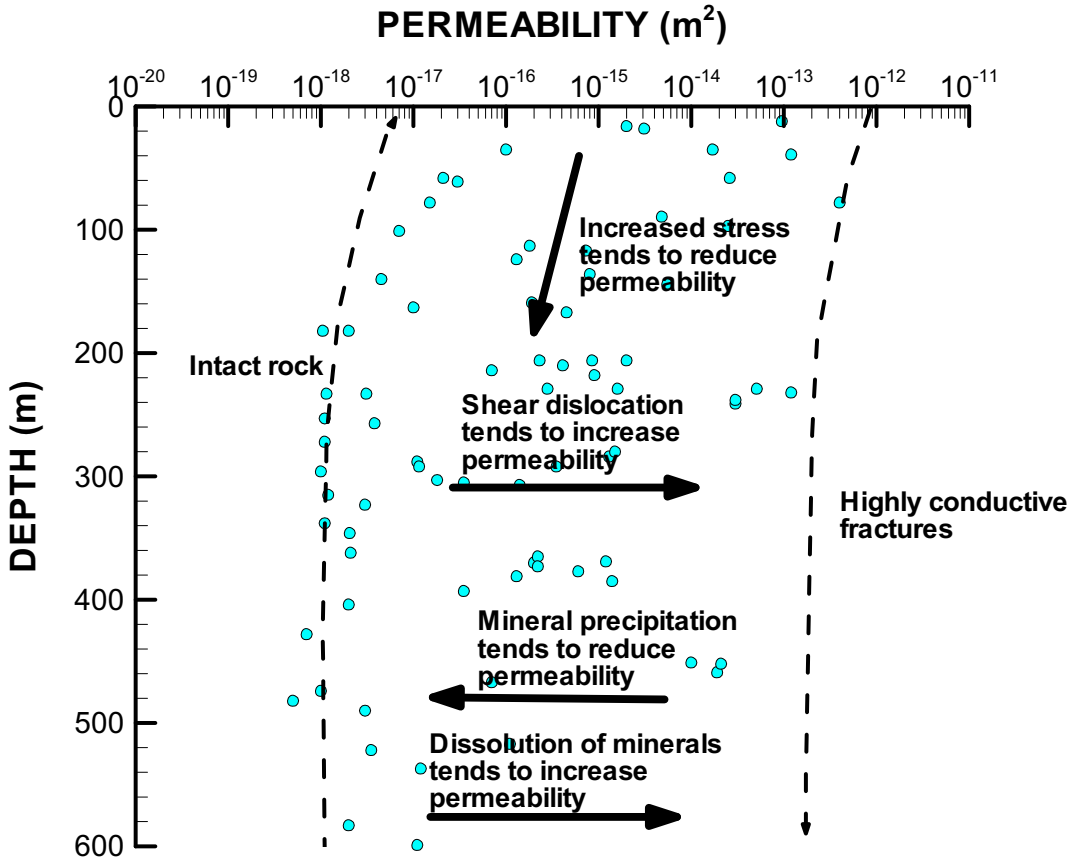

Figure 3.4-1. Permeability measured in short interval well tests in fractured crystalline rocks at Gideå, Sweden (data points from Wladis et al. 1997). Effects of shear dislocation and mineral precipitation/dissolution processes obscure the dependency of permeability on depth (Rutqvist and Stephansson, 2003).

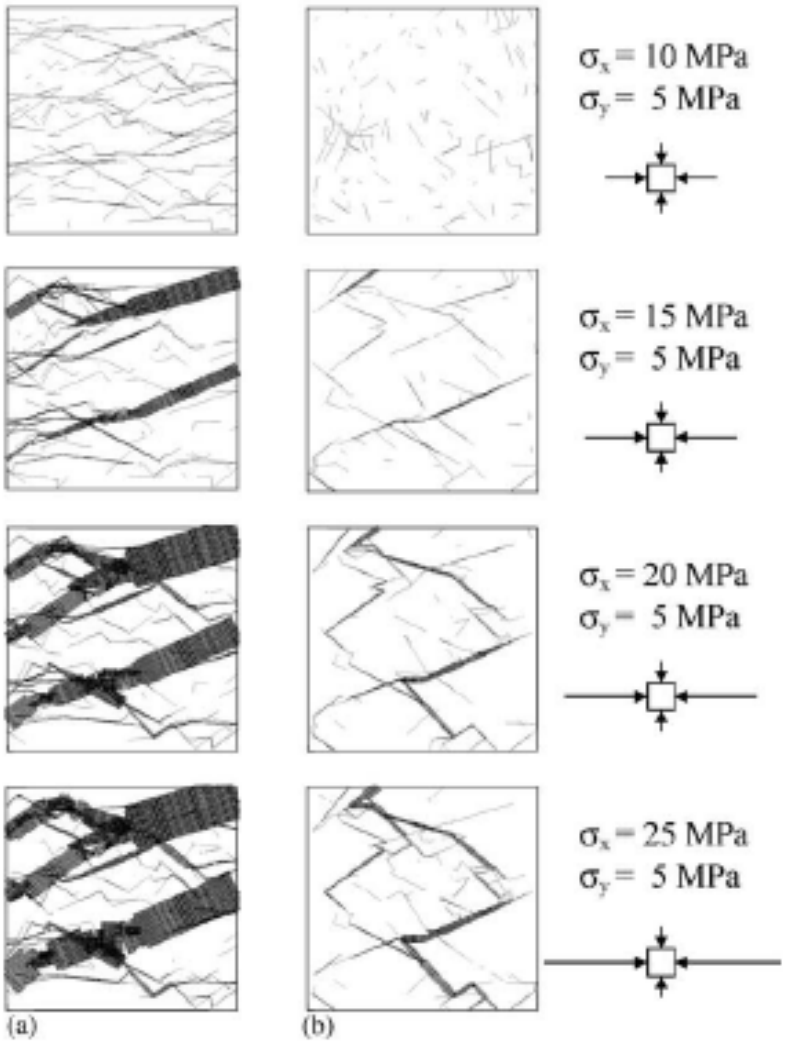

Figure 3.4-2. Results from a discrete fracture analysis showing development of fluid pathways during stress application with the direction of hydraulic gradient (a) from left to right and (b) from top to bottom. The thickness of the line represents the magnitude of flow rates (from Min et al., 2004).

4 ANALYSIS OF NEAR-FIELD THM BEHAVIOR

This section presents our independent coupled THM analysis of KBS-3V repositories at both Forsmark and Laxemar. This analysis is developed based on years of model development and experience in coupled THM analysis within the international DECOVALEX project. The analysis is conducted with the ROCMAS code (Rutqvist et al., 2001), which is a finite element code completely independent of SKB's codes, and hence can be used to independently check SKB's simulation results. The fundamental approach and field equations for the ROCMAS code is summarized in Appendix A. In this section, we address near-field THM behavior,

4.1 Finite element discretization and material properties

Because of the periodic nature of the KBS-3V repository concept design, the simulations were conducted with a one-quarter symmetric three-dimensional model containing one deposition hole (Figure 4.1-1). The quarter symmetric geometry represents a condition that neighboring deposition holes are simultaneously excavated and heated. The models extend vertically from the ground surface to a depth of 1,000 m below the emplacement tunnels. The model dimensions are site specific according to the respective suggested layouts for the Forsmark and Laxemar repository alternatives. For the Forsmark site, the repository tunnel is located at 400 m depth, with canister spacing of 6 m. For the Laxemar site, the repository tunnel is located at 500 m depth, with canister spacing of 7.2 m.

The material properties of buffer, rock mass, waste container, and groundwater are presented in Tables 4.1 through 4.5. The sources of every material parameter value are also given in Table 4.1 through 4.5.

The material properties for the bentonite buffer were extracted from Börgesson and Hernelind (1999), and Börgesson et al. (2006), and represent MX-80 bentonite (Table 4.1). Further calibration and validation of the properties of MX-80 bentonite are presented in Appendix B. One important parameter is the thermal diffusion coefficient, D_{TV}, which has to be calibrated against so-called thermal gradient tests. One such thermal gradient test have been used by Börgesson and Hernelind (1999) to derived a saturation dependent D_{TV} for MX-80. It is difficult to evaluate the match between model and measurements in Börgesson and Hernelind (1999), since model simulations begin at different initial saturation than the experiment. The thermal gradient test was unfortunately conducted at a void ratio of 1.0, which is much different from *in situ* conditions of the emplaced buffer, which is expected to have a void ratio of 0.77. In our analysis of the thermal gradient test presented in Appendix B, we found it quite difficult to satisfactorily match the experimental results over the entire range of the experimental data. Therefore, and because of the general uncertainties in determining this important parameter, we performed the simulations using alternative and bounding estimates of the D_{TV} function. This is different from SR-Can, which relies on one single D_{TV} function.

The material properties of the backfill in the basic ideal case, corresponds to the 30/70 backfill material, consisting of a mixture of bentonite and crushed rock with a weight ratio of 30/70. Most properties for this type of backfill have been extracted from Börgesson et al. (2006), with some properties assumed similar to or adjusted from the

MX-80 bentonite properties (Table 4.2). The impact using the alternative Friedland Clay backfill properties is also investigated in this report.

Table 4.1. Material properties of bentonite buffer (MX-80 bentonite)

Parameter	Value	Source
Saturated permeability, k_{wS} [m^2]	6.5×10^{-21}	Börgesson and Hernelind (1999) and also in Börgesson et al. (2006).
Capillary pressure, P_c [Pa]	Defined by Equation B.1 and shown in Figure 3.2-1	Fitted to experimental data from Börgesson and Hernelind (1999) and also in Börgesson et al. (2006) as described in Appendix B.
Relative permeability, k_r [-]	$k_r = S^3$	Börgesson and Hernelind (1999) and also in Börgesson et al. (2006).
Porosity, ϕ [-]	0.435	Börgesson and Hernelind (1999) and also in Börgesson et al. (2006).
Bulk Modulus, K [MPa]	17	Back-calculated to fit swelling stress in Börgesson and Hernelind (1999) as described in Appendix B.
Poisson ratio, ν [-]	0.3	Assumed
Biot's effective stress parameter, α [-]	0.0 ($P_l < 0.0$) 1.0 ($P_l \geq 0.0$)	Assumed, since swelling is dictated by the back-calculated value of moisture swelling coefficient as described in Appendix B.
Moisture swelling coefficient, β_{sw} [-]	0.4	Fitted to drying test data from Börgesson and Hernelind (1999) as described in Appendix B.
Thermal expansion, β_T [1/°C]	1.0×10^{-5}	Assumed
Dry specific heat, C_{vs} [J/kg·°C]	800	Börgesson and Hernelind (1999) and in Börgesson et al. (2006)
Thermal conductivity, [W/m·°C]	Equation (B.12)	Fitted to experimental data in Börgesson and Hernelind (1999) and in Börgesson et al. (2006)
Thermal diffusion coefficient D_{Tv} [-]	Equation (B.8)	Börgesson and Hernelind (1999) with two different alternative values as a result of model calibration in Appendix B

Table 4.2. Material properties of 30/70 backfill

Parameter	Value	Source
Saturated permeability, k_{wS} [m^2]	0.5×10^{-17}	Börgesson et al. (2006).
Suction pressure, s [Pa]	Equation B.1 with $P_0 = 0.1087$ MPa $\lambda = 0.19$, $P_s = 800$ MPa, $\lambda_s = 1.1$	Modified van-Genuchten function fitted to data from Börgesson et al. (2006) and also used by Börgesson et al. (2006)
Relative permeability, k_r [-]	$k_r = S^{10}$	Börgesson et al. (2006).
Porosity, ϕ [-]	0.63	Börgesson et al. (2006).
Bulk Modulus, K [MPa]	17	Used same values as in buffer which is similar to elastic properties used for 30/70 backfill by Börgesson et al. (2006) p. 75
Poisson ratio, ν [-]	0.3	Assumed
Biot's effective stress parameter, α [-]	0.0 ($P_l < 0.0$) 1.0 ($P_l \geq 0.0$)	Assumed, since swelling is dictated by the back-calculated value of moisture swelling coefficient as described in Appendix B.
Moisture swelling coefficient, β_{sw} [-]	0.14	The value of this parameter was adjusted (lowered) from the value used for the buffer to achieve a swelling stress of about 3 MPa upon full wetting.
Thermal expansion, β_T [1/°C]	1.0×10^{-5}	Assumed
Dry specific heat, C_{vs} [J/kg·°C]	800	Assumed equivalent to that of MX-80 bentonite.
Thermal conductivity, [W/m·°C]	Equation (B.12)	Assumed equivalent to that of MX-80 bentonite buffer. Value used in Börgesson et al. (2006) is slightly higher.
Thermal diffusion coefficient D_{Tv} [-]	Equation (B.8)	Assumed equivalent to that of MX-80 bentonite.

Most of the rock-mass properties have been extracted from the site descriptive models of Forsmark and Laxermar sites (Table 4.3a and b). In our simulation, we will treat the rock hydraulic properties as parameters that could vary widely, and we will perform simulations with different values. For the ideal base case, in which resaturation is relatively fast, the rock-mass permeability is set to 1.0×10^{-16} m^2. However, in a parameter study, the rock permeability is varied to a value as low as 1.0×10^{-21} m^2 to investigate extreme cases of low-permeability rock. We also investigate the impact of flow from fractured that are included in the model and can be activates as shown in Figure 4.1-2. This is similar to the approach used by Börgesson et al. (2006). In contrast to SR-Can and its supporting documents, we will also investigate what impact the water-retention curve the rock might have on the

resaturation process. As a starting point we will use the rock retention curve determined by Finsterle and Pruess (1995), using inverse modeling of two-phase flow processes at a tunnel ventilation experiment at Grimsel Test Site in Switzerland. According to Figure 3.3-2, these retention properties are similar to that used in Börgesson et al. (2006) and Börgesson and Hernelind (1999).

Table 4.3a. Rock-mass properties for Forsmark

Parameter	Value	Source
Density, ρ_s [kg/m^3]	2701	Forsmark site descriptive model (SKB 2005) for vertical stress gradient of 0.0265z MPa
Porosity, ϕ [-]	0.003	Assumed
Young's Modulus, E [GPa]	68 GPa	Forsmark site descriptive model, SKB (2005), Table 6-7, rock domain RFM012
Poisson's Ratio, ν [-]	0.22	Forsmark site descriptive model, SKB (2005), Table 6-7, rock domain RFM012
Biot's effective stress parameter, α [-]	1.0	Assumed
Specific heat, C_v [J/kg·°C]	803	Calculated from heat capacity 2.17 MJ/m^{3}K given in Forsmark site descriptive model, SKB (2005), Table 7-14, divided by the rock density
Thermal conductivity, K_m [W/m·°C]	3.46	Forsmark site descriptive model , SKB (2005), Table 7-13 rock domain RFM012
Thermal expansion, β [1/°C]	7.7×10^{-6}	Forsmark site descriptive model, SKB (2005), Table 7-10 for granite
Hydraulic permeability, k {m^2]	1.0×10^{-16}	Assumed value for the ideal base case of a relatively high rock permeability
Van-Genuchten's retention parameter, P_0 [MPa]	5.5 MPa	Determined by inverse modeling of two-phase flow processes during a ventilation experiment in crystalline rock at Grimsel by Finsterle and Pruess (1995)
Van-Genuchten's retention parameter, β_{VG}	3.0	Determined by inverse modeling of two-phase flow processes during a ventilation experiment in crystalline rock at Grimsel by Finsterle and Pruess (1995)

Table 4.3b. Rock-mass properties for Laxemar

Parameter	Value	Source
Density, ρ_s [kg/m^3]	2752	Value to obtain vertical stress gradient of 0.027z MPa according to Laxemar site descriptive model Table 6.9 for stress domain I
Porosity, ϕ [-]	0.003	Assumed but within range of measured values reported in Laxemar site descriptive model (SKB 2006b)
Young's Modulus, E [GPa]	55 GPa	Laxemar site descriptive model, SKB (2006b), Table 6-7, for Domain A
Poisson's Ratio, ν [-]	0.24	Laxemar site descriptive model, SKB (2006b), Table 6-7, for Domain A
Biot's effective stress parameter, α [-]	1.0	Assumed
Specific heat, C_v [J/kg·°C]	814	Calculated from heat capacity 2.24 MJ/m^{3}K SR-Can Table 3-2, divided by the rock density
Thermal conductivity, K_m [W/m·°C]	2.77	SR-Can, Table 3-2.
Thermal expansion, β [1/°C]	7.7×10^{-6}	From Hökmark et al. (2006), which is within the range of 6 to 8×10^{-6} 1/°C given in the Laxemar site descriptive model, SKB (2006b), Table 7-9
Hydraulic permeability, k {m^2]	1.0×10^{-16}	Assumed value for the ideal base case of a relatively high rock permeability
Van-Genuchten's retention parameter, P_0 [MPa]	5.5 MPa	Determined by inverse modeling of two-phase flow processes during a ventilation experiment in crystalline rock at Grimsel by Finsterle and Pruess (1995)
Van-Genuchten's retention parameter, β_{VG}	3.0	Determined by inverse modeling of two-phase flow processes during a ventilation experiment in crystalline rock at Grimsel by Finsterle and Pruess (1995)

Table 4.4. Properties of the emplacement container

Parameter	Value	Source
Density, ρ_s [kg/m^3]	7000	Börgesson et al. (2006).
Hydraulic permeability, k_w [m^2]	1.0×10^{-27}	Assumed low value
Porosity, ϕ [-]	1.0×10^{-5}	Assumed low value
Young's modulus, E [GPa]	210	Börgesson et al. (2006).
Poisson's ratio, ν [-]	0.3	Börgesson et al. (2006).
Specific heat, C_v [J/kg°C]	4600	Assumed
Thermal conductivity, K_m [W/m°C]	200	Börgesson et al. (2006).
Thermal expansion coefficient, β [1/°C]	1.2×10^{-6}	Assumed

Table 4.5. Properties of the groundwater

Parameter	Value	Source
Thermal expansion coefficient, β_T [1/°C]	4.0×10^{-4}	Standard thermo-physical table (Vargaftik, 1975)
Specific heat, C_{vw} [J/kg·°C]	4180	Standard thermo-physical table (Vargaftik, 1975)
Viscosity, η_w [Ns/m^2] (at 25 °C)	1.070×10^{3}	Standard thermo-physical table (Vargaftik, 1975)
Compressibility, β_p [1/Pa]	4.4×10^{-10}	Standard thermo-physical table (Vargaftik, 1975)
Density, ρ_{w0} [kg/m^3] (at 25 °C)	997.0	Standard thermo-physical table (Vargaftik, 1975)
Vapor specific heat of water vapor, C_{vS} [J/kg·°C]	1900	Standard thermo-physical table (Vargaftik, 1975)
Latent heat of vaporization, L_0 [J/kg]	2.4×10^{6}	Standard thermo-physical table (Vargaftik, 1975)
Specific gas constant of water vapor, R [J/kg°C]	461.5	Standard thermo-physical table (Vargaftik, 1975)

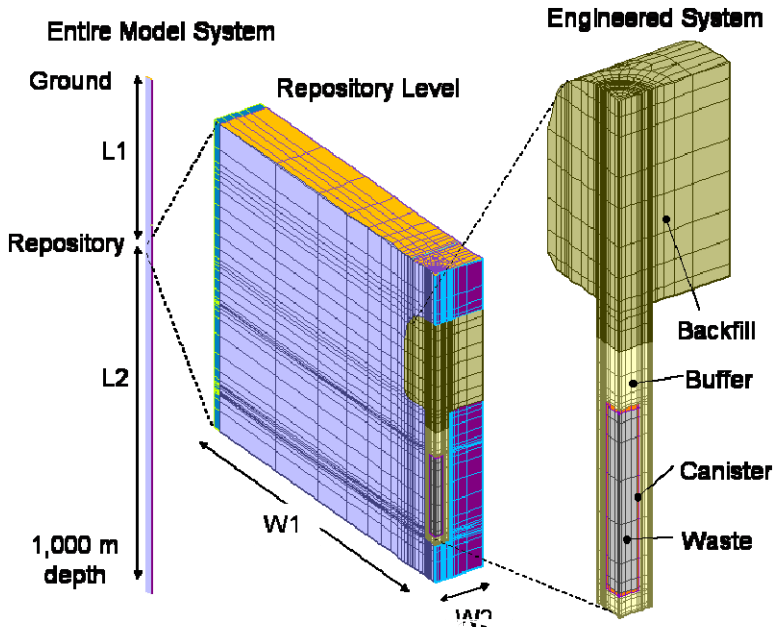

	Depth of repository, L1 (m)	Distance to bottom, L2 (m)	Half tunnel spacing, W1 (m)	Half canister spacing, W2 (m)
Laxemar	500 m	1,000 m	40/2 = 20	7.2/2 = 3.6
Forsmark	400 m	1,000 m	40/2 = 20	6/3 = 3

Figure 4.1-1a. Quarter symmetric finite element model for coupled THM simulations of KBS-3V repositories at Forsmark and Laxemar.

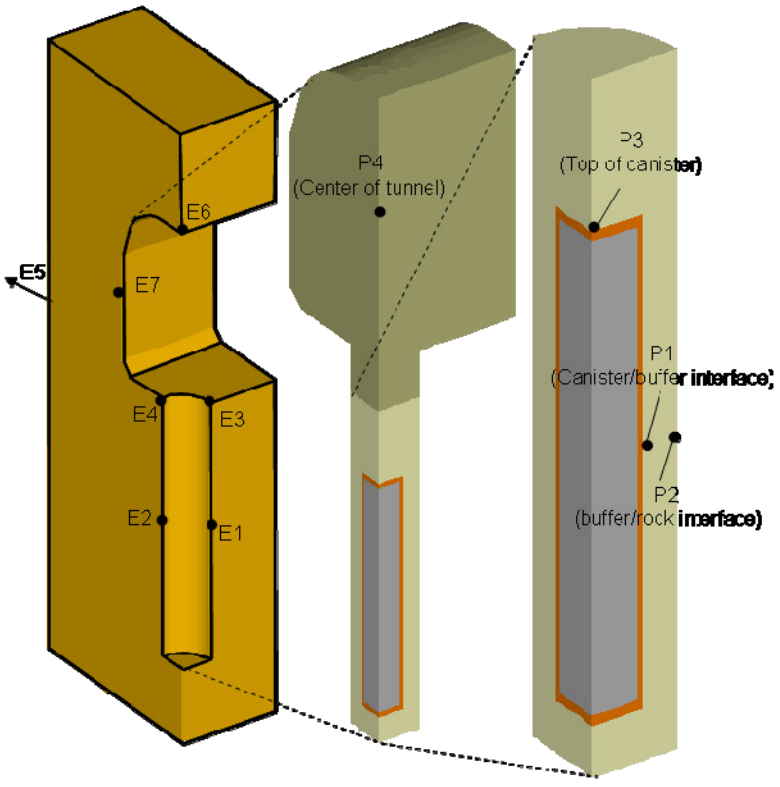

Figure 4.1-1b. Monitoring points for presentation of time-dependent results.

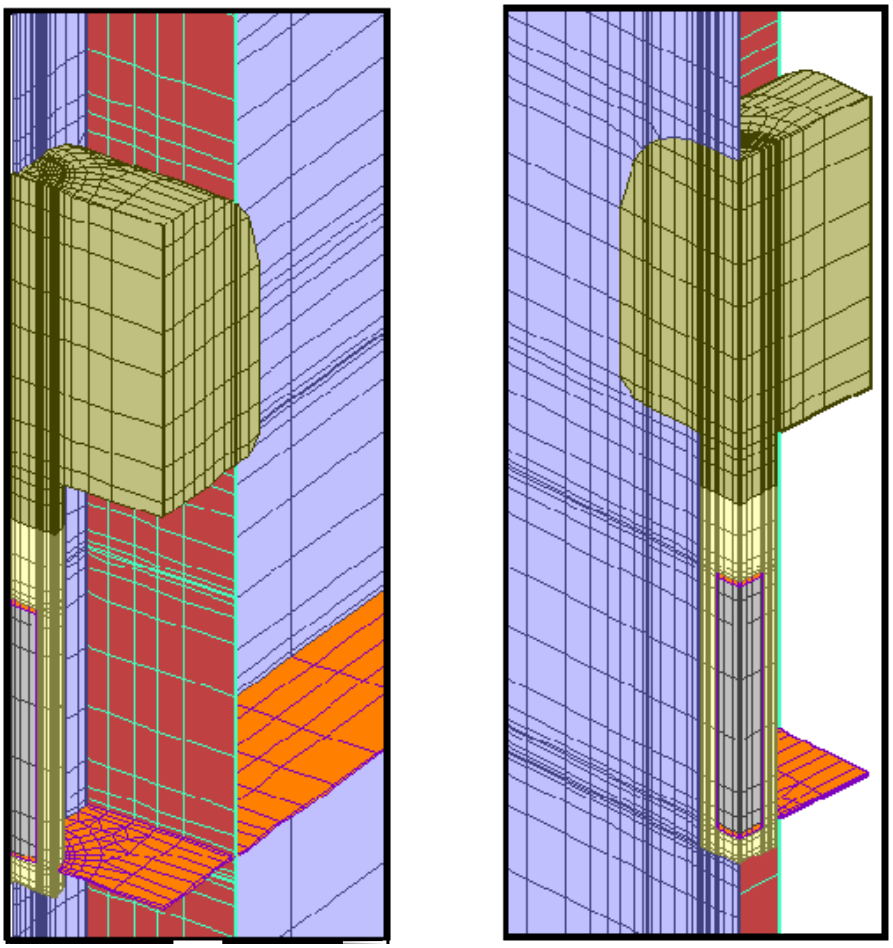

Figure 4.1-2. Some of the discrete fractures that may be activated in the quarter symmetric finite element model. Left and right figure shows the same model from two different angles.

4.2 Modeling sequences, boundary and initial conditions

Figure 4.2-1 presents the modeling sequence, along with boundary and initial conditions, for a coupled THM simulation. The initial conditions for the rock mass are defined at the pre-excavation stage (Figure 4.2-1a). The vertical gradients of temperature, fluid pressure, and *in situ* stress gradients applied for each site are given in Table 4.6. The horizontal stresses are the most uncertain of the parameters given in Table 4.6. Average values evaluated for each of the sites have been applied in the basic ideal case. For the Forsmark repository alternative, the tunnels are oriented parallel to the maximum stress as defined in SR-Can (SKB 2006a). For the Laxemar repository alternative, SR-Can specifies that the tunnels at the 500 m depth option should be oriented to make best use of available space without consideration of stress orientation. The repository layout indicates tunnel orientations at variable angles relative to the maximum principal stress, with some tunnels oriented almost normal to the maximum principal stress. In our modeling, we assumed the most unfavorable

case of tunnels oriented with their axis normal to the maximum principal stress. However, since the initial stress horizontal stress field is an uncertain parameter, we performed a parameter study by varying the initial horizontal stress field between extreme values for both Forsmark and Laxemar cases.

The excavation sequence (excavation and operational period) is simulated for 10 years, with the elements in the tunnel removed and with fixed relative humidity (Figure 4.2-1b). In the base case, a relative humidity of 100% was used. After 10 years, the waste canister, bentonite buffer, and backfill are installed instantaneously and the postclosure simulation can start (Figure 4.2-1c and d). The postclosure simulation is conducted for 100,000 years until the temperature and fluid pressure have been restored to ambient conditions.

Table 4-6. Initial pressure, temperature, and stress for modeling of Forsmark and Laxemar sites.

	Forsmark	Laxemar
Initial pressure, P (MPa)	$P \approx 0.00981 \times z_d$ (hydrostatic)	$P \approx 0.00981 \times z_d$ (hydrostatic)
Initial temperature, T (°C)	$T = 6.0+0.012 \times z_d$ (Fitted to measured values in Figure 7-4 of the Forsmark site descriptive model [SKB 2005])	$T = 6.0+0.016 \times z_d$ (Fitted to measured values in Figure 7-4 of the Laxemar site descriptive model [SKB 2006b])
Initial vertical stress, σ_z (MPa)	$\sigma_z = 0.0265 \times z_d$ (Forsmark site descriptive model, SKB 2005, Table 6-10, Figure 6-16)	$\sigma_z = 0.027 \times z_d$ (Laxemar site descriptive model, SKB 2006b, Table 6-9)
Initial horizontal stress normal to tunnel axis, σ_x (MPa)	$\sigma_x = 10.0+0.012 \times z_d$ for $z_d \leq 250$ m $\sigma_x = 19.0+0.025 \times z_d$ for $z_d \geq 250$ m (Forsmark site descriptive model, SKB 2005, Table 6-9 and Figure 6-16 and assuming σ_x = 10 MPa stress at ground surface)	$\sigma_x = 5.0+0.0587 \times z_d$ (Laxemar site descriptive model, SKB 2006b, Table 6-9 and assuming maximum principal compressive stress normal to tunnel axis)
Initial horizontal stress along tunnel axis, σ_y (MPa)	$\sigma_y = 5.0+0.081 \times z_d$ for $z_d \leq 250$ m $\sigma_y = 35.0+0.020 \times z_d$ for $z_d \geq 250$ m (Forsmark site descriptive model, SKB 2005, Table 6-9 and Figure 6-16 and assuming σ_y = 5 MPa stress at ground surface)	$\sigma_y = 3.0+0.014 \times z_d$ (Laxemar site descriptive model, SKB 2006b, Table 6-9 and assuming maximum principal compressive stress normal to tunnel axis)

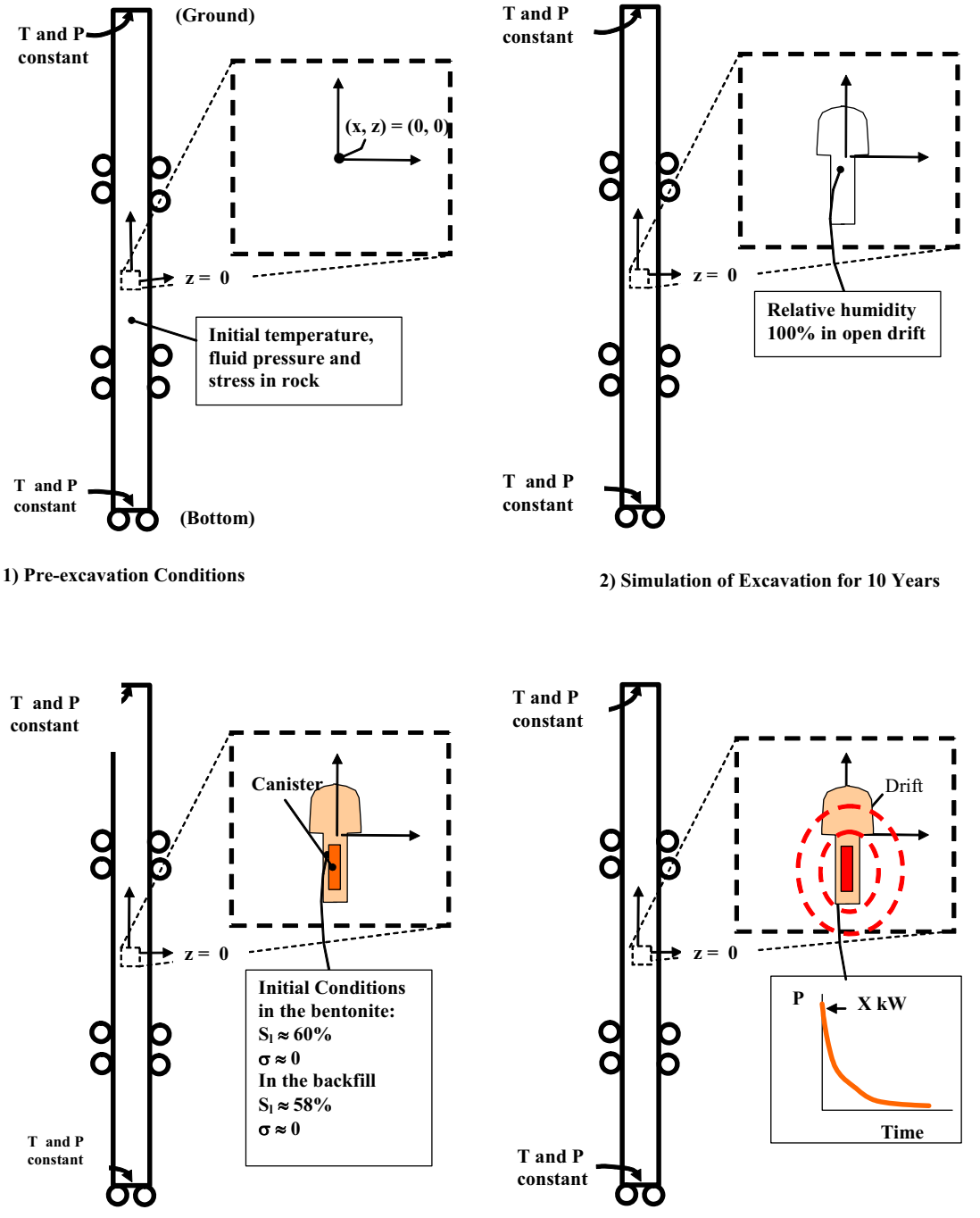

Figure 4.2-1. Specific modeling sequence (step1 to 4), including boundary and initial conditions, for Forsmark and Laxemar repository alternatives.

4.3 Approach and parameters for mechanical failure analysis

In this study we analyze the potential for rock failure rather than a full analysis of the failure process. The approach is to calculate the evolution of the stress field and then apply a failure criterion to investigate the potential for failure. Two alternative failure criteria are used: a spalling criterion based on observed *in situ* compressive strength and the Mohr-Coulumb criterion using SKB's derived rock-mass strength parameters.

The simple failure criterion under compressive stress expressed by D. Martin (e.g., Martin, 2005) stipulates that spalling of the unsupported rock wall would be initiated when the maximum principal compressive stress exceeds about 50% of the short-term uniaxial compressive strength determined on core samples. At Forsmark, the short-term uniaxial compressive strength determined from core samples on granite and granodiorite has a mean value of 225 MPa, with a standard deviation of 22 MPa (Forsmark site descriptive model, SKB [2005], Table 6-5). At Laxemar, the uniaxial compressive strength on Ävrö granite has a mean of 195 MPa with a standard deviation of 20 MPa (Laxemar site descriptive model, SKB [2006b], Table 6-5). The corresponding *in situ* compressive strength would be 112.5 MPa at Forsmark and 97.5 MPa at Laxemar. We will use these values of mean *in situ* compressive strength and compare those to the evolution of stresses around the tunnel and deposition hole.

An alternative Mohr-Coulomb criterion (Jaeger and Cook, 1979) is used to investigate the potential for rock failure. One advantage with a Mohr-Coulomb criterion over the above mentioned spalling criterion is that the Mohr-Coulomb criterion considers the effect of the confining pressure that may develop at the walls of the tunnel and deposition holes as the bentonite swells and provides support load to the rock walls. The importance of the confining pressure from the bentonite buffer have been demonstrated in the Äspö pillar stability experiment (SR-Can, SKB 2006a, Section 9.2.2). In our simulation study, we apply the Mohr-Coulomb criterion using the rock-mass strength parameters (cohesion and fiction angle) developed by SKB in the site descriptive models. All the strength parameters are listed in Table 4-7. The Mohr-Coulomb criterion may be expressed in the following form:

$$\sigma'_{1c} = C_0 + q\sigma'_3 \tag{4-1}$$

where C_0 is the uniaxial compressive strength, which can be calculated from cohesion, S_0, and the coefficient of friction, $\mu = \tan\phi$, as:

$$C_0 = 2S_0\left[\left(\mu^2 + 2\right)^{1/2} + \mu\right] \tag{4-2}$$

and q is the slope which can be calculated from the coefficient of friction as:

$$q = \left[\left(\mu^2 + 1\right)^{1/2} + \mu\right]^2 \tag{4-3}$$

The rock mass uniaxial compressive strength calculated by the Mohr-Coulomb criterion is slightly higher than 50% of intact-rock uniaxial compressive strength for Forsmark whereas it is lower than 50% for Laxemar. The lower rock-mass compressive strength at Laxemar is a result of a denses fracture network, which is considered in the evaluation of the rock-mass strength parameters.

Table 4-7. Material parameters for failure analysis.

	Forsmark	Laxemar
Mean of Uniaxial Compressive Strength of intact rock from core samples	225 MPa (Forsmark site descriptive model, SKB 2005, Table 6-5)	195 MPa (Laxemar site descriptive model, SKB 2006b, Table 6-5)
In situ compressive strength for spalling criterion, UCS	112.5 MPa (50% of uniaxial compressive strength)	97.5 MPa (50% of uniaxial compressive strength)
Mohr-Coulomb rock mass compressive strength, C_0 or MCUCS	127 MPa (Forsmark site descriptive model, SKB 2005, Table 6-7)	82 MPa (Laxemar site descriptive model, SKB 2006b Table 6-7)

4.4 Results for an ideal base case

We first present the results for an ideal base case, in which the resaturation of the buffer is timely because of relatively high rock permeability. In this ideal case, the properties of the bentonite buffer are those determined by model calibration against SKB's laboratory experiments. Moreover, the elastic properties of the rock mass are representative for an average fractured rock mass at the respective sites. In the ideal case, no significant desaturation of the rock is expected, because the rock permeability is high and because we assume 100% relative humidity in the open excavations during the operational phase. Moreover, we assume that the tunnels are backfilled with 30/70 backfill, which has a higher permeability than the Friedland Clay backfill option. For the Laxemar repository, we assume that the tunnels are oriented perpendicular to the tunnel axis, which may not be an ideal tunnel orientation from a rock mechanical viewpoint. However, according to the repository layout in SR-Can, many emplacement tunnels at the Laxemar site would be oriented nearly perpendicular to the maximum horizontal principal stress, and hence our ideal base case is realistic at least for parts of a Laxemar repository.

4.4.1 Temperature evolution and maximum temperature

Figure 4.4-1 presents the decay function of heat power in the simulated waste canister, as well as temperature evolution at two points in the buffer and one point located away from the emplacement tunnels. Vertical temperature profiles are presented in Figure 4.4-2. Figure 4.4-1 shows that maximum temperatures of 72°C (for Forsmark) and 75°C (for Laxemar) are attained at the canister surface at about 10 to 20 years after waste emplacement. At the buffer/rock interface, a maximum temperature of 52°C is attained after about 40 years. At 10,000 years, the heat power is down to a few percent of its initial value and the temperature has declined to about 27°C, which is still substantially higher than the ambient temperature.

The peak temperatures obtained by our calculations are slightly lower than that obtained by SKB in their thermal analysis. SKB used an analytical solution of a line

heat source and determined a canister spacing that would result in a peak temperature of about 80°C at the canister surface (SR-Can, SKB 2006a, Section 9.3.4). Our analyses indicate peak temperatures of about 72 and 75°C, respectively at the Forsmark and Laxemar sites. However, SKB's analysis was made for a thermal conductivity of the buffer equal to 1.1 W/(mK) representing some initial unsaturated conditions (SR-Can, SKB 2006a, Table 9-4), whereas in our simulations the buffer is fully resaturated with a thermal conductivity of 1.3 W/(mK) at the time of peak temperature. On the other hand, SKB also included a 0.03 m gap at the buffer/rock interface, which is not considered in our analysis. At the rock wall, SKB's thermal analysis indicates a temperature of about 60°C (SR-Can, SKB 2006a, Figure 9-17), whereas our analysis indicates 52°C. We could also compare our results to a similar three-dimensional analysis presented in Börgesson et al. (2006). In that analysis the canister spacing was set to 6 m, corresponding to a repository at Forsmark, but the tunnel distance was set to 30 m instead of 40 m. The peak temperature calculated by Börgesson et al. (2006) using those conditions were 89°C, which is substantially higher than both our analysis and SKB's thermal analysis.

4.4.2 Evolution of buffer saturation and fluid pressure

Figure 4.4-3 presents the evolution of liquid saturation in the buffer and backfill. The evolution of saturation is very similar for Forsmark and Laxemar, because the hydrological properties are assumed to be the same, with relatively high rock permeability, for this ideal case. At the top of the canister, the liquid saturation in the buffer first decreases to a minimum of about 35% after a few years, then starts to increase, and finally reaches full saturation at about 10 to 20 years. The resaturation at the top of the canister is much slower than at the side of the canister. Near the side of the canister, as well as in the backfilled tunnel, the resaturation takes only about 5 years.

Figure 4.4-4 presents the evolution of fluid pressure at one point within the buffer and one point in the rock outside the buffer. By the time of full saturation in most of the buffer, the fluid pressure within the buffer and rock is almost, but not completely, restored. However, the fluid pressure then increases at a much slower rate and is not completely restored to hydrostatic pressure until more than 2,000 years.

The time to full resaturation of the buffer is similar to that estimated by SKB's analysis for the case of high rock permeability. For example, Börgesson et al. (2006) calculated a time to complete resaturation of the buffer to be on the order of 10 years. Our analysis shows a time to full resaturation of the buffer ranging from 10 to 20 years. The agreement is good, despite the model geometries and distance to some hydraulic outer boundary conditions being different. The results may be insensitive to the outer boundary conditions in this case, because resaturation is controlled by the hydraulic properties of the bentonite and an unlimited water supply from the surrounding rock.

4.4.3 Evolution of stress in the buffer

Figure 4.4-5 presents the evolution of total stress in the buffer and backfill. The final total stress within the buffer and backfill depends on several components. First, the bentonite and backfill swells as a result of resaturation. This swelling can give rise to a swelling stress of about 9 MPa in the buffer and 3 MPa in the backfill. After the

bentonite is fully saturated, the fluid pressure increases from 0 to 4 MPa (at Forsmark) and 0 to 5 MPa (at Laxemar), which is the hydrostatic fluid pressure at 400 and 500 m depth, respectively. Assuming Biot's $\alpha = 1.0$ for the bentonite and backfill, a 4 or 5 MPa pressure increase could give rise to an increase in total stress of about 4 and 5 MPa, respectively. For a repository at 400 m depth at Forsmark, the total stress developed from the swelling stress (which is an effective stress) and the fluid pressure is 9 + 4 = 13 MPa in the buffer and 3 + 4 = 7 MPa in the backfill. Similarly, for a repository at 500 m depth at Laxemar, the total stress developed is 9 + 5 = 14 MPa in the buffer and 3 + 5 = 8 MPa in the backfill. In addition to the stress created by resaturation and fluid pressure restoration, thermal expansion may give rise to an additional small component of compressive stress during elevated temperature. The total stress in the buffer and backfill is fully developed after 10 to 20 years.

The evolution of stress in the buffer is not explicitly presented in SR-Can and its supporting documents, but we may assume that the evolution is similar to our analysis, since it correlates well with the evolution of saturation in the buffer.

4.4.4 Evolution of stress in the rock and possible failure

Figure 4.4-6 and 4.4-7 present profiles of vertical and horizontal stresses in the rock. Thermal stress in the horizontal direction develops where temperature increases and peaks around 100 to 1,000 years. In general, the initial horizontal stresses are higher in the Forsmark case. The magnitude of thermal stress, e.g., the stress at 1,000 years minus the initial stress, is also higher in the Forsmark case. The reason for a higher thermal stress at Forsmark is that the rock mass is less fractured and hence less compliant than at Laxemar. Another observation from Figure 4.4-5 is that at Forsmark, the horizontal stress field has a higher degree of anisotropy, which can lead to higher stress concentrations around the underground openings. Moreover, a higher degree of anisotropy implies higher shear stress, which might lead to a higher potential for shear reactivation along pre-existing fractures.

Figure 4.4-8 presents contours of minimum and maximum principal stresses after excavation and after 1,000 years. Figure 4.4-8 shows that a zone of tensile stress develops at the side wall of the tunnel for both Forsmark and Laxemar repository alternatives. The direction of the tensile stresses in the side wall is parallel to the tunnel wall, and hence if the rock fails in tension, radial fractures could develop. This zone of tensile stress develops because the horizontal stress normal to the tunnel axis (σ_y) is much higher than the vertical stress. Figure 4.4-8 also shows that there is a high concentration of compressive stresses on the side wall of the deposition hole, especially near the floor of the overlying tunnel. The compressive stress is actually higher in the case of Laxemar. This is because the horizontal stress field is initially more anisotropic, and the maximum principal horizontal stress is oriented normal to the tunnel axis.

Figure 4.4-9 presents the evolution of the safety factor defined as the ratio of current to critical maximum principal effective stress, i.e. σ_{1c}/σ_1, where σ_{1c} is calculated from the Mohr-Coulomb criterion. For both Forsmark and Laxemar repository alternatives, a zone of failure develops in the wall of the tunnel, corresponding to the zone of tensile stress observed in Figure 4.4-8. In the case of Forsmark, failure in the rock wall develops after emplacement and backfill of the tunnels, whereas at Laxemar the

failure occurred already during excavation. The results in Figure 4.4-9 also shows that in the case of Forsmark, no failure would occur near the deposition hole, whereas in the case of Laxemar failure would occur near the deposition hole already during the excavation phase. Thus, the analysis indicates a higher potential for spalling at the Laxemar repository alternative.

Figures 4.4-10 and 4.4-11 present the evolution of principal stresses at a few key points around the deposition hole and around the tunnel. Figures 4.4-12 and 4.4-13 show the path of minimum and maximum principal effective stresses in relation to the Mohr-Coulomb failure envelopes. Figures 4.4-10 and 11 show that compressive stresses in the walls of the deposition hole and tunnel exceed the uniaxial compressive strength at several locations. However, swelling pressure from the buffer and the backfill provide enough support to prevent failure from occurring at several of the highly stressed points. Figure 4.4-12 shows that the stress state at Forsmark stays below that required for failure, except at points E3, E4, and E7, at which tensile failure may occur. Figure 4.4-13 shows that at Laxemar, compressive shear failure may occur in E1 and E3, whereas tensile failure could occur at E2, E4, and E7.

The evolution of the thermal stresses obtained by our analysis is very similar to that of SKB's as presented in Hökmark et al. (2006). The time evolution of maximum principal stress shown in Figure 4.4-7 is very similar to that calculated by Hökmark et al. (2006) for points E1 and E2. For points E3 and especially E4, Hökmark et al. (2006) calculates a higher maximum compressive stress than in our analysis. Both our analysis and that of SKB indicates a high potential for spalling at both Forsmark and Laxemar. Our analysis agrees with the analysis by Hökmark et al. (2006), which shows that during the operational phase there is a higher risk of spalling at the Laxemar site than at Forsmark. Moreover, our analysis using a Mohr-Coulomb criterion actually indicates that at both Forsmark and Laxemar, the development of swelling would prevent any further spalling during the thermal period. SKB has taken a conservative approach, assuming that spalling could occur if maximum principal stress exceeds the rock-mass strength, without accounting for the benefits of the bentonite swelling.

The potential for tensile fracturing in the tunnel wall is not discussed in SR-Can (SKB 2006a) or in the supporting document by Hökmark et al. (2006). Our analysis shows that tensile stress would develop in the tunnel wall at both sites. Such fracturing may have the consequence of forming a continuous zone of increased permeability along the tunnel axis.

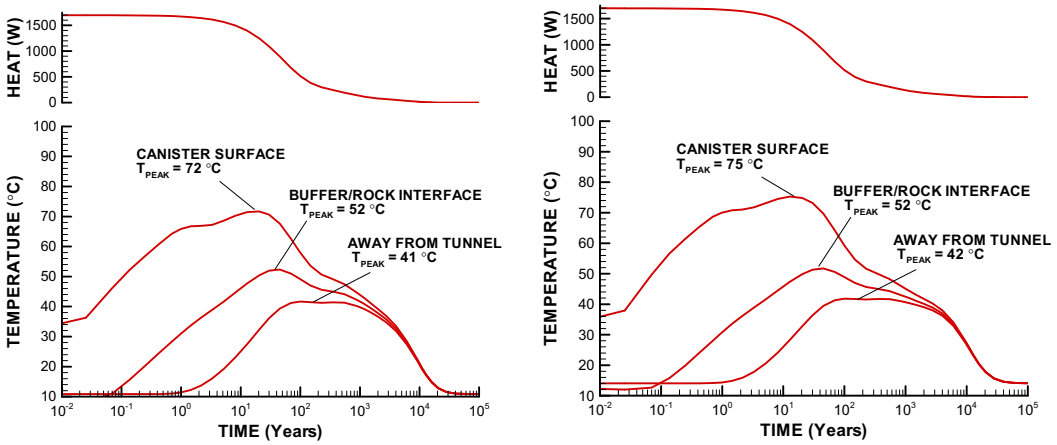

(a) Forsmark (b) Laxemar

Figure 4.4-1. Evolution of power and temperature for a repository located at (a) Forsmark and (b) Laxemar for the ideal case.

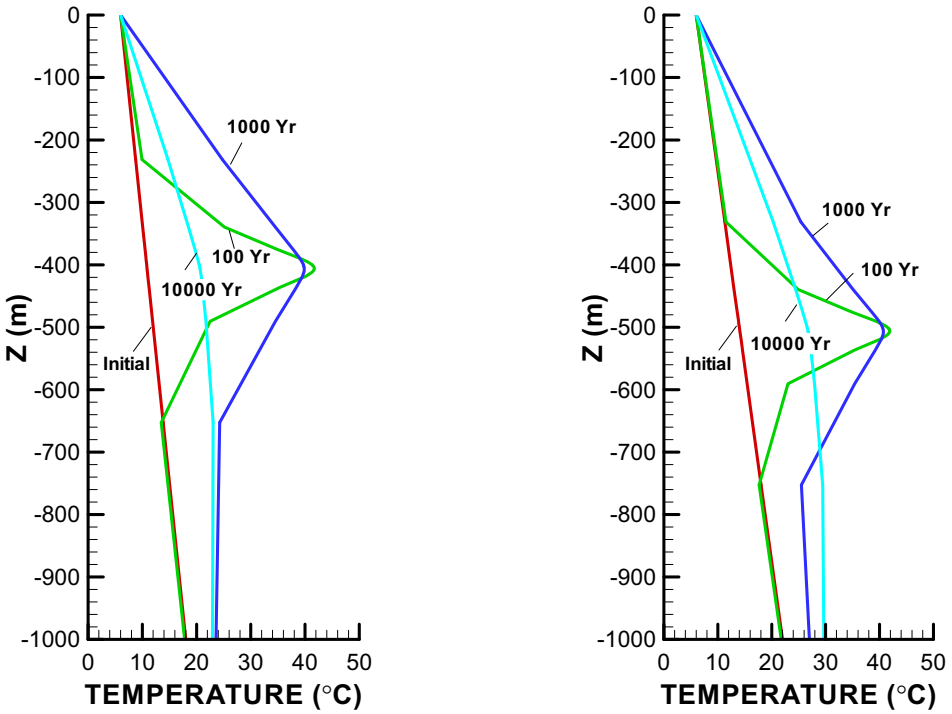

(a) Forsmark (b) Laxemar

Figure 4.4-2. Profiles of rock temperature for a repository located at (a) Forsmark and (b) Laxemar for the ideal case.

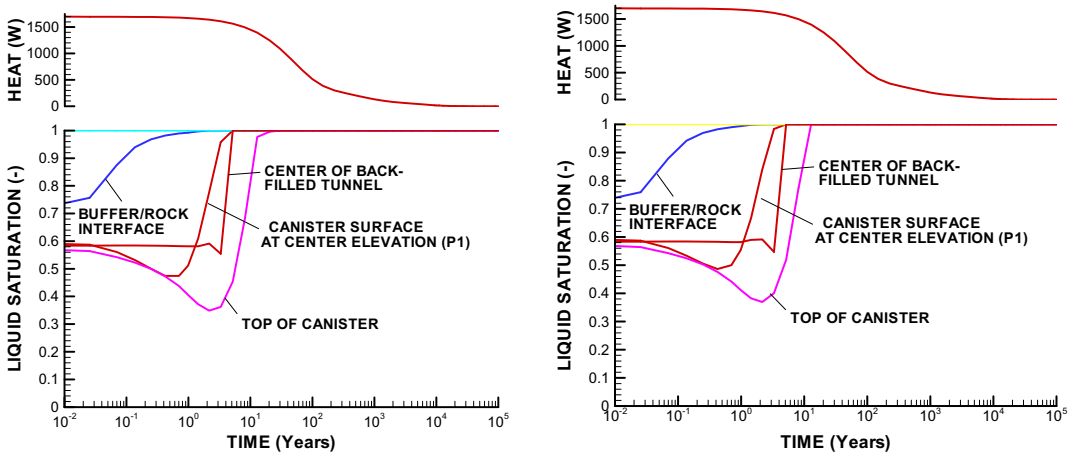

(a) Forsmark (b) Laxemar

Figure 4.4-3. Evolution of saturation for a repository located at (a) Forsmark and (b) Laxemar for the ideal case (see locations of monitoring points in Figure 4.1-1b).

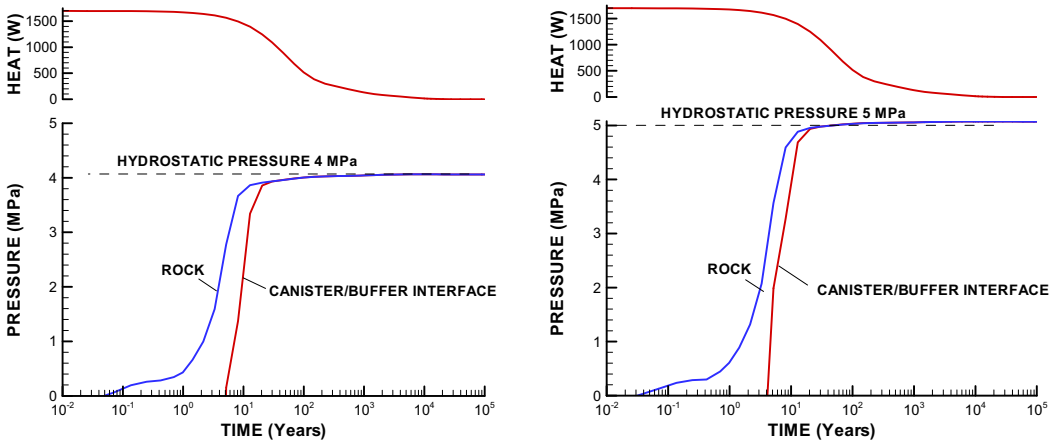

(a) Forsmark (b) Laxemar

Figure 4.4-4. Evolution of fluid pressure for a repository located at (a) Forsmark and (b) Laxemar for the ideal case.

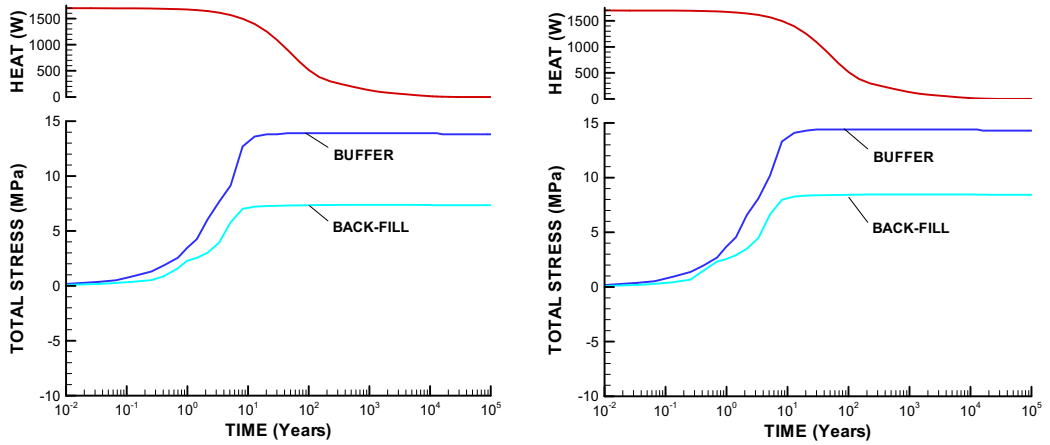

(a) Forsmark (b) Laxemar

Figure 4.4-5. Evolution of total stress in buffer and backfill for a repository located at (a) Forsmark and (b) Laxemar for the ideal case.

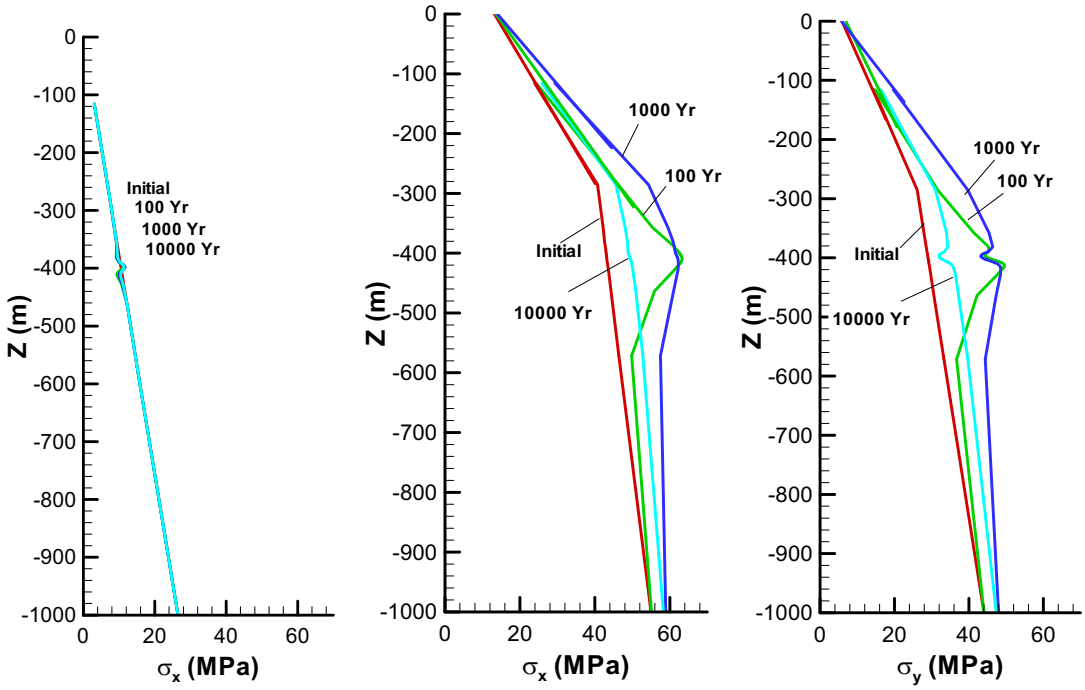

(a) (b) (c)

Figure 4.4-6. Profiles of vertical and horizontal stresses for a repository located at Forsmark: (a) vertical stress, (b) horizontal stress normal to the tunnel axis and (c) horizontal stress along the tunnel axis.

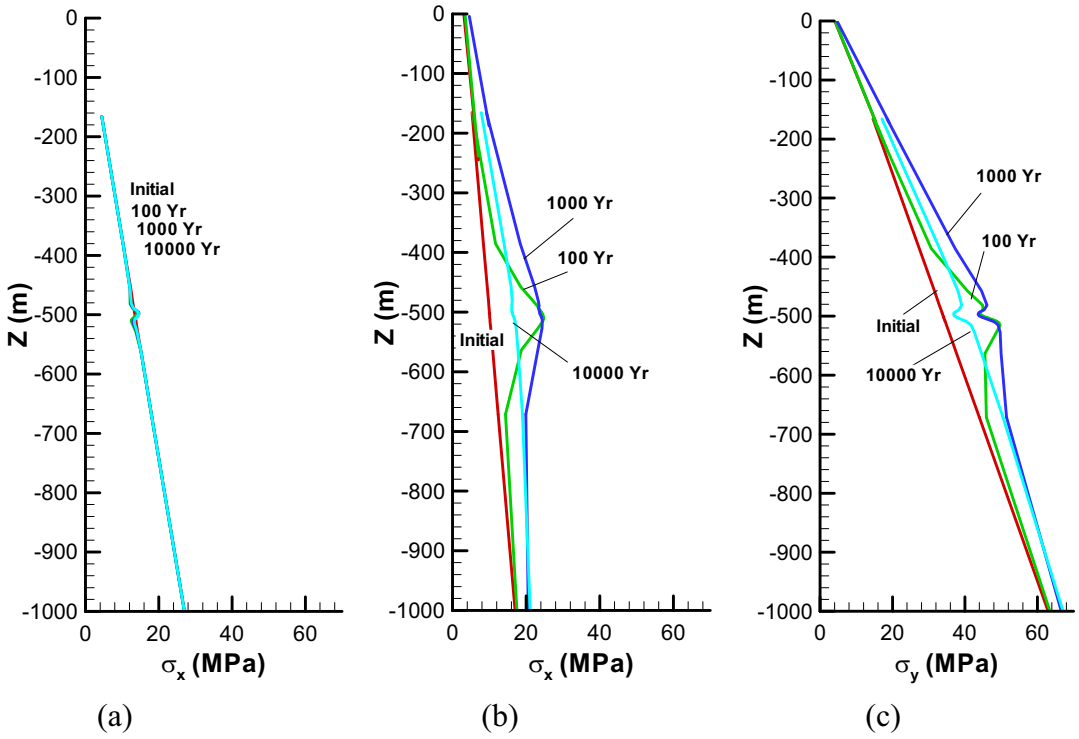

Figure 4.4-7. Profiles of vertical and horizontal stresses for a repository located at Laxemar: (a) vertical stress, (b) horizontal stress normal to tunnel axis and (c) horizontal stress along tunnel axis.

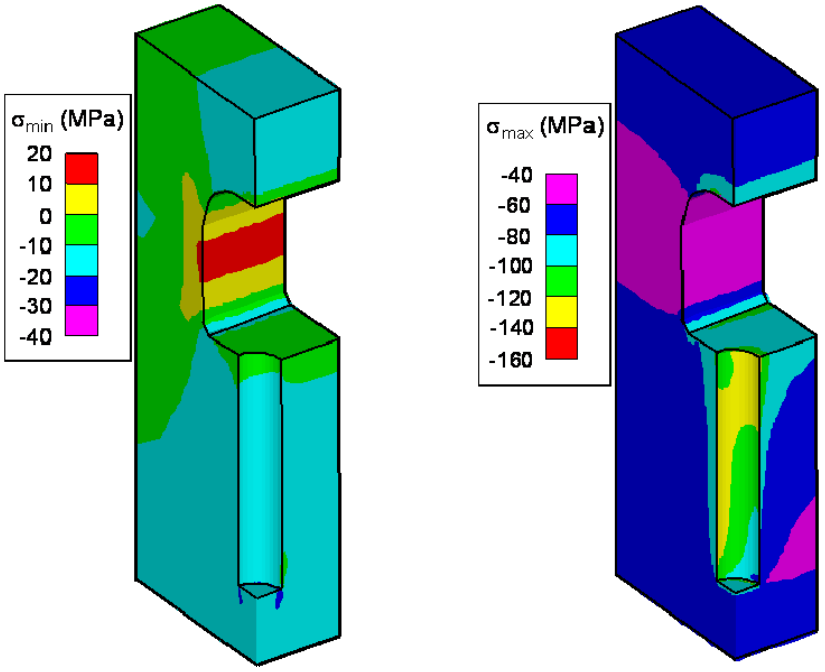

(a) Forsmark

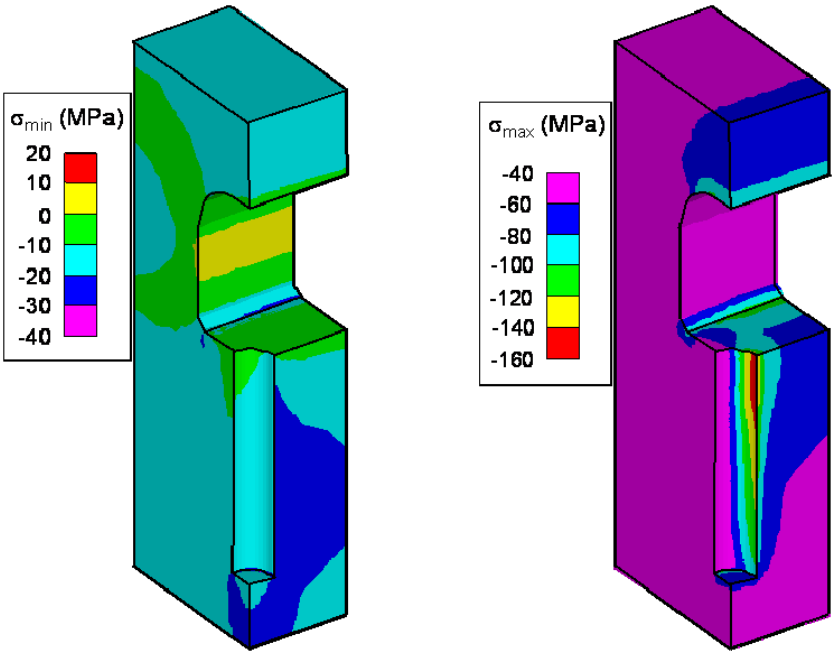

(b) Laxemar

Figure 4.4-8. Maximum (σ_{max}) and minimum (σ_{min}) compressive principal stresses after 1,000 years for a repository located at (a) Forsmark and (b) Laxemar for the ideal case.

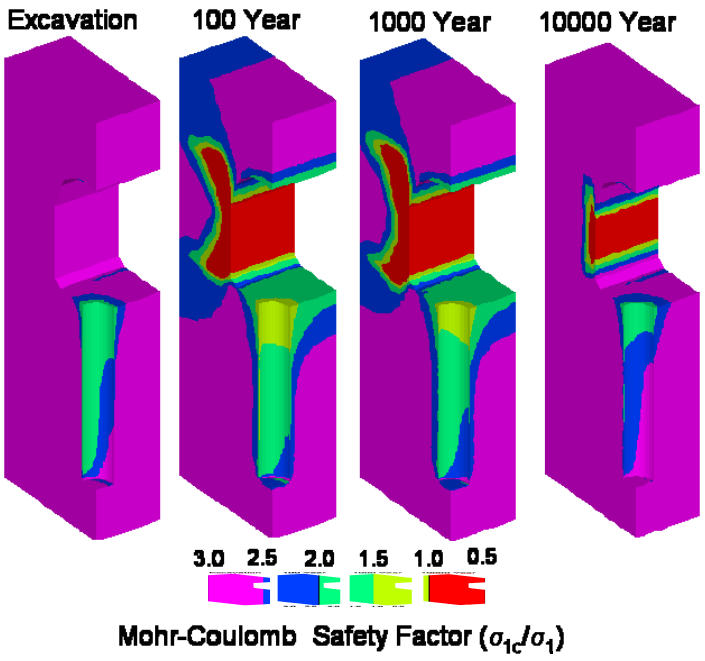

(a) Forsmark

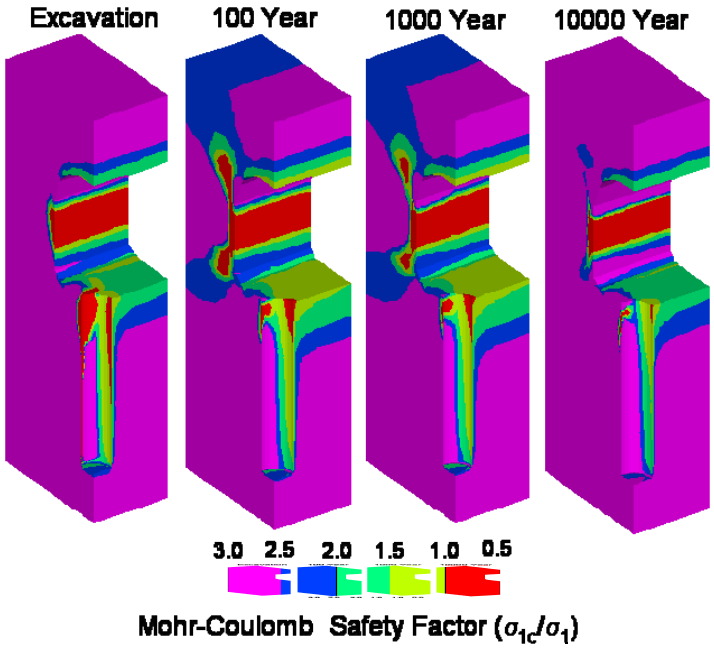

(b) Laxemar

Figure 4.4-9. Evolution of Mohr-Coulomb safety factor (σ_{1c}/σ_1) for a repository located at (a) Forsmark and (b) Laxemar for the ideal case. Red contour indicates zone of highest potential for failure, as the current maximum principal stress exceeds the critical stress for failure.

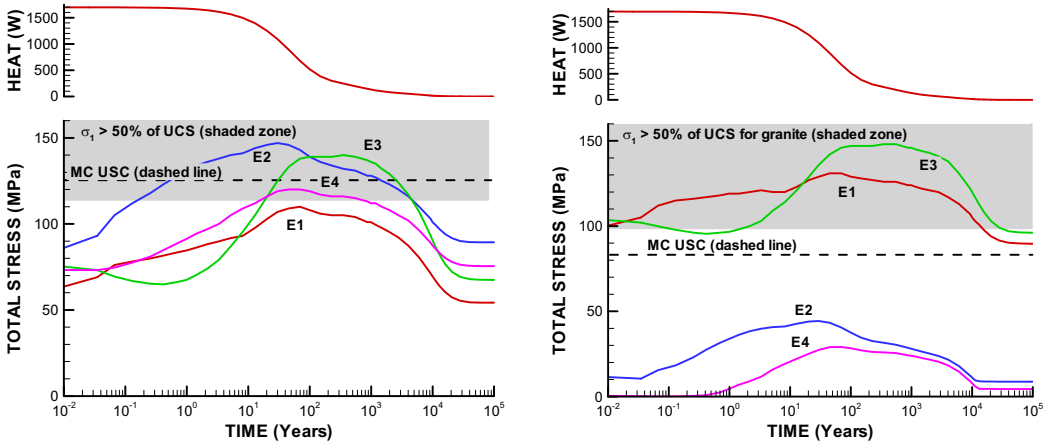

(a) Forsmark (b) Laxemar

Figure 4.4-10. Evolution of maximum compressive principal effective stress at four points located at the periphery of the deposition hole with comparison to uniaxial compressive strength estimated by two different methods (see locations of monitoring points in Figure 4.1-1b).

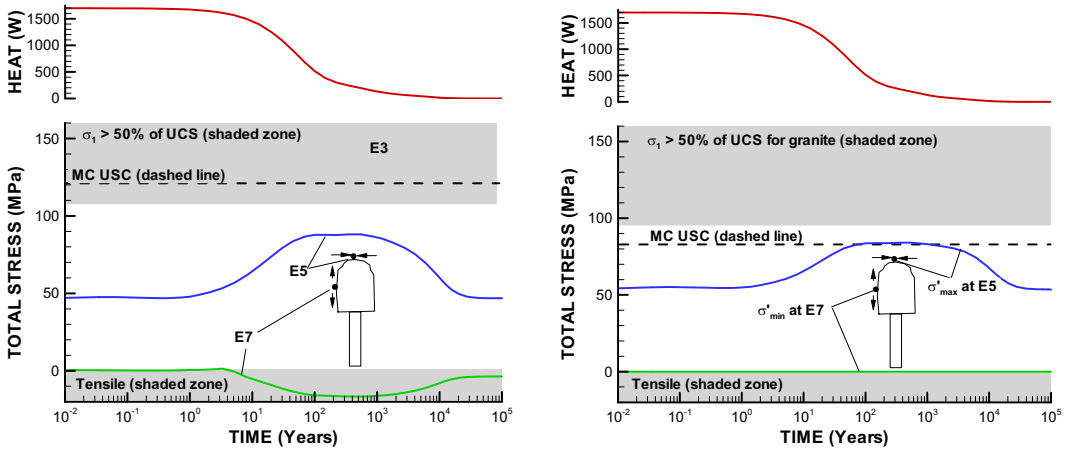

(a) Forsmark (b) Laxemar

Figure 4.4-11. Evolution of principal effective stresses at two points located at the periphery of the emplacement tunnel, with comparison to uniaxial compressive strength estimated by two different methods.

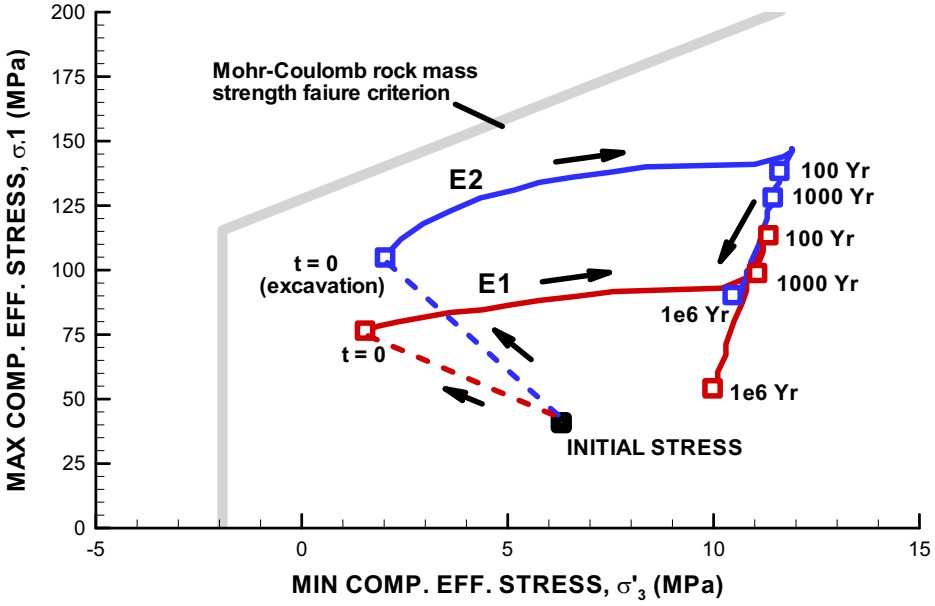

(a) Point E1 and E2

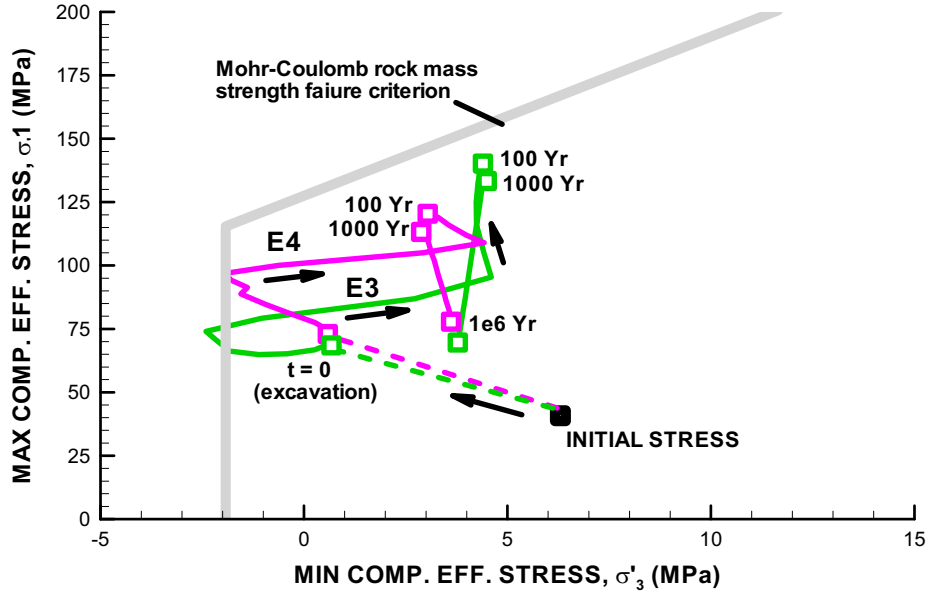

(b) Point E3 and E4

Figure 4.4-12. Principal stress path in relation to Mohr-Coulomb rock-mass failure criterion for a repository located at Forsmark (see locations of monitoring points in Figure 4.1-1b).

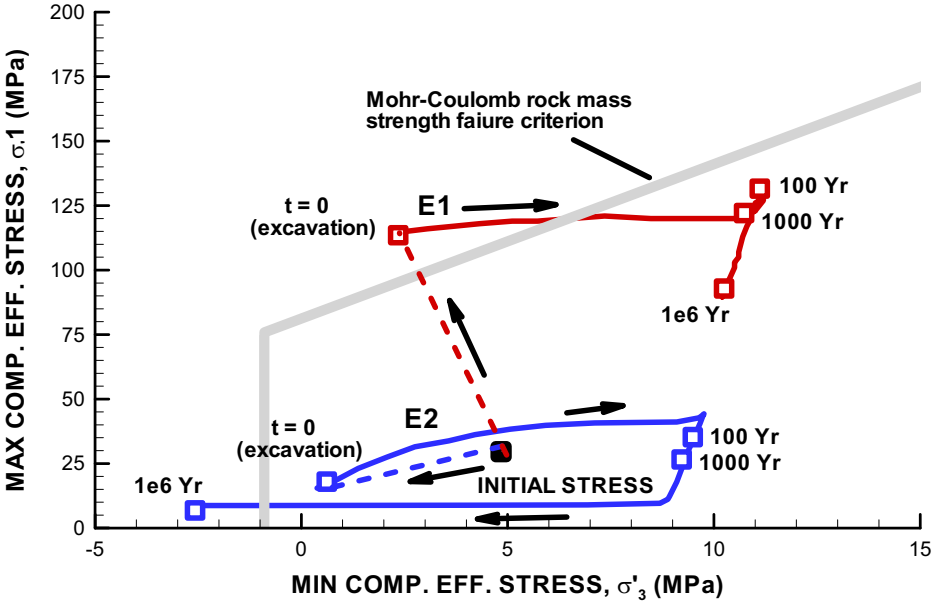

(a) Point E1 and E2

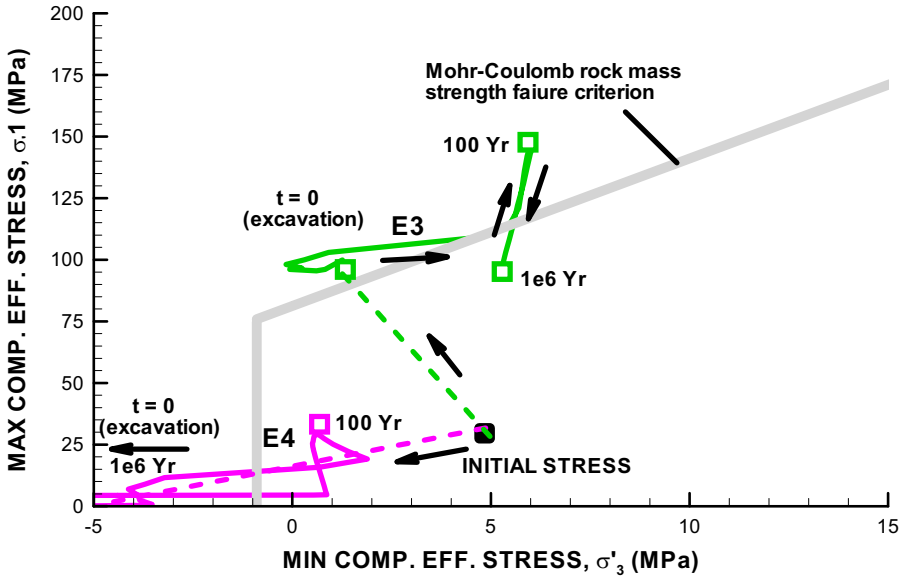

(b) Point E3 and E4

Figure 4.4-13. Principal stress path in relation to Mohr-Coulomb rock-mass failure criterion for a repository located at Laxemar (see locations of monitoring points in Figure 4.1-1b).

4.5 Case of extremely low rock permeability

In this section, we study the extreme case of a very low rock-mass permeability of k = 1×10^{-20} m^2, with all other properties and conditions unchanged from the ideal case. This case corresponds to a rock hydraulic conductivity of K = 1×10^{-13} m/s, which is the minimum hydraulic conductivity used in SKB's THM analysis (e.g., in Börgesson et al. 2006). In general, this extremely low rock permeability results in a much delayed resaturation of the buffer. This in turn may lead to increased peak temperature and a delayed development of swelling stress that may affect the stability of the underground openings.

4.5.1 Temperature evolution and maximum temperature

Figure 4.5-1 shows that maximum temperatures of 86°C (for Forsmark) and 91°C (for Laxemar) are attained at the canister surface at about 10 to 20 years after the waste emplacement. Thus, compared to the ideal case presented in Section 4.4, the peak temperature has increased by 14°C (from 72 to 86°C) for Forsmark and by 16°C (from 75 to 91°C) for Laxemar. This increase in temperature is caused by a lower thermal conductivity in buffer, because it is much dryer in this case. At the buffer/rock interface and in the rock surrounding the buffer, the temperature evolution is unchanged from that of the ideal case.

4.5.2 Evolution of buffer saturation and fluid pressure

Figure 4.5-2 presents the evolution of liquid saturation in the buffer and backfill. Again, the evolution of saturation is very similar for Forsmark and Laxemar repository alternatives, because the rock permeability is assumed to be the same. The time to full (about 100%) resaturation is 40,000 years at Forsmark and 30,000 years at Laxemar. The slightly faster resaturation at Laxemar is caused by the higher hydrostatic fluid pressure, because the repositor at Laxemar is located at a depth of 500 m compared to 400 m at Forsmark.

Figure 4.5-3 shows the distribution of liquid saturation for a repository at Forsmark (the distribution of liquid saturation for a repository at Laxemar is very similar and is therefore not shown). The figure shows that the rock gets desaturated around the deposition hole by suction from the buffer, whereas there seems to be no significant desaturation around the backfilled tunnel. This pattern of desaturation of rock is caused by the differences in water-retention properties for rock, buffer, and backfill, as discussed in Section 3.2. A close examination of the simulated results showed that the rock is in fact also desaturated around the backfilled tunnel. However, the saturation of the rock surrounding the tunnel is always higher than 0.95, i.e., almost fully saturated.

In this case, the rock permeability is so low that the buffer first gets resaturated by water supply from the initial water content in the overlying backfill. After about 2,000 years, the buffer has sucked water from the backfill, and is about 95% saturated (Figure 4.5-2). At the same time, the saturation in the backfill has decreased from an initial 58% to 48%. The buffer becomes fully resaturated (100%) once the backfill becomes fully resaturated by slow water supply from the surrounding low permeability rock. This takes between 30,000 to 40,000 years.

Figure 4.5-4 shows that the fluid pressure is not fully restored until about 100,000 years both in the rock and the buffer. This indicates that the time to complete resaturation and fluid pressure restoration is controlled by the hydraulic properties of the surrounding low permeability rock.

Our analysis of this case shows a much longer resaturation time than that of Börgesson et al. (2006) for the same low rock permeability. In the three-dimensional analysis by Börgesson et al. (2006) there is a fast resaturation of the buffer to above 95% in about 30 years, whereas it take 570 years for the buffer to be 100% saturated. In SR-Can, SKB (2006a, Section 9.3.8), this is interpreted as a 50-year resaturation time. In an alternative two-dimensional axial symmetric analysis in Börgesson et al. (2006), it takes 2,000 years to resaturate the buffer from the backfill alone. In our analysis, the first step to 95% saturation takes 2,000 years, whereas it takes as much as 30,000 to 40,000 years to achieve 100% saturation. A very long resaturation time obtained in our analysis is explained by the fact that the initial permeability in the backfill is very low. In fact, the initial permeability of the backfill is on the same order as the extremely low permeability rock. The low permeability of the backfill is caused by the sensitive relative-permeability function for the 30/70 backfill shown in Figure 3.2-1. At an initial saturation of 58%, the relative permeability is $k_r = S^{10} = 0.58^{10} = 4.3\times10^{-3}$. With an intrinsic permeability of 5×10^{-18} m^2, the initial absolute permeability in the backfill is 2.1×10^{-20} m^2. Moreover, as the saturation of the backfill decreases to 48%, the permeability of the backfill becomes 3.2×10^{-21} m^2, much lower than the surrounding rock. With such a low permeability in the backfill, we question whether it is at all possible to resaturate the buffer in 50 years as claimed in SR-Can. Another contributing reason for the disagreement between our analysis and that of SKB's might be the limited distance to an outer constant head hydraulic boundary in SKB's analysis. The effect of the distance to the outer hydraulic boundary will be investigated in Section 4.6 below.

4.5.3 Evolution of stress in the buffer

Figure 4.5-5 shows that development of total stress within the buffer and backfill is significantly delayed by the slow resaturation and pressure restoration process. Our analysis indicates development of a small tensile stress near the canister during the drying of the buffer, which lasts for several hundred years. The magnitude of this tensile stress may not be realistic, as we are using an elastic model that does not consider tensile failure in the buffer. Moreover, in reality there is a gap between the buffer and the rock that is not considered in the modeling. Development of tensile stress in our modeling is rather an indication that the initial gap would remain open during this period and may only close after several hundred years. Figure 4.5-4 also shows that the total stress increases in two steps, the first step to about 8 MPa at about 10,000 years, and the second step to about 13 or 14 MPa after about 100,000 years. The first step is related to swelling of the buffer as it gets resaturated, whereas the second step is caused by the fluid pressure restoration. The swelling or total stress in the backfill does not start to develop until 30,000 or 40,000 years; thus, the swelling stress is clearly lower than the 0.1 MPa required by the safety function indicator (see Section 2).

4.5.4 Evolution of stress in the rock and possible failure

In terms of rock-stress evolution, the main difference from the ideal case is the delayed resaturation and fluid-pressure restoration that affects the evolution minimum principal stress near the tunnel and the deposition hole. Most importantly, a lack of swelling implies that the bentonite provides little support to the rock walls, and there will be much less confinement of the rock surrounding the tunnel and deposition hole.

The potential for failure shown in Figure 4.5-6 can be compared with the corresponding Figure 4.4-9 for the ideal case. Such a comparison indicates that in the case of the extremely low permeability rock, the potential for rock failure (spalling) is higher near the deposition hole. The biggest difference is seen at 100 years, when the yellow and red zone of low safety factor (and high failure potential) is more extensive in Figure 4.5-6 than in Figure 4.4-9. Conversely, the zone of tensile failure in the wall of the tunnel is less extensive in Figure 4.5-6 (extreme low permeability) than in Figure 4.4-9 (ideal case). This indicates that the swelling of the backfill actually contributes to create the tensile stress in the wall of the tunnel. In the case of the extremely low rock permeability, the swelling of the backfill does not take place until after more than 10,000 years, and therefore much less tensile stresses are developed in the tunnel wall.

Figures 4.4-7 and 8 show the path of minimum and maximum principal effective stresses in relation to the Mohr-Coulomb failure envelops. The biggest difference with the ideal case occurs at points E1 and E2, a few meters below the tunnel floor (compare Figures 4.5-7 and 8 with corresponding Figures 4.4-12 and 13 for the ideal case). In the ideal case, shown in Figure 4.4-12 and 13, the potential for failure was highest right after excavation, before the stress state moves away from the failure envelope as the minimum principal stress increases. In the case of the extremely low rock permeability, on the other hand, the highest potential for rock failure occurs at about 100 years, when the thermal compressive stress is the highest and when the minimum principal stress is still very low. The minimum principal stress is still low at 100 years, because no swelling pressure has been developed within the buffer.

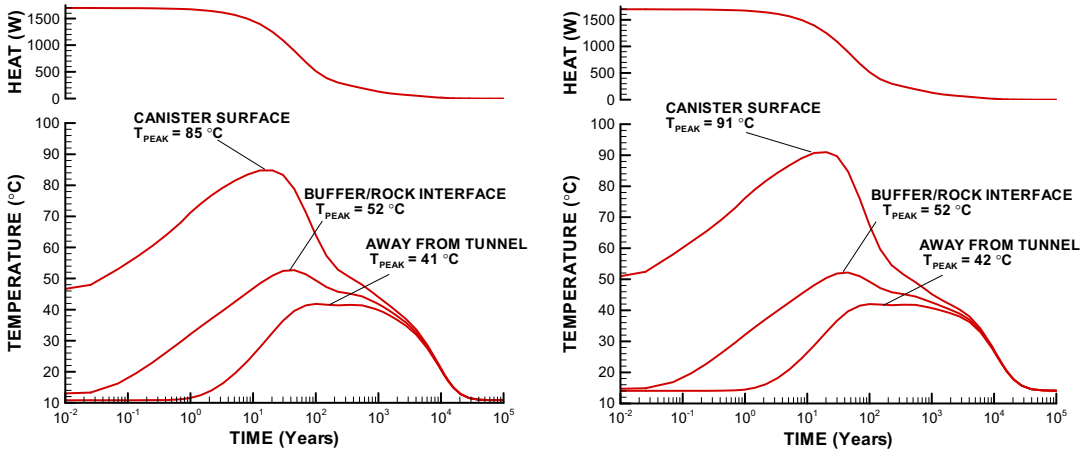

(a) Forsmark (b) Laxemar

Figure 4.5-1. Evolution of power and temperature for a repository located at (a) Forsmark and (b) Laxemar for the case of an extremely low rock permeability.

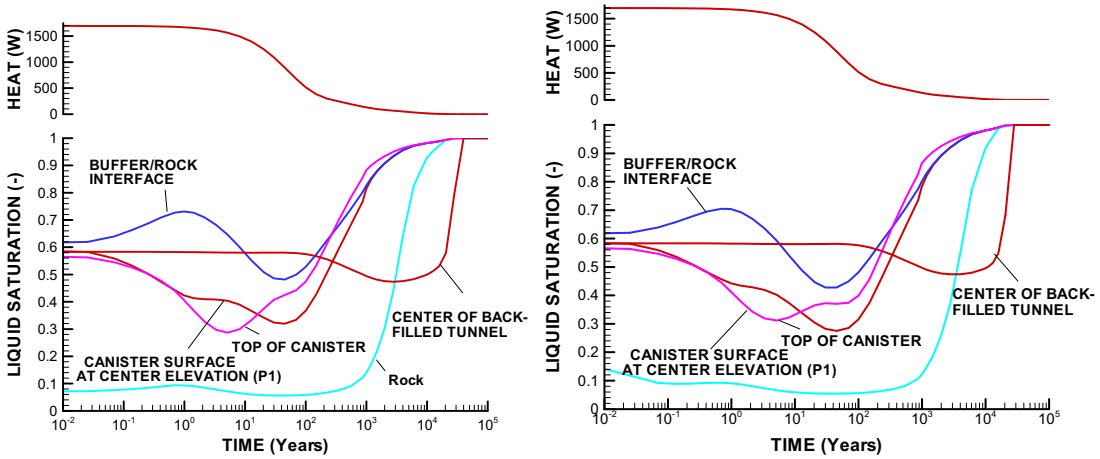

(a) Forsmark (b) Laxemar

Figure 4.5-2. Evolution of saturation for a repository located at (a) Forsmark and (b) Laxemar for the case of an extremely low rock permeability (see locations of monitoring points in Figure 4.1-1b).

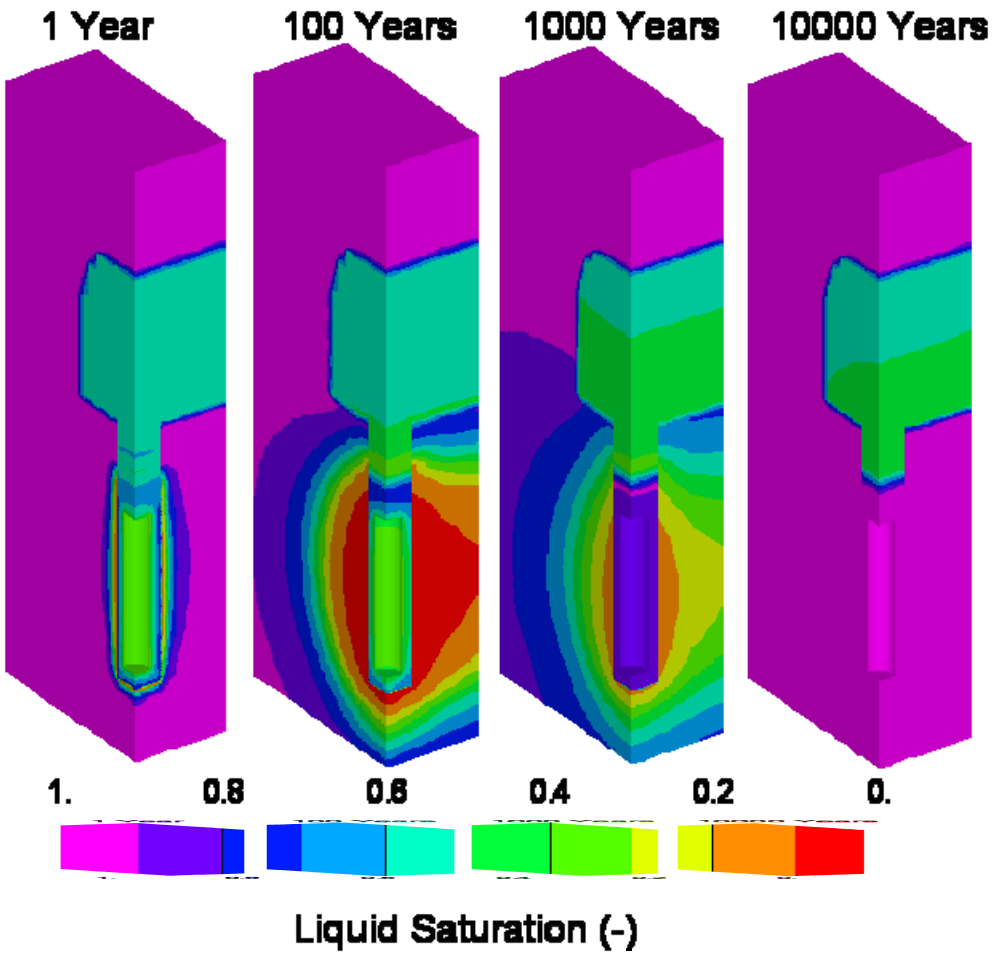

Figure 4.5-3. Distribution of liquid saturation for a repository located at Forsmark for the case of an extremely low rock permeability.

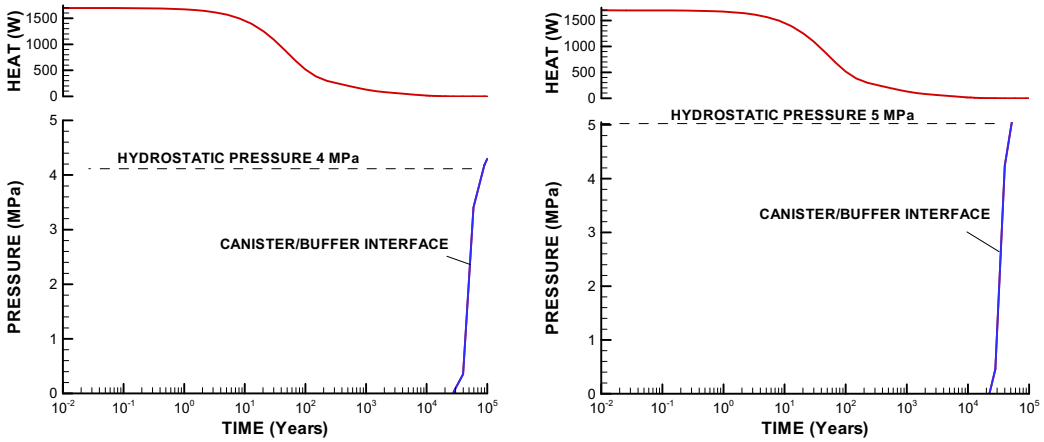

Figure 4.5-4. Evolution of fluid pressure for a repository located at (a) Forsmark and (b) Laxemar for the case of an extremely low rock permeability.

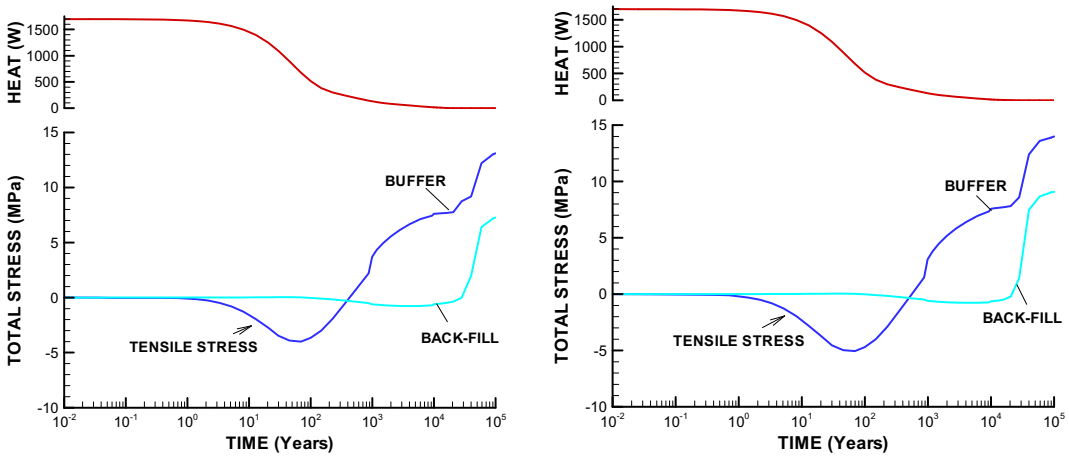

Figure 4.5-5. Evolution of total stress in buffer and backfill for a repository located at (a) Forsmark and (b) Laxemar for the case of an extremely low rock permeability.

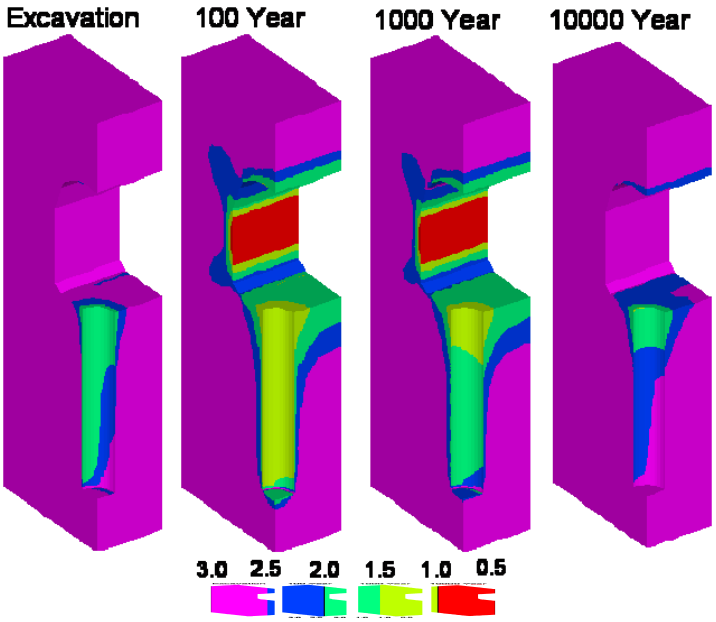

(a) Forsmark

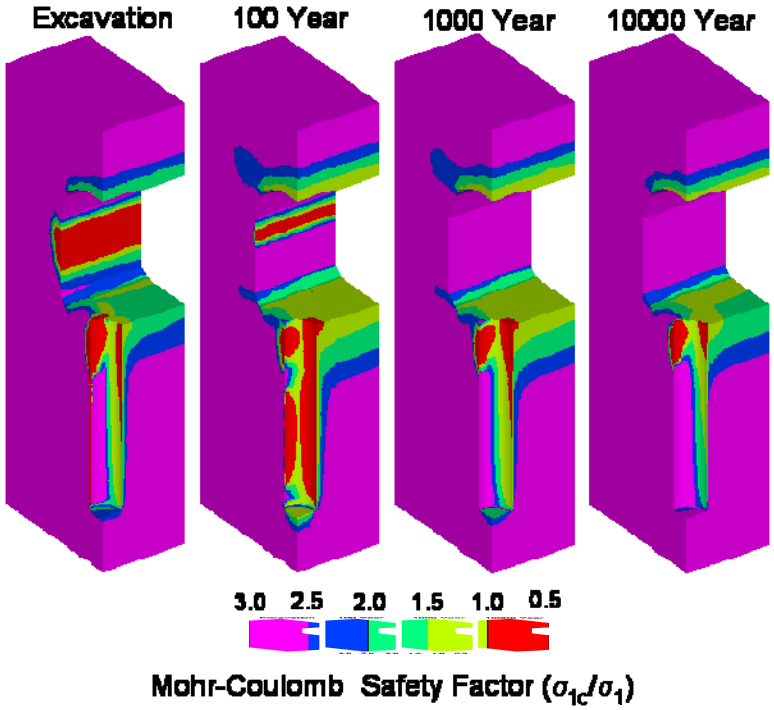

(b) Laxemar

Figure 4.5-6. Evolution of Mohr-Coulomb safety factor (σ_{1c}/σ_1) for a repository located at (a) Forsmark and (b) Laxemar for the case of an extremely low rock permeability. Red contours indicate zones of highest potential for failure as the current maximum principal stress exceeds the critical stress for failure.

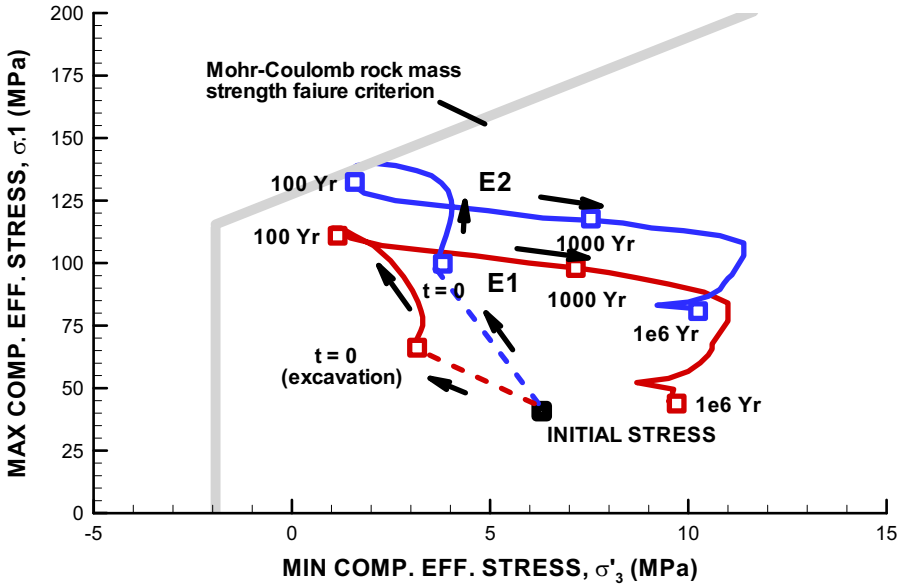

(a) Points E1 and E2

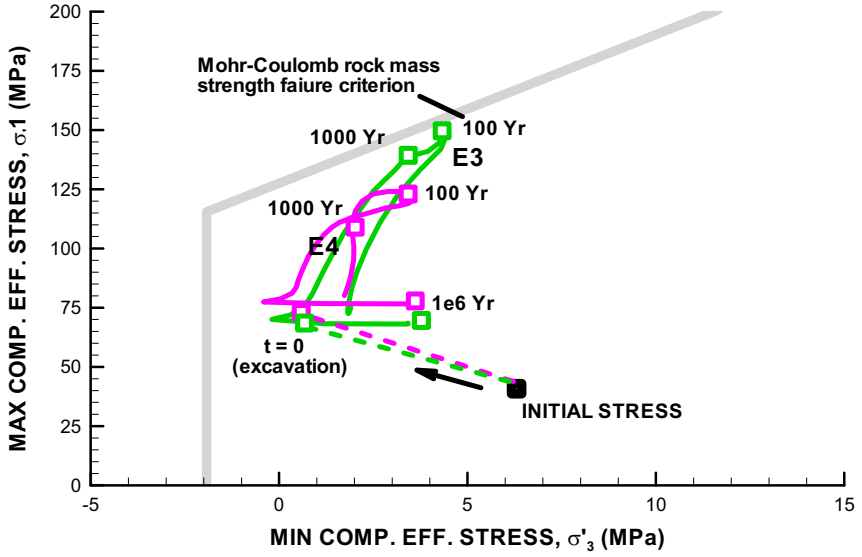

(b) Points E3 and E4

Figure 4.5-7. Principal stress path in relation to Mohr-Coulomb rock-mass failure criterion for a repository located at Forsmark for the case of an extremely low rock permeability (see locations of monitoring points in Figure 4.1-1b).

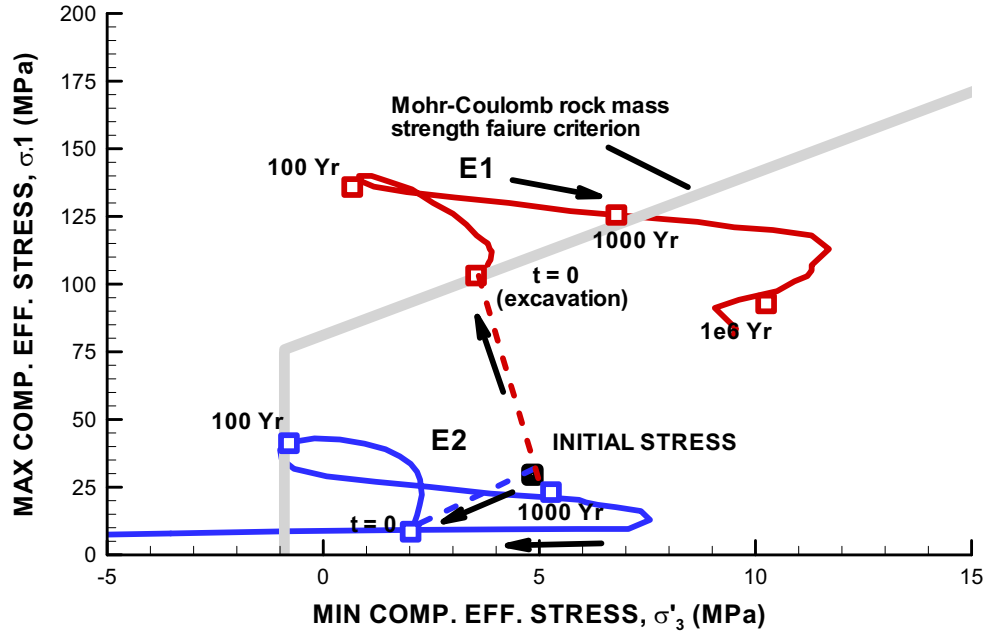

(a) Points E1 and E2

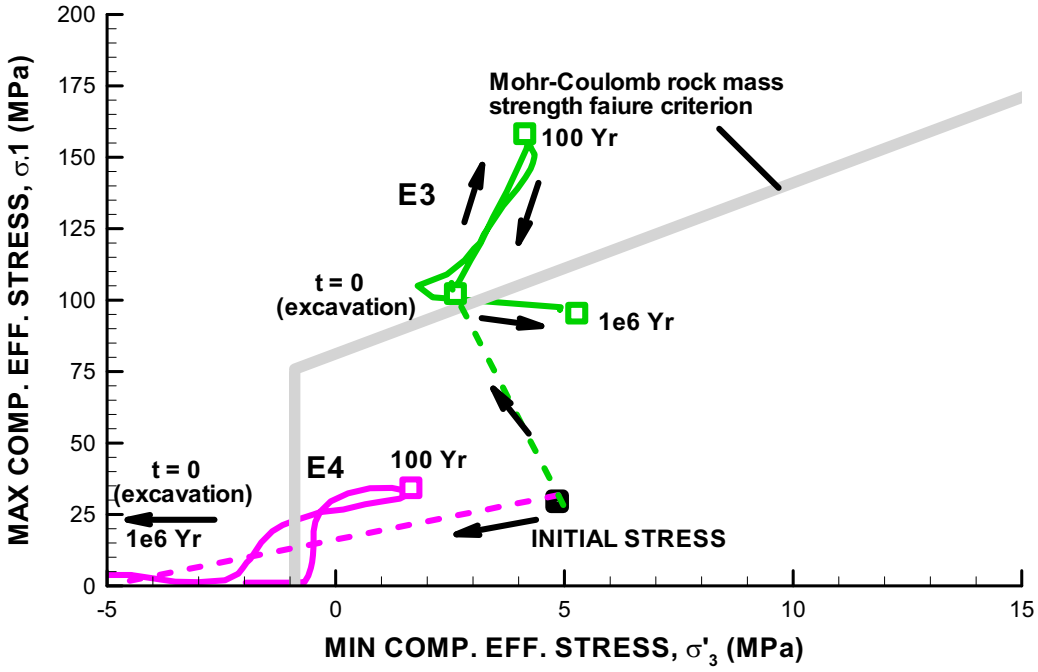

(a) Points E3 and E4

Figure 4.5-8. Principal stress path in relation to Mohr-Coulomb rock-mass failure criterion for a repository located at Laxemar for the case of an extremely low rock permeability (see locations of monitoring points in Figure 4.1-1b).

4.6 Variation of distance to water feeding boundary

In the case of an extremely low permeability rock presented in Section 4.5, there was an obvious disagreement between our analysis and that of SKB's regarding the time to full resaturation. This might be due to the difference in model geometry and distance to the outer hydrological boundary. In SR-Can (SKB 2006a), it is noted that the exact figure of resaturation times depends on where the water-feeding boundary is located (SR-Can, SKB 2006a, Section 9.3.8). The referred calculation had a distance to the water-feeding boundary of only 12 m. Thus, the water pressure is assumed to be constant and equal to the initial hydrostatic pressure at a distance of 12 m from the deposition hole. In this section, we analyze a case very similar to the three-dimensional analysis conducted by Börgesson et al. (2006). That is, we fixed the fluid pressure at a distance of about 25 m above and 20 m below the deposition hole.

Figure 4.6-1 compares the evolution of saturation of the ideal case with that of a case with assumed nearby water-feeding boundaries. In the ideal case, the far-field hydraulic boundaries are located at the ground surface and 1,000 m below. The hydrological behavior in Figure 4.6-1 is quite similar to that obtained for the similar geometry in Börgesson et al. (2006). First of the all, the time to final 100% resaturation is about 550 to 600 years, which is very close to the 570 years obtained by Börgesson et al. (2006). Moreover, the first rapid buffer resaturation to about 95% takes about 20 years in our analysis, which is similar to the 32 years calculated by Börgesson et al. (2006). The result in Figure 4.6-1 shows that there is a very strong dependency on the distance to the outer constant-fluid-pressure boundary in the case of a low-permeability rock. When having a model with nearby constant pressure boundaries, the time to full resaturation decreases from 40,000 to 570 years. This implies that the times to full resaturation claimed in SR-Can can only be valid for the case of a constant-pressure boundary located 12 m from the deposition hole.

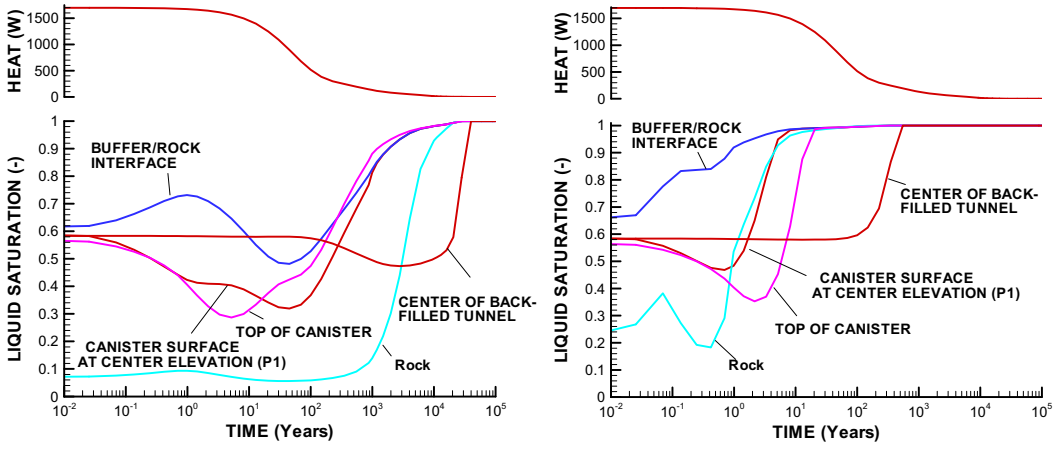

Figure 4.6-1. Evolution of saturation at a repository located at Forsmark for (a) ideal case with hydrological boundaries at ground surface and 1,000 m below, and (b) for constant-fluid-pressure boundaries located 20 m below and 25 m above the deposition hole (see locations of monitoring points in Figure 4.1-1b).

4.7 Effect of rock permeability on resaturation time

In this section, we perform a parameter study, varying the rock permeability to investigate its impact on the resaturation time, to investigate the apparent inconsistency between SKB's analysis and other analyses reported in the literature (as discussed in Section 3.2). Specifically, in SR-Can it is stated that the resaturation of the buffer would be controlled by the hydraulic properties of the buffer if the hydraulic conductivity of the rock is larger than 1×10^{-12} m/s.

Figures 4.7-1 presents resaturation times, defined as time to 99 and 90% liquid saturation, respectively. The figure shows that the resaturation times become constant when rock permeability exceeds 1×10^{-17} m^2, which corresponds to a hydraulic conductivity exceeding 1×10^{-10} m/s. This should be compared with the value 1×10^{-12} m/s obtained by SKB. Thus, our results indicate that a much higher rock hydraulic conductivity is required to make the resaturation process independent of the hydraulic properties of the rock. The lower hydraulic conductivity value obtained by SKB can be explained by the much shorter distance to the constant pressure hydraulic boundaries that may substantially reduce the potential for rock desaturation in their simulations.

Our results indicate that the permeability of the rock should be about a factor 1,000 higher than that of the bentonite buffer for the resaturation process to be independent of the rock permeability. This factor can be explained with the retention and relative permeability curves shown in Figure 3.2-1. As soon as the buffer is emplaced at a saturation of about 60%, the suction pressure in the buffer will desaturate the rock to a saturation of about 0.05 to 0.1. At a rock saturation of 0.05 to 0.1, the relative permeability of the rock is about 10^{-4} to 10^{-3} (Figure 3.2-1). Within the buffer, the relative permeability at about 60% is about 10^{-1}. Thus, the factor 1,000 might be explained by a relative permeability effect. Consequently, the simulation results in this section are only valid for the assumed retention and relative-permeability function of the rock. Likewise, the simulation results by SKB are only valid for their assumed relative-permeability function of the rock.

Comparing the results for 99 and 90% resaturation in Figure 4.7-1, we observe that when the permeability is low, the time to 90% resaturation is at least one order of magnitude shorter. The time to 90% resaturation is probably controlled by the permeability and relative permeability of the backfill, which determines how fast the water can be sucked from the backfill to the buffer. We see that even if the permeability of the rock is extremely low, the buffer will resaturate to 90% within a few thousand years. This should be enough to develop a significant swelling stress in the buffer, but only after several thousand years.

Figure 4.7-2 shows the time to satisfying the safety-function-indicator criteria for swelling stress in the buffer and backfill. The results in Figure 4.7-2 indicate that it is more difficult and takes a longer time to satisfy the criterion for the backfill than for the buffer. For the case of an extremely low rock permeability, the criterion of 1 MPa swelling stress in the buffer is satisfied within 1000 years whereas it may take up to 100,000 years to satisfy the 0.1 MPa criterion in the backfill.

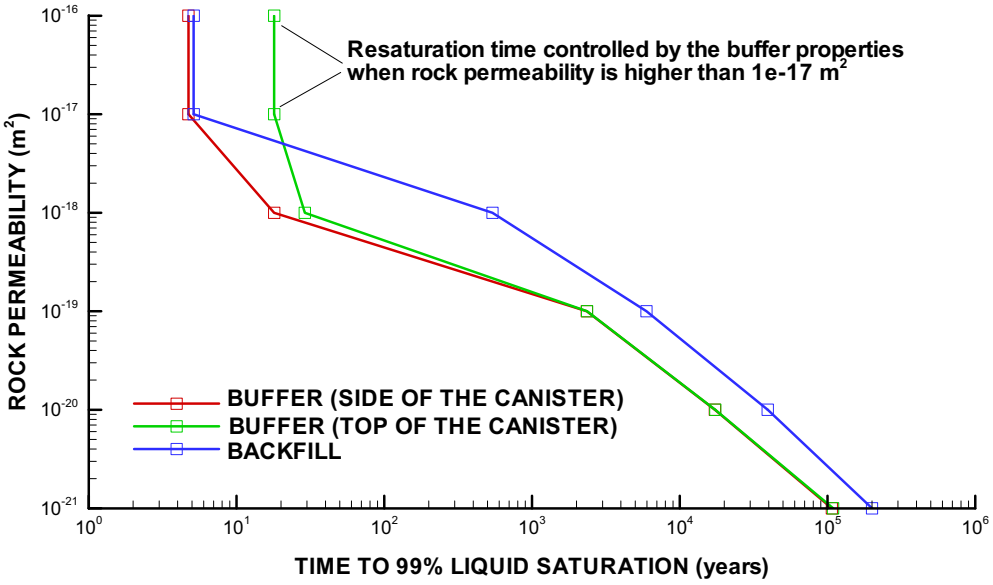

(a) time to 99% liquid saturation

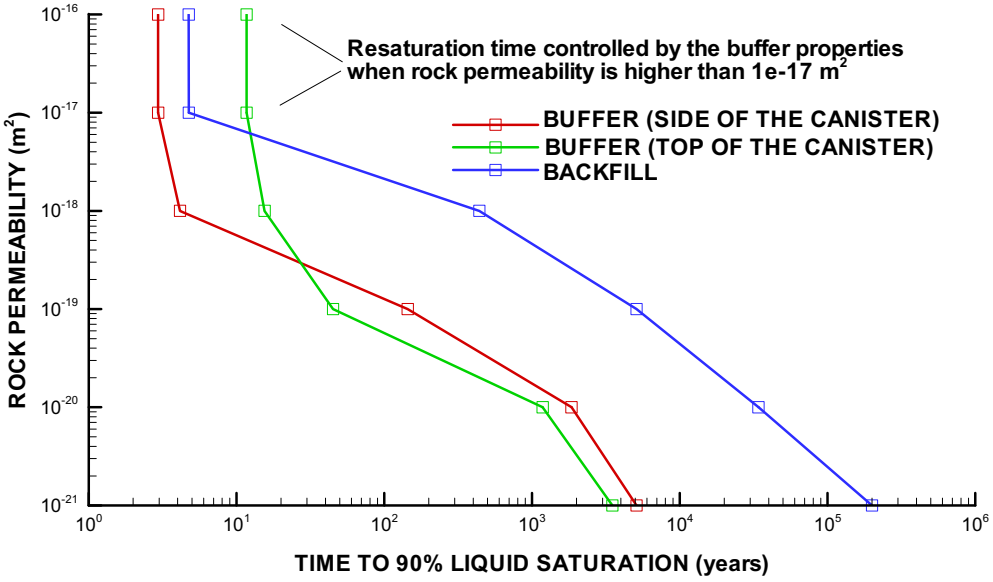

(b) time to 90% liquid saturation

Figure 4.7-1. Resaturation times versus rock permeability expressed as time to (a) 99% liquid saturation and (b) 90% liquid saturation for the Forsmark repository alternative.

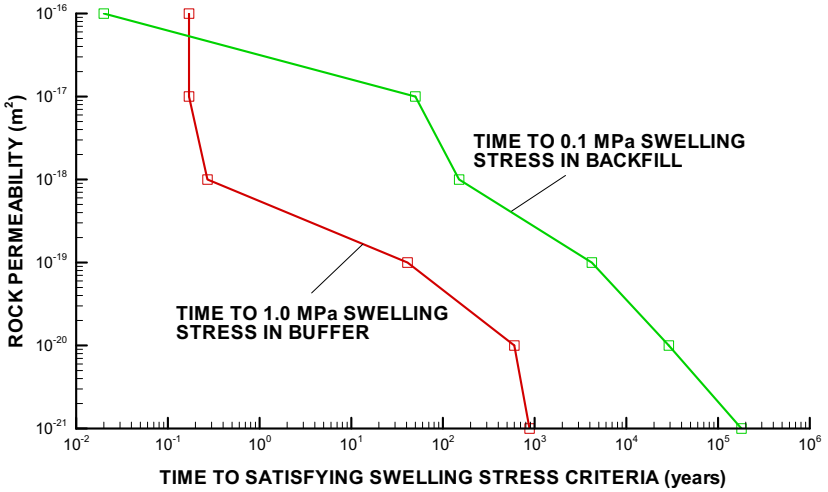

Figure 4.7-1. Time to satisfying swelling stress criteria for buffer and backfill versus rock permeability for the Forsmark repository alternative.

4.8 Variation of retention and relative permeability of the rock

In this section, we investigate the sensitivity of the simulation results to changes in retention curves and relative-permeability functions of the rock. We try to use more conservative values that might give a longer resaturation time than expected. Moreover, we test the different retention properties under two different values of the rock permeability: (1) for the ideal case with intrinsic rock permeability k = 1×10^{-16} m^2, and (2) for the case of an extremely low intrinsic rock permeability k = 1×10^{-20} m^2.

4.8.1 Variation of retention curve of the rock

In this case, we lower the retention curve of the rock by one order of magnitude. This is done by changing the van Genuchten parameter P_0 from 5.5 to 0.55 MPa. Moreover, in our base-case model we had assigned a residual liquid saturation of 0.05. We decrease this value to 0.0. This one-order-of-magnitude change is not very large, considering the possible variations and uncertainties in the retention properties of the rock.

The results in Figure 4.8-1 shows that if the rock permeability is high (k = 1×10^{-16} m^2), a lowering of the rock's retention curve by one order of magnitude causes temporarily desaturation of the rock during the first few years after emplacement, but the time to complete (S_l = 99%) resaturation is not affected. Thus, lowering the retention curve by one order of magnitude has little impact on the performance, as long as the rock permeability is high.

The results in Figure 4.8-2, on the other hand, show that if the rock permeability is low (k = 1×10^{-20} m^2), the lowering of the rock's retention curve causes a delayed resaturation in the backfill, whereas the resaturation of the buffer appears to be unaffected. Figure 4.8-3 shows that the lowering of the retention curve has a pronounced impact on the desaturation of the rock, in particular around the tunnel. The increased desaturation around the backfilled tunnel is explained by the fact that

the lowered retention curve implies that the retention in the rock is lower than in the backfill. Thus, this confirms that the retention curves for the buffer, backfill and rock, and hence the relative retention in these components, are very important for the resaturation process.

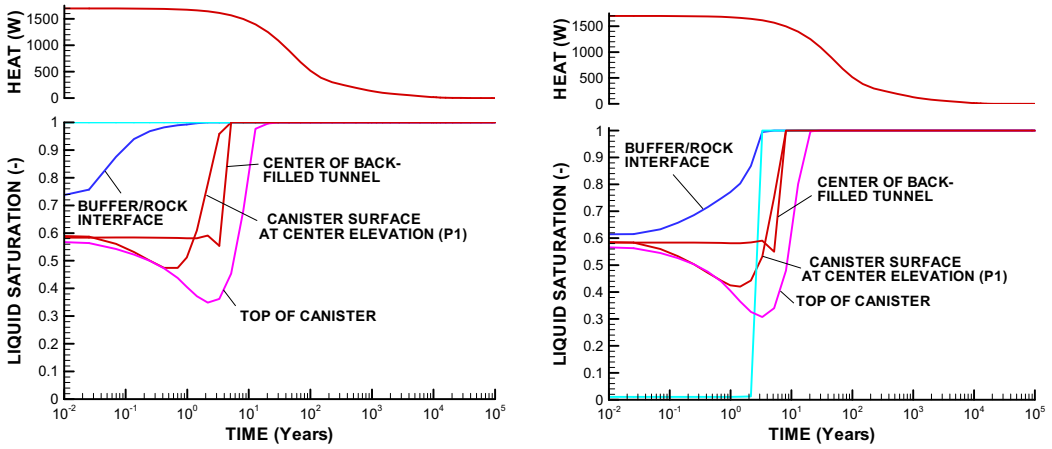

(a) SKB's water retention of rock (b) lower water retention of rock

Figure 4.8-1. Variation of the water-retention curve of the rock when rock permeability is high (k = 1×10^{-16} m^2): Evolution of saturation at a repository located at Forsmark for (a) the ideal case with SKB's assumed retention curve for the rock and (b) for a case with lower retention properties of the rock.

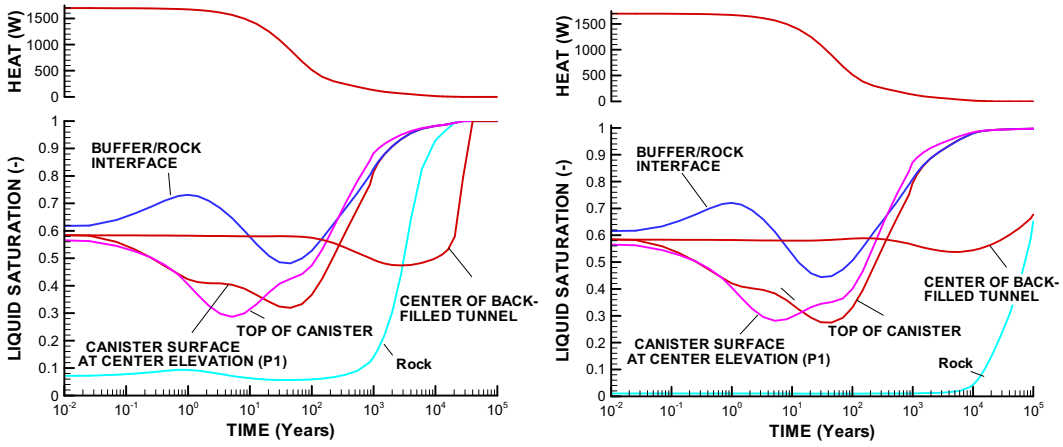

(a) SKB's water retention of rock (b) lower water retention of rock

Figure 4.8-2. Variation of the water-retention curve of the rock when rock permeability is very low (k = 1×10^{-20} m^2): Evolution of saturation at a repository located at Forsmark for (a) a case with SKB's assumed retention curve for the rock, and (b) for a case with lower retention properties of the rock.

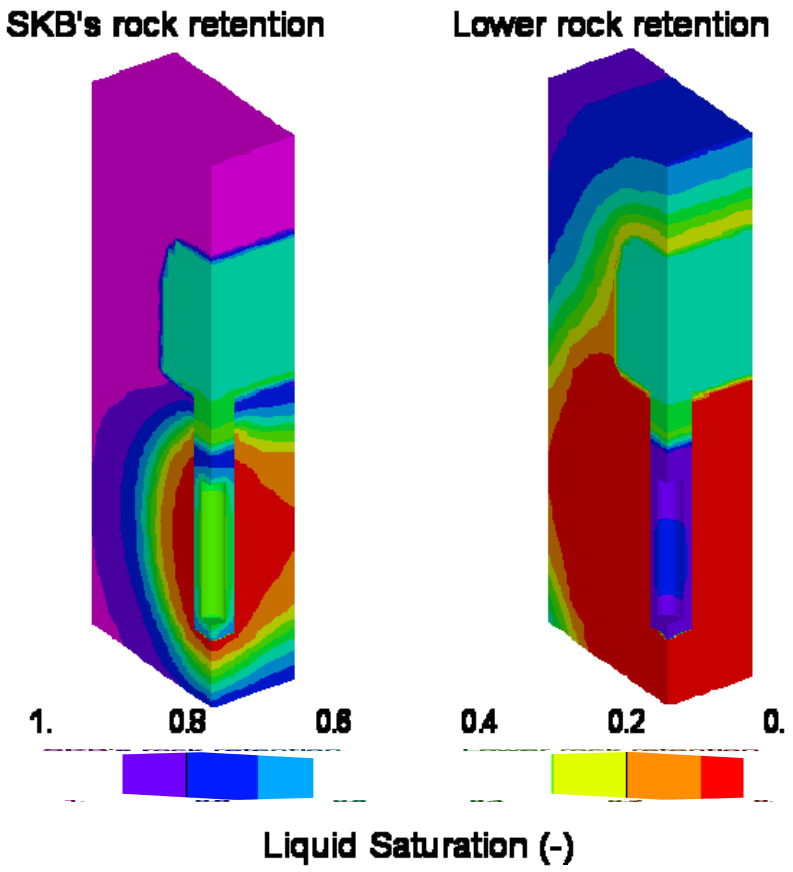

Figure 4.8-3. Variation of the water-retention curve of the rock when rock permeability is very low (k = 1×10^{-20} m^2): Distribution of liquid saturation 100 years after emplacement for a repository located at Forsmark for a case with SKB's assumed retention curve for the rock and a case with lower retention properties of the rock.

4.8.2 Variation of relative permeability of the rock

We change the relative-permeability function from being equal to that of the buffer (i.e., $k_r = S^3$) to being equal to that of the backfill (i.e., $k_r = S^{10}$). This is a much more sensitive function assuming a strong lowering of the relative permeability that might be an extreme case. However, we do not know if this is really an extreme case, since the relative-permeability function of fractured crystalline rock is in general not well known.

The results in Figure 4.8-4 and 4.8-5 show that the lowering of the relative-permeability function for the rock has a small impact on the resaturation processes for both low and high intrinsic rock permeability. Only a small difference can be found in the early time in Figure 4.8-4, when lowering of the rock relative permeability causes a temporal desaturation of the rock that has no impact on the following evolution of saturation in the buffer and backfill.

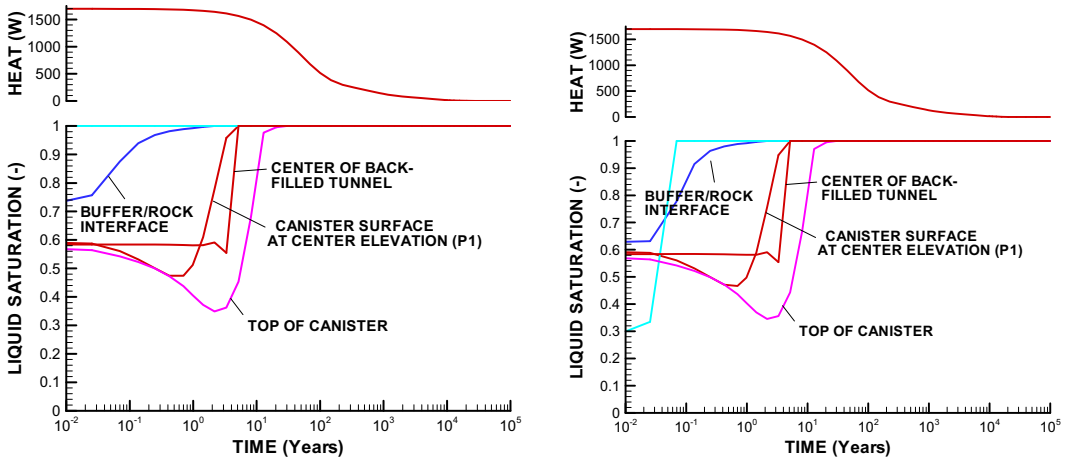

Figure 4.8-4. Variation of the relative permeability of the rock when intrinsic rock permeability is high (k = 1×10^{-16} m^2): Evolution of saturation at a repository located at Forsmark for (a) the ideal case with SKB's assumed relative permeability for the rock and (b) for a case with a lowered relative-permeability function of the rock.

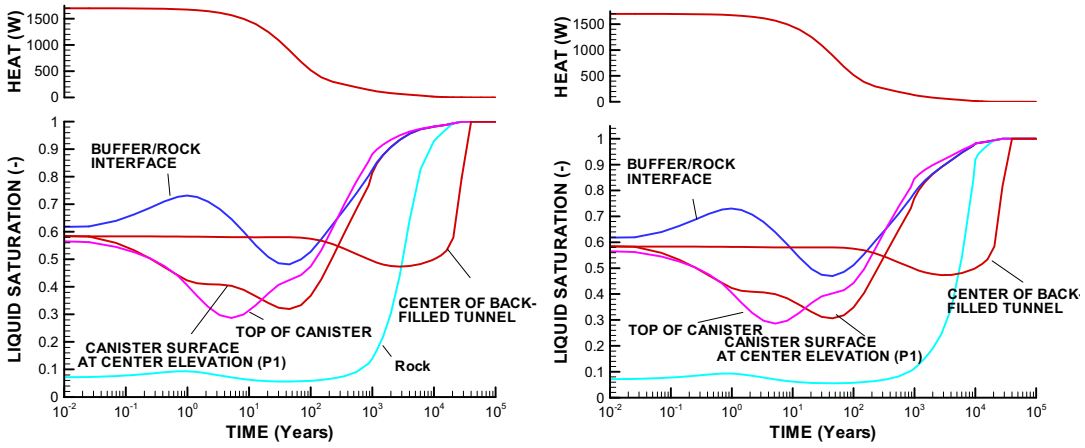

Figure 4.8-5. Variation of the relative permeability of the rock when intrinsic rock permeability is low (k = 1×10^{-20} m^2): Evolution of saturation at a repository located at Forsmark for (a) with SKB's assumed relative permeability for the rock and (b) a case with a lowered relative-permeability function of the rock.

4.9 Case of high (intact) rock-mass modulus

The deformation modulus of the rock mass is an important parameter for the thermally induced stress and important for assessing the potential of thermally induced failure around the underground openings. In the ideal case, we used values of the rock-mass modulus that have been evaluated in the site descriptive models of Forsmark (SKB 2005) and Laxemar (SKB 2006b). These values of rock-mass modulus of deformation were developed based on empirical methods and numerical analyses that accounted for fracture spacing, fracture normal stiffness, etc. The rock-mass modulus, considering the effect of fractures, results in a lower Young's modulus than that of the intact rock. However, the initial stresses at both Forsmark and Laxemar are generally very high at the depth of the candidate repositories, implying that fractures may be compressed to a relatively high stiffness. Moreover, the thermal stress will compress the fractures further. Therefore, it might be reasonable to adopt an upper bound for the rock-mass modulus equal to that of the intact rock. Therefore, in this case, the Young's modulus is increased from 68 GPa to 76 GPa at Forsmark, and from 55 GPa to 70 GPa at Laxemar. All the other parameters are equivalent to that of the ideal case as presented in Section 4.5.

Figures 4.9-1 through 4.9-4 compare the distribution and evolution of maximum principal stress for the current case with a high (intact) rock modulus to that of the ideal case with a reduced rock-mass modulus. Figures 4.9-1 and 4.9-2 show some increase in the size of the zone of red contour near the deposition hole, which indicate that the compressive stress increased in that area. The increased thermally induced compressive stress is also shown in Figures 4.9-3 and 4.9-4. However, the differences in the stress evolution for the two cases are rather small; other factors such as initial stress magnitude and orientation and anisotropy of the stress field might be more important.

Figures 4.9-5 and 4.9-6 also indicate some increase in the extent of the failure zones when assuming the intact rock modulus, but the differences are rather minor. Considering the relatively small differences in the outcome of the failure analysis, it might be recommended to use the intact rock modulus in the coupled THM analysis, as this represents an upper bound that would be a conservative assumption in the performance assessment of the repositories. This would remove the uncertainties associated with estimation of the rock-mass modulus.

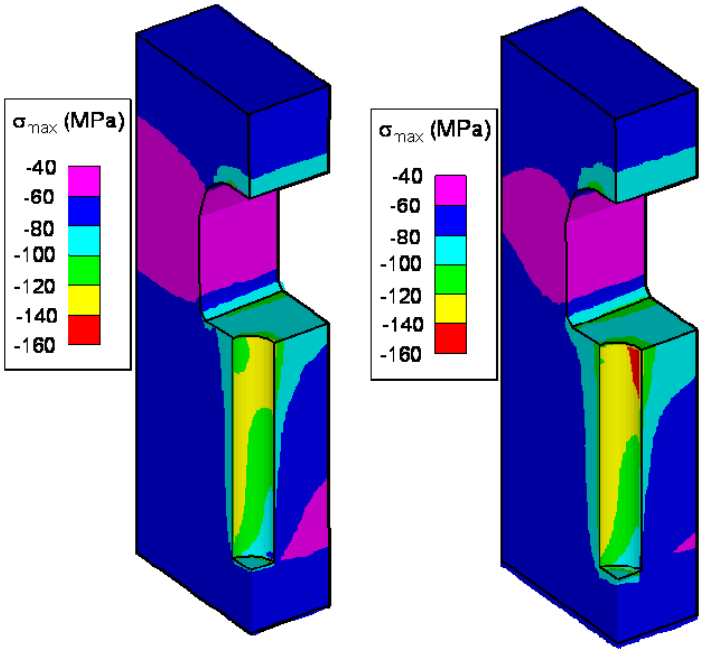

(a) Ideal case (b) High rock modulus

Figure 4.9-1. Maximum (σ_{max}) compressive principal stresses after 1,000 years for a repository located at Forsmark for a different rock-mass modulus.

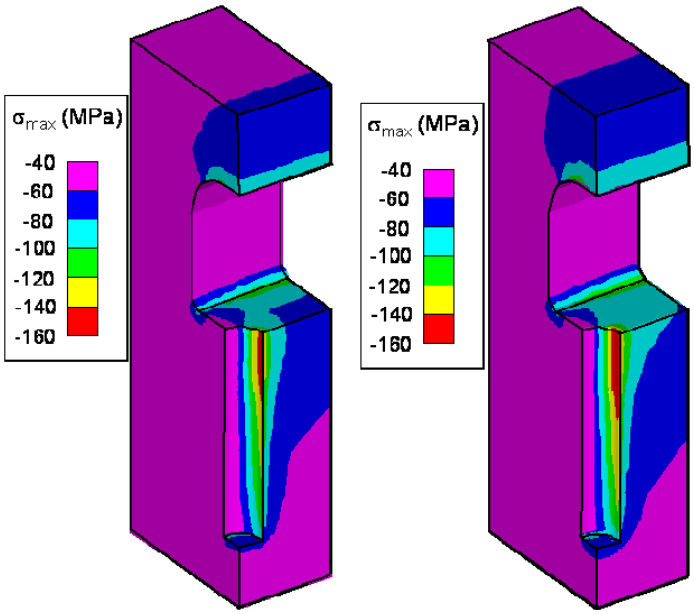

(a) Ideal case (b) High rock modulus

Figure 4.9-2 Maximum (σ_{max}) compressive principal stresses after 1,000 years for a repository located at Laxemar for a different rock-mass modulus.

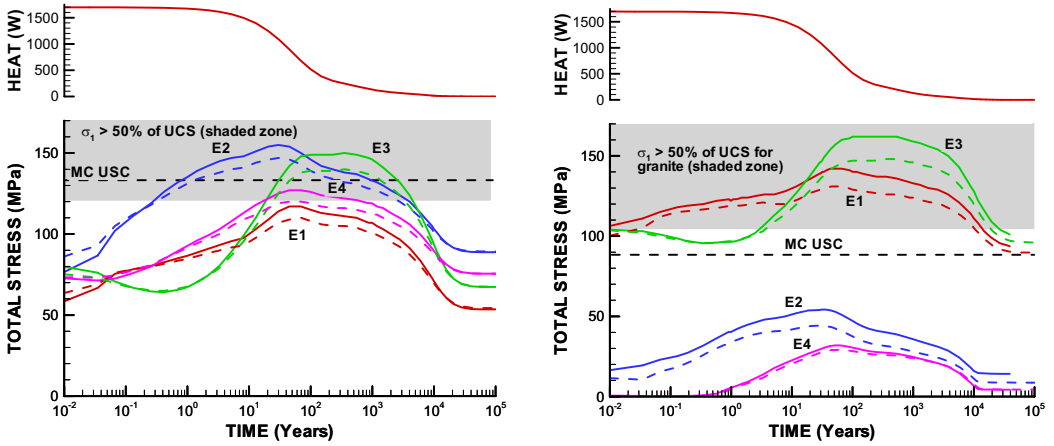

(a) Forsmark (b) Laxemar

Figure 4.9-3. Evolution of maximum compressive principal effective stress at four points located at the periphery of the deposition hole. The results for the high (intact) rock modulus are shown in solid lines whereas the results for the ideal case using a reduced rock-mass modulus are shown in dashed lines (see locations of monitoring points in Figure 4.1-1b).

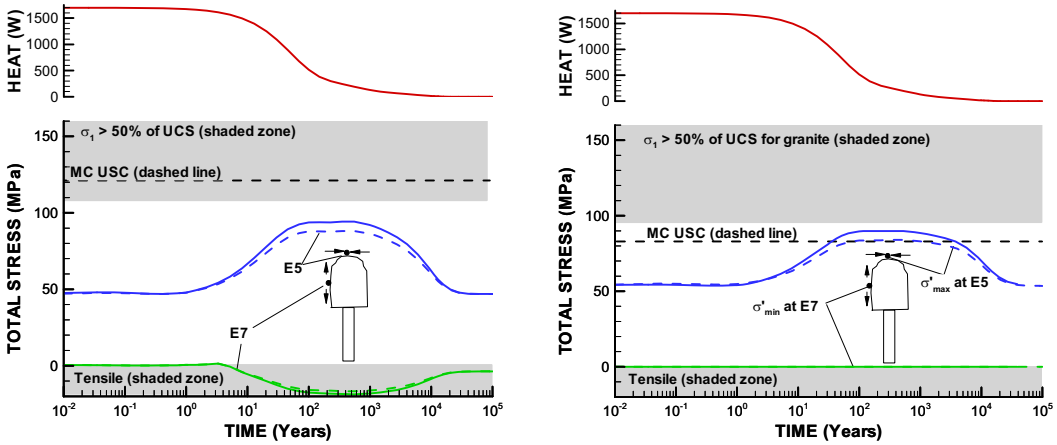

(a) Forsmark (b) Laxemar

Figure 4.9-4. Evolution of principal effective stresses at two points located at the periphery of the emplacement tunnel. The results for the high (intact) rock modulus are shown in solid lines whereas the results for the ideal case using a reduced rock-mass modulus are shown in dashed lines.

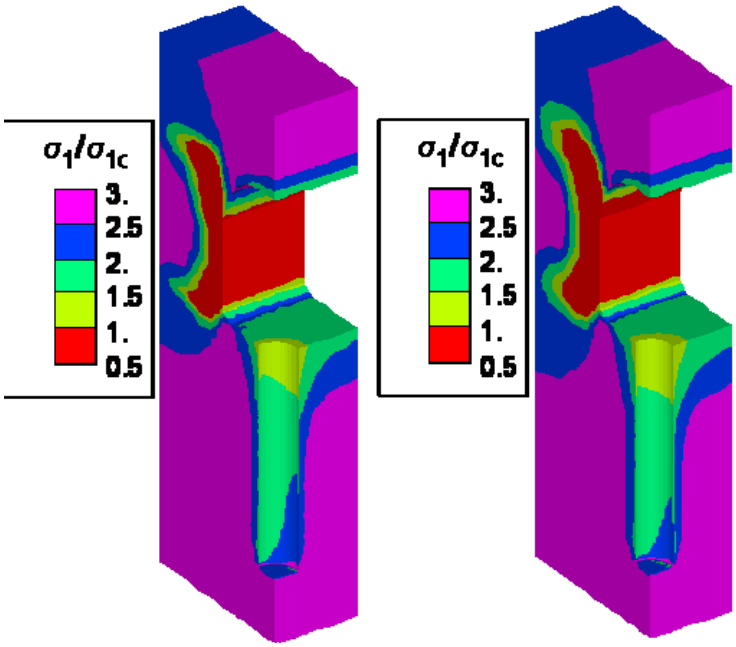

(a) Ideal case (b) High rock modulus

Figure 4.9-5. Evolution of Mohr-Coulomb safety factor (σ_{1c}/σ_1) after 1000 years for a repository located at Forsmark and for two different values of the rock-mass modulus.

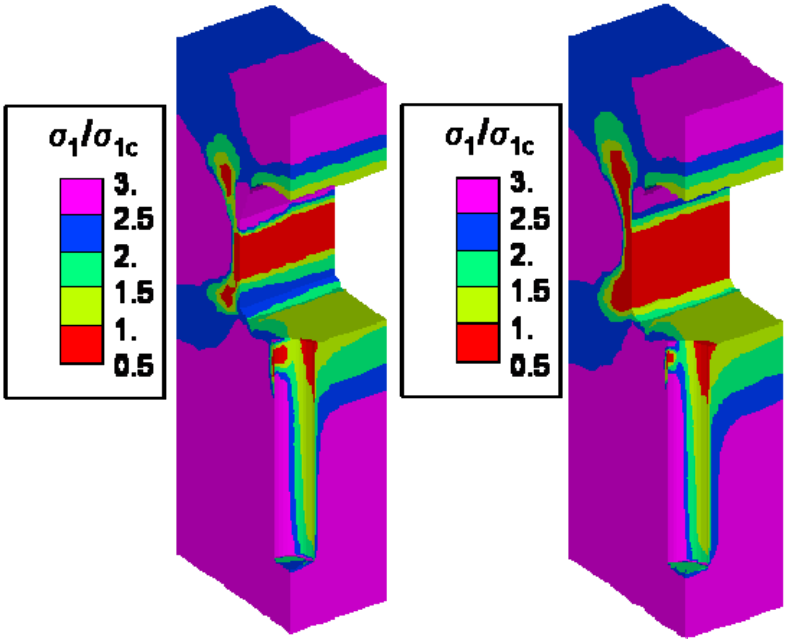

(a) ideal case (b) High rock modulus

Figure 4.9-5. Evolution of Mohr-Coulomb safety factor (σ_{1c}/σ_1) after 1,000 years for a repository located at Laxemar and for two different values of the rock-mass modulus.

4.10 Variation of thermal diffusion coefficient

In this section, we conduct a simulation using an upper bound for the thermal diffusion coefficient, D_{TV}. The upper bound of the thermal diffusion coefficient was determined by model calibration against SKB's thermal gradient experiments in Appendix B of this report. The D_{TV} is increased by approximately a factor of 2 compared to the D_{TV} used in the ideal case. In our model calibration, we found that this higher value captured the drying part of the experiment better. Thus, the higher D_{TV} used in this section might capture the degree of drying of the bentonite more accurately. However, this is still very, uncertain, since the laboratory experiments for determining this parameter were conducted at different conditions (e.g., different void ratio, initial saturation and initial suction) from the *in situ* conditions at emplacement. Therefore, we cannot know which value of D_{TV} is really the most accurate, but we can investigate what impact it would have if the value used by SKB is underestimating the real *in situ* thermal diffusion coefficient.

The results in Figures 4.10-1 and 4.10-2 with the upper bound estimate of the thermal diffusion coefficient can be compared to that of the ideal base case shown in Figure 4.4-1 and 4.4-2. The results show that with the upper-bound estimate of thermal diffusion coefficient, the initial drying of the buffer is stronger, leading to a dryer buffer in the first few years and a slightly higher peak temperature. The higher peak temperature has a first peak at 1 to 2 years of heating and a second peak equivalent to the peak temperature achieved in the ideal case (compare Figures 4.10-1 and 4.4-1). Moreover, the upper- bound estimate of the thermal diffusion coefficient leads to a slightly delayed resaturation, with time to full resaturation of the buffer increasing from about 15 to 30 years.

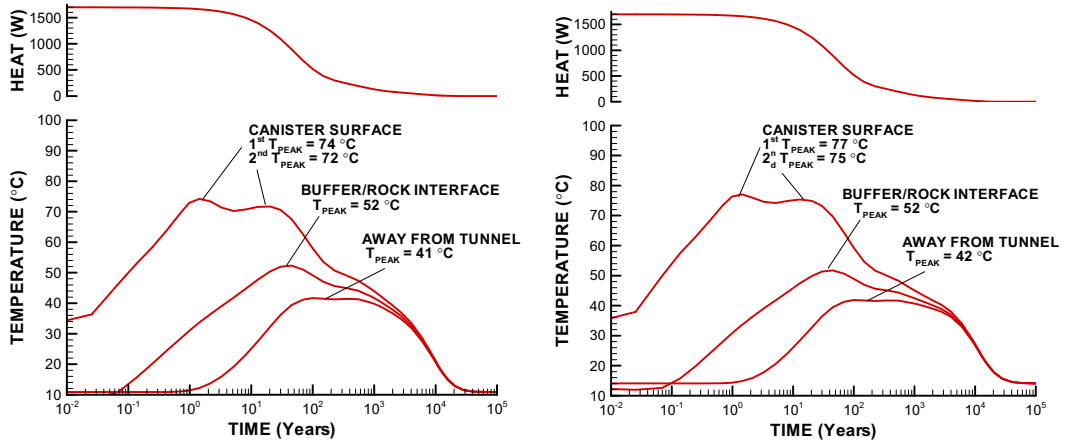

Figure 4.10-1. Evolution of power and temperature for a repository located at (a) Forsmark and (b) Laxemar for an upper bound estimate of the thermal diffusion coefficient.

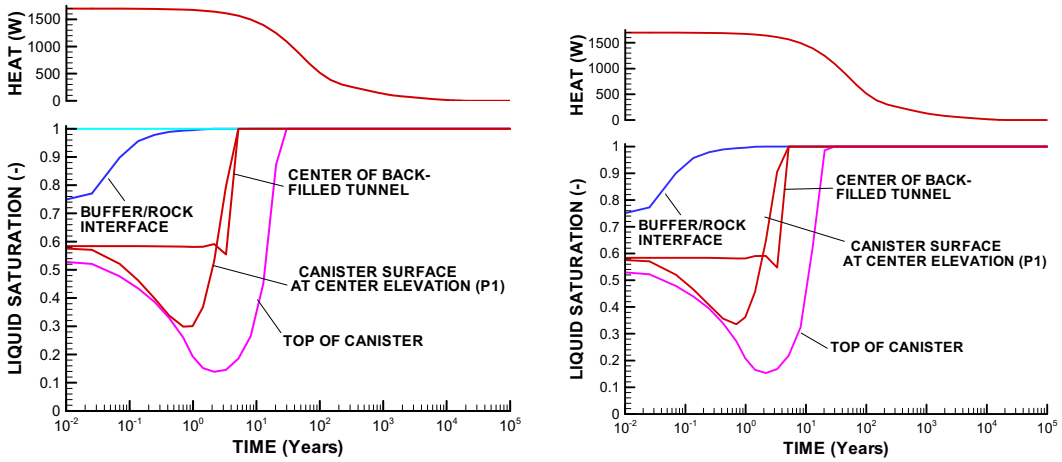

Figure 4.10-2. Evolution of saturation for a repository located at (a) Forsmark and (b) Laxemar for an upper bound estimate of the thermal diffusion coefficient.

4.11 Peak temperature for an extreme case of dry rock and high vapor diffusion coefficient

In this section, we investigate a potential condition of extreme drying of the buffer that could lead to a reduced thermal conductivity in the buffer, and thereby an unexpectedly high peak temperature. In Section 4.10, we found that the degree of drying in the buffer during the heating phase is strongly dependent on the thermal vapor diffusion coefficient. The increased drying caused by the upper bound of the thermal vapor diffusion coefficient also affected the peak temperature. In Section 4.5, we also found that an extremely low permeability rock leads to enhanced drying of the buffer and consequently a higher peak temperature. An extreme case would then be the combined effect of an upper-bound thermal diffusion coefficient and low-permeable rock that could lead to an even higher peak temperature.

Figure 4.11-1 and 4.11-2 show the results of temperature evolution and liquid saturation for this extreme case. Figure 4.11-1 shows that maximum temperatures of 94°C (for Forsmark) and 99°C (for Laxemar) are attained at the canister surface at about 10 to 20 years after waste emplacement. Thus, compared to the ideal case presented in Section 4.4, the peak temperature has increased by 21°C (from 72 to 94°C) for Forsmark and by 26°C (from 75 to 91°C) for Laxemar. The increased peak temperature is caused by the extreme drying of the buffer, with a minimum saturation as low as 20% next to the canister. At 20%, the thermal conductivity of the buffer is 0.3 w/mK, as defined by a lower-bound value for dried bentonite (Börgesson and Hernelind, 1999).

These simulation results indicate that a peak temperature very close to 100°C could be achieved in an extreme situation. In addition, we note that the experimental data for thermal conductivity in the buffer is limited to saturations values over 42%, whereas SKB's model is a linear extrapolation to characterize thermal conductivity at saturation values below 42%. Thus, there might be some additional uncertainties regarding the thermal conductivity of low saturation and the lower bound value of 0.3 W/mK. A small difference (e.g., 0.25 W/mK) would result in an even higher peak

temperature in this case. Moreover, we did not consider a gap between the rock and buffer. Calculations made by SKB indicate that such a gap could increase the peak temperature by about 4°C (SR-Can, SKB 2006a, Section 9.3.4).

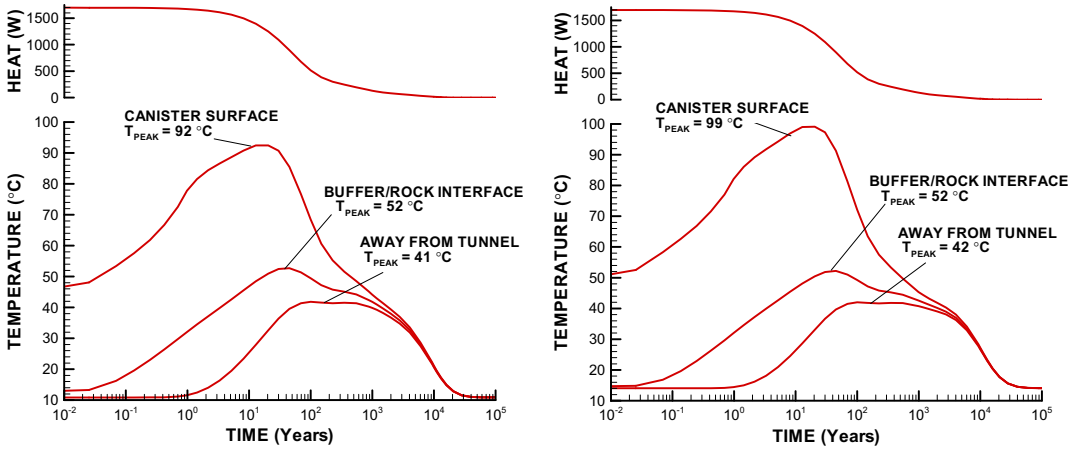

(a) Forsmark (b) Laxemar

Figure 4.11-1. Evolution of power and temperature for a repository located at (a) Forsmark and (b) Laxemar for an extremely case of low rock permeability and high thermal diffusion coefficient.

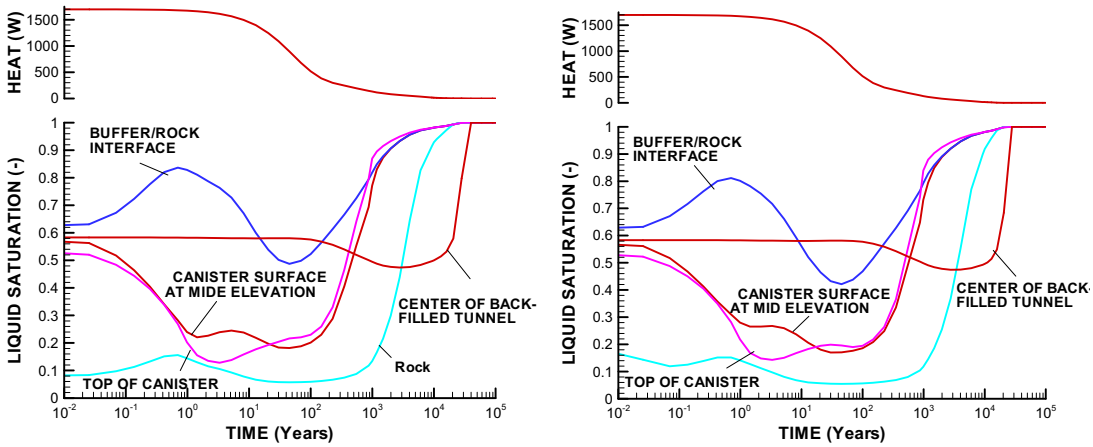

(a) Forsmark (b) Laxemar

Figure 4.11-2. Evolution of saturation for a repository located at (a) Forsmark and (b) Laxemar for an extreme case of low rock permeability and high thermal diffusion coefficient.

4.12 Case of optimum tunnel orientation relative to stress field at Laxemar

In this section, we investigate whether the potential for rock failure near the deposition hole and tunnel could be reduced by using an optimum tunnel orientation relative to the anisotropic *in situ* stress field. Thus, in this simulation, we rotate the tunnel 90° so that the minimum horizontal stress will be oriented perpendicular to the axis of the tunnel, and hence the maximum horizontal stress will be oriented along the axis of the tunnel.

The results shown in Figures 4.12-1 and 4.12-2 can be directly compared with the corresponding results for the ideal base case shown in Figures 4.4-9b and 4.4-13. Clearly, the potential for rock failure is much reduced when the tunnels have an optimum orientation relative to the stress field. In Figure 4.12-1 a small zone of failure can be observed at the deposition hole near the tunnel floor. At 100 and 1,000 years there is also a quite high potential for compressive failure along the deposition hole, but it is still slightly below the critical stress required for failure according to the Mohr-Coulomb criterion. When comparing Figure 4.12-1 and Figure 4.4-9b we also see a dramatic improvement in the tunnel wall, where the zone of tensile failure has been eliminated by reorienting the tunnels.

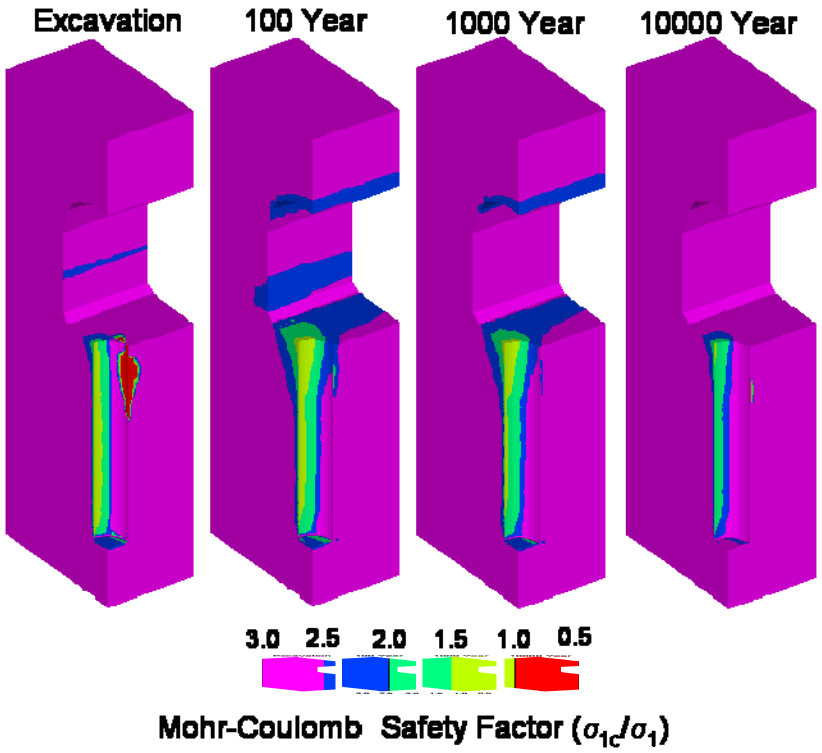

Figure 4.12-1. Evolution of Mohr-Coulomb safety factor (σ_{1c}/σ_1) for a repository located at Laxemar for the case of optimum orientation of tunnels relative to the *in situ* stress field. Red contour indicates zone of highest potential for failure as the current maximum principal stress exceeds the critical stress for failure.

Overall the results in this section show that the ideal case in Section 4.4 is not an ideal case for minimizing the potential for failure around the tunnels at the Laxemar site. Clearly, reorienting the tunnels would be very beneficial, because this would substantially reduce the risk of rock failure near the deposition hole and the tunnels.

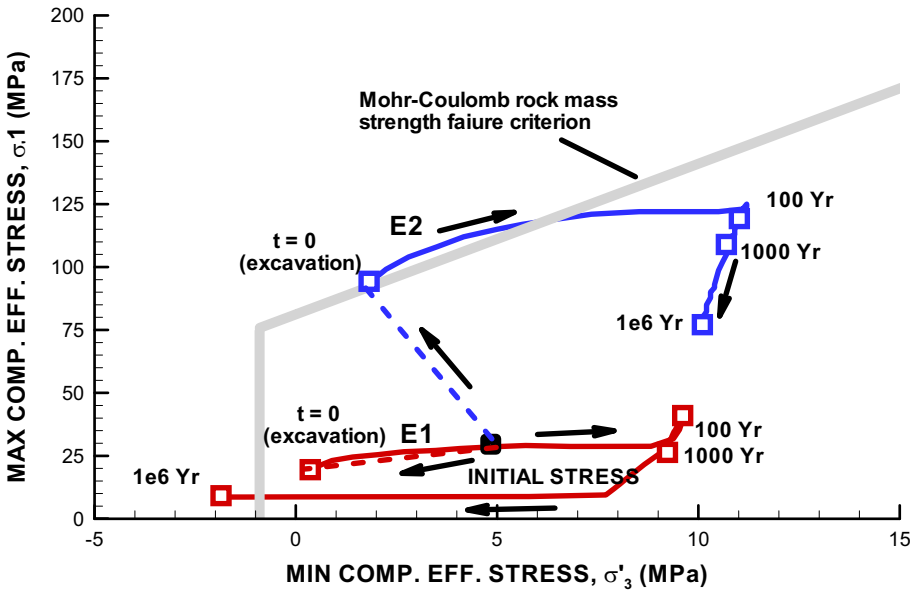

(a) Points E1 and E2

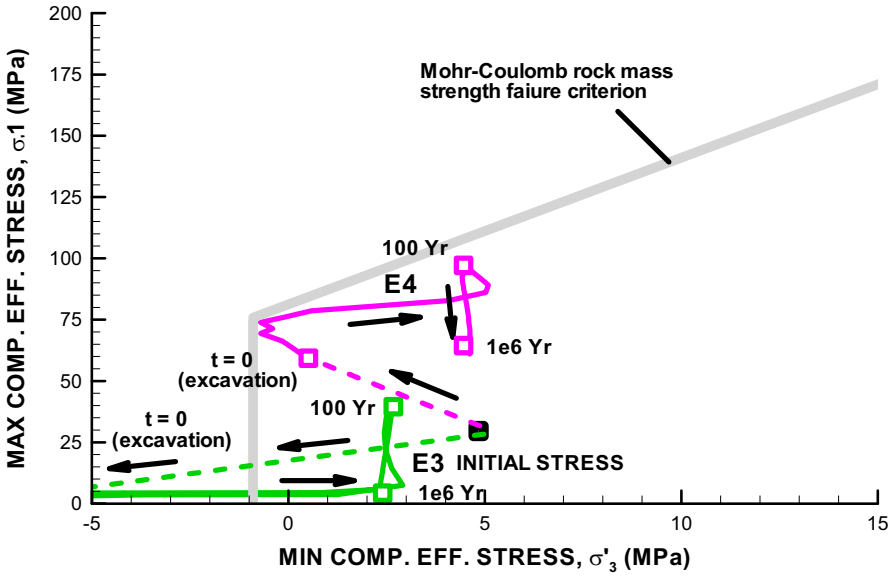

(b) Points E3 and E4

Figure 4.12-2. Principal stress path in relation to Mohr-Coulomb rock-mass failure criterion for a repository located at Laxemar for the case of optimum orientation of tunnels relative to the *in situ* stress field (see locations of monitoring points in Figure 4.1-1b).

4.13 Extreme case of near isotropic horizontal stress at Forsmark

There is a large spread in the measured magnitudes of the *in situ* stress field at Forsmark. In the ideal base case of this study, we used the average stress as derived from measurement between 350 to 600 m depth (Forsmark site descriptive model, SKB 2005, Table 6-10). At 400 m depth, the average principal horizontal stresses are $\sigma_H = 35 + 0.020z = 43$ MPa and $\sigma_h = 19 + 0.025z = 29$ MPa. The Forsmark site descriptive model, SKB (2006b), Table 6-10, presents ranges for the estimated stresses as ±20 for the minimum compressive principal stress and ±10 for the maximum compressive stress. Based on these range intervals, an extreme case of near-isotropic stress is derived by factoring the σ_H and σ_h by 0.9 and 1.2 respectively. That is, at 400 m, the stress field would be $\sigma_v = 0.0260z = 10.4$ MPa, $\sigma_H = (35 + 0.020z)*0.9 = 38.7$ MPa and $\sigma_h = (19 + 0.025z)*1.2 = 34.8$ MPa. This variation in the stress field will impact the potential for failure and spalling around the tunnel and deposition holes, as the stress normal to the tunnel axis is increased compared to the ideal base case.

The results shown in Figures 4.13-1 and 2 can be compared with the corresponding results for the ideal base case shown in Figures 4.4-9a and 4.4-12. The results in Figure 4.13-1 show that the potential for spalling is now higher at the deposition hole near the floor of the tunnel. This is also seen in Figure 4.13-2b, in which the stress path at point E4 exceeds the Mohr-Coulomb criterion after about 100 years. Also, the results in Figure 4.13-1 show that the zone of tensile failure in the tunnel wall is more extensive. This is expected, because the stress perpendicular to the tunnels was increased while the vertical stress remained the same as in the ideal case.

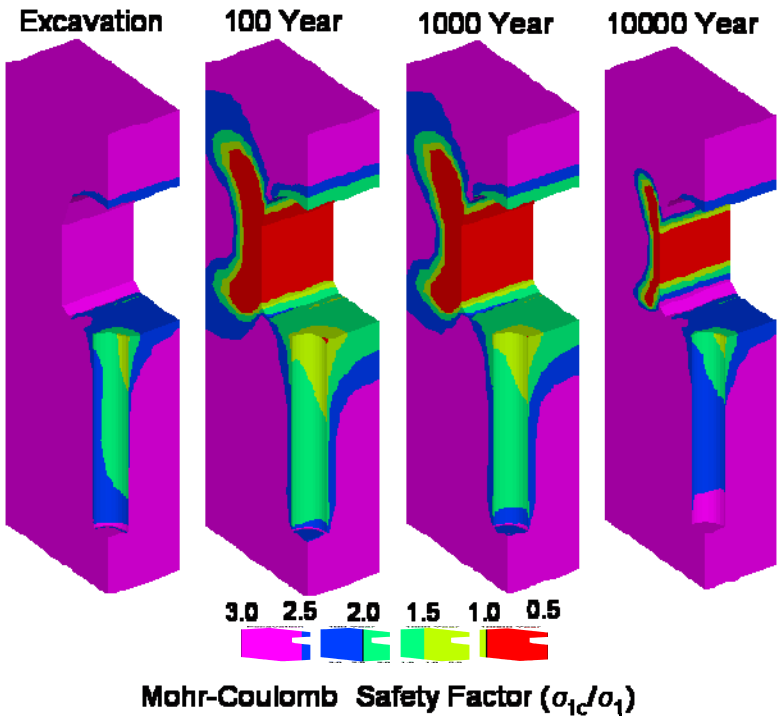

Figure 4.13-1. Evolution of Mohr-Coulomb safety factor (σ_{1c}/σ_1) for a repository located at Forsmark for the extreme case of near isotropic horizontal stress. Red contour indicates zone of highest potential for failure when the current maximum principal stress exceeds the critical stress for failure.

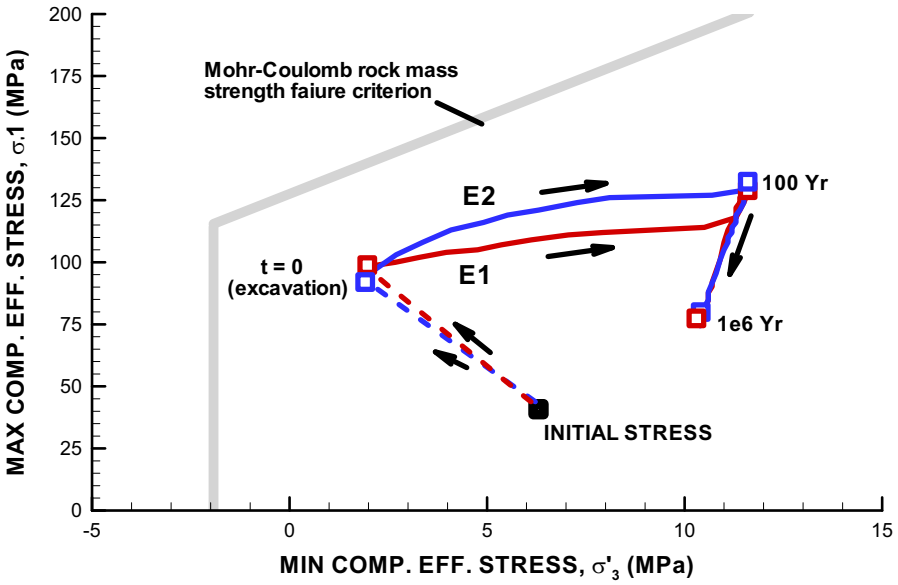

(a) Points E1 and E2

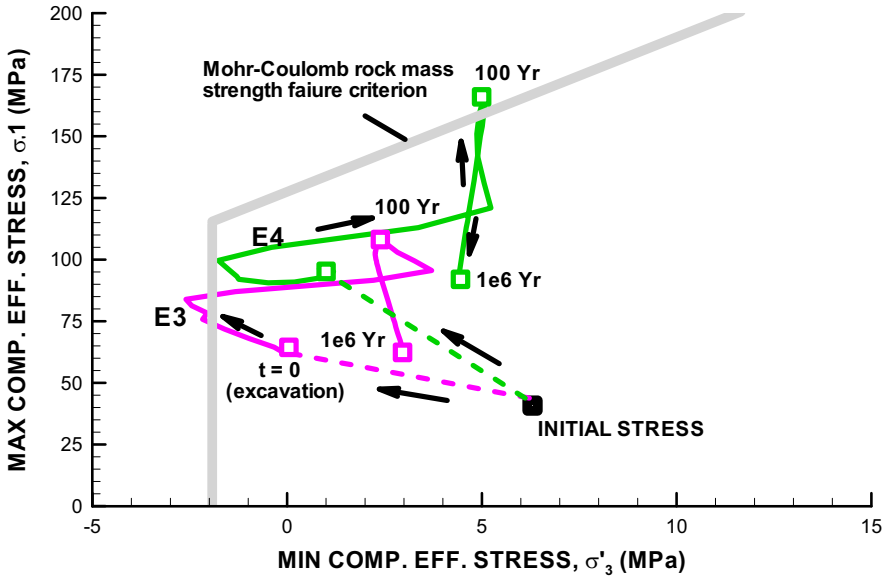

(b) Points E3 and E4

Figure 4.13-2. Principal stress path in relation to Mohr-Coulomb rock-mass failure criterion for a repository located at Forsmark, for the extreme case of near isotropic horizontal stress (see locations of monitoring points in Figure 4.1-1b).

4.14 Extreme case of very anisotropic horizontal stress at Forsmark

In this section, we investigate the failure potential for another extreme of the stress field, namely an extremely anisotropic horizontal stress field. Based on range intervals for the *in situ* stresses given in the Forsmark site descriptive model (SKB 2005), an extreme case of very anisotropic stress is derived by factoring the σ_H and σ_h by 1.1 and 0.8 respectively. That is, at 400 m, the stress field would be $\sigma_v = 0.0260z =$ 10.4 MPa, $\sigma_H = (35 + 0.020z)*1.1 = 47.3$ MPa and $\sigma_h = (19 + 0.025z)*0.8 = 15.22$ MPa.

The results in Figures 4.14-1 and 4.14-2 can be compared with that of the ideal case in Figures 4.4-9a and 4.4-12, as well as with the results of the other extreme case of isotropic horizontal stress presented in Section 4.13. The main difference is that in this case, the highest potential for spalling occurs at a different location around the deposition hole. Moreover, the likelihood for spalling is lower and the extent of the tensile failure zone in the tunnel wall is smaller. This is a result of the lower stress perpendicular to the tunnel axis in this case.

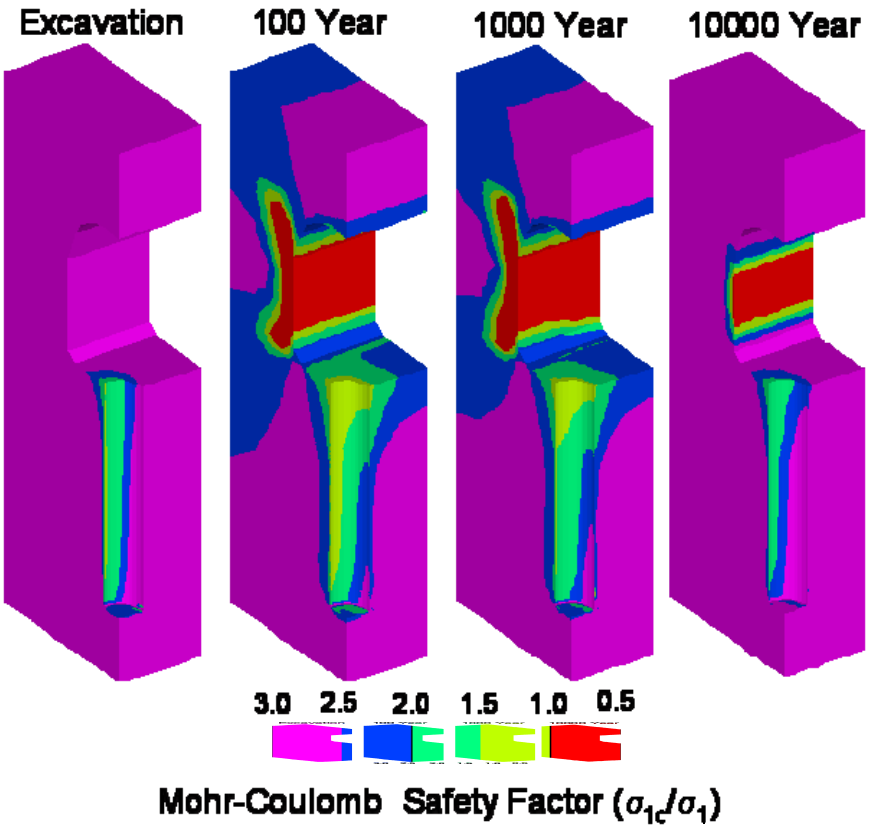

Figure 4.14-1. Evolution of Mohr-Coulomb safety factor (σ_{1c}/σ_1) for a repository located at Forsmark for the extreme case of very anisotropic horizontal stress. Red contour indicates zone of highest potential for failure, as the current maximum principal stress exceeds the critical stress for failure.

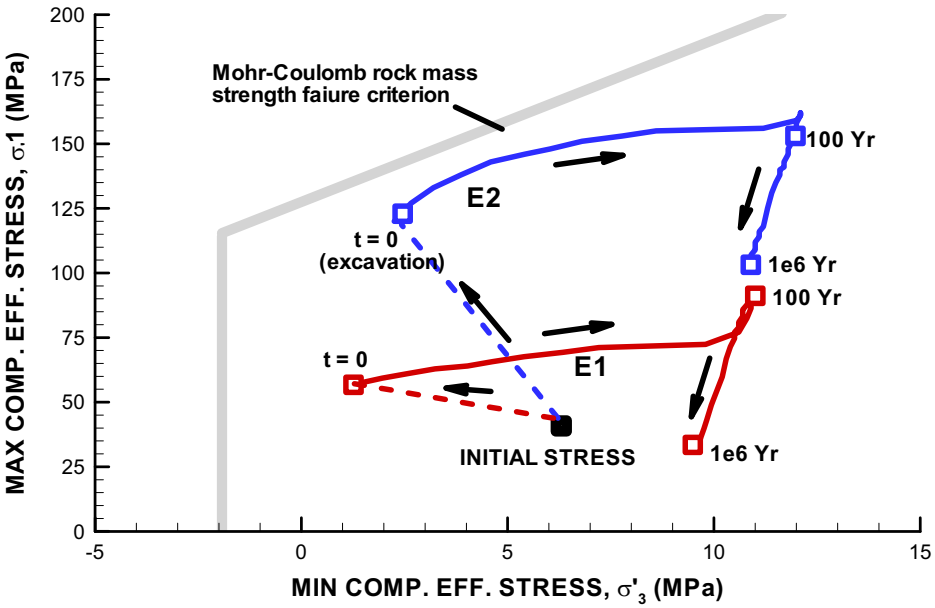

(a) Points E1 and E2

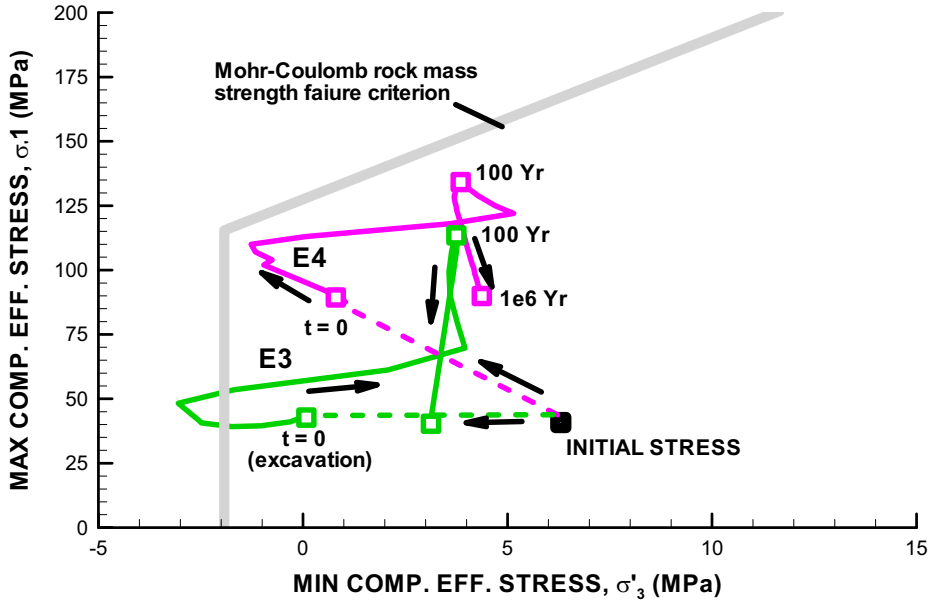

(a) Points E3 and E4

Figure 4.14-2. Principal stress path in relation to Mohr-Coulomb rock-mass failure criterion for a repository located at Forsmark for the extreme case of very anisotropic horizontal stress (see locations of monitoring points in Figure 4.1-1b).

4.15 Impact of backfill properties—30/70 vs Friedland Clay

In this section, we investigate the impact of the choice of backfill material. The main difference in the backfill properties between 30/70-mixture and Friedland Clay are summarized in Figure 4.15-1. First of all, the initial saturation of Friedland Clay is lower, about 30% compared to 58% for the 30/70 mixture (Börgesson et al., 2006, p 42 and 43). At an initial saturation of 30% in Friedland Clay, the suction pressure is slightly higher than in bentonite buffer and much higher than in the rock (Figure 3.2-1). The high suction pressure in the Friedland Clay implies that there is a strong potential for desaturation of the rock and even a possibility for suction of water from the buffer into the overlying backfill. Moreover, at emplacement, the permeability of the backfill for water flow is $k_w = k \cdot S^3 = 0.7 \times 10^{-18} \cdot 0.3^3 = 1.9 \times 10^{-20}$ m^2 for Friedland Clay and $k_w = k \cdot S^{10} = 0.5 \times 10^{-17} \cdot 0.58^{10} = 2.2 \times 10^{-20}$ m^2 for 30/70 mixture. That is, although the intrinsic permeability is lower in Friedland Clay, a very sensitive relative permeability curve for the 30/70 implies that the permeability for water flow at initial saturation is roughly the same in both backfill alternatives.

The results in Figure 4.15-2 and 3 show that the choice of backfill material between 30/70 and Friedland Clay have a relatively minor impact on the time to complete resaturation of the buffer and backfill. The biggest effect is on the resaturation of the backfill itself. In the case of Friedland Clay, the time to full resaturation increases from about 5 to 10 years when rock permeability is high (Figure 4.15-2), whereas the resaturation time decreases from about 40,000 to 20,000 years when rock permeability is low. Moreover, in the case of Friedland Clay, there is very limited water supply from the backfill to the buffer, because in that case the initial suction is higher in the backfill than in the bentonite buffer. Because of higher suction in the backfill, water would tend to be sucked from the buffer into the backfill rather than the reverse. This also implies that if the rock were completely impermeable and if Friedland Clay were be used for backfill, the bentonite would never be resaturated by water supply from the backfill. Rather, the buffer would be slightly dried as a results of suction of water from the buffer to the backfill.

Figure 4.15-4 shows that desaturation of rock is stronger around the tunnel if Friedland Clay is used as backfill. Again, this is because the initial suction in the backfill is very high when using Friedland Clay as backfill and an initial saturation of 30%.

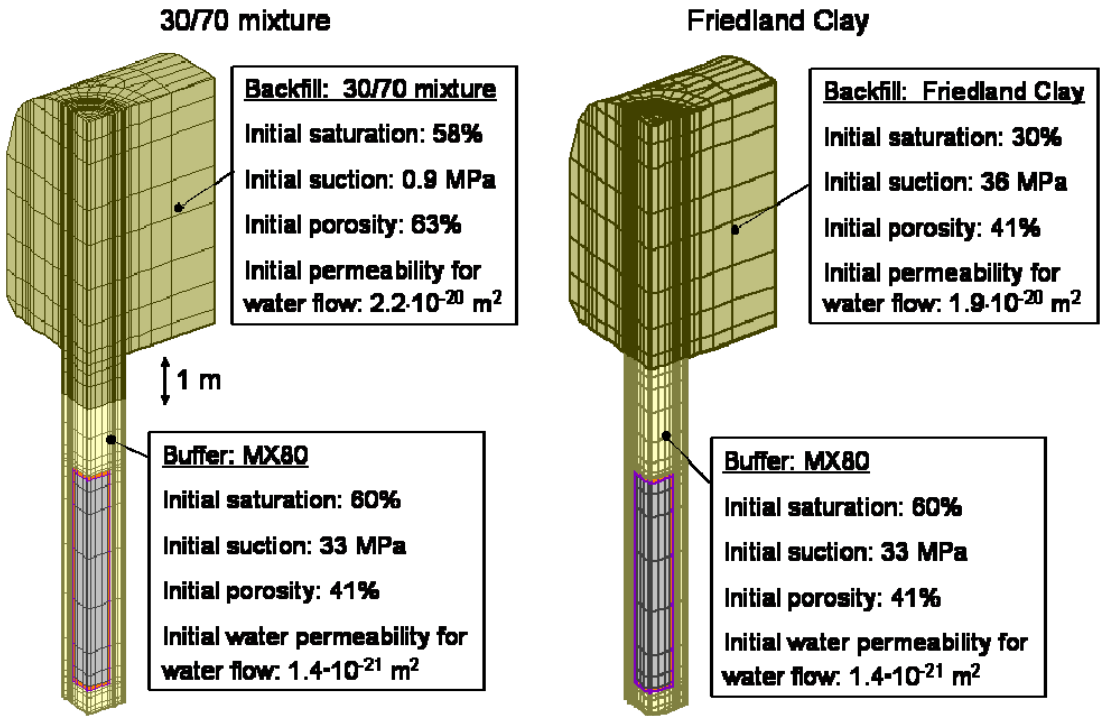

Figure 4.15-1. Comparison of material properties and initial conditions for two alternative backfill materials: (a) 30/70 bentonite-rock mixture and (b) Friedland Clay.

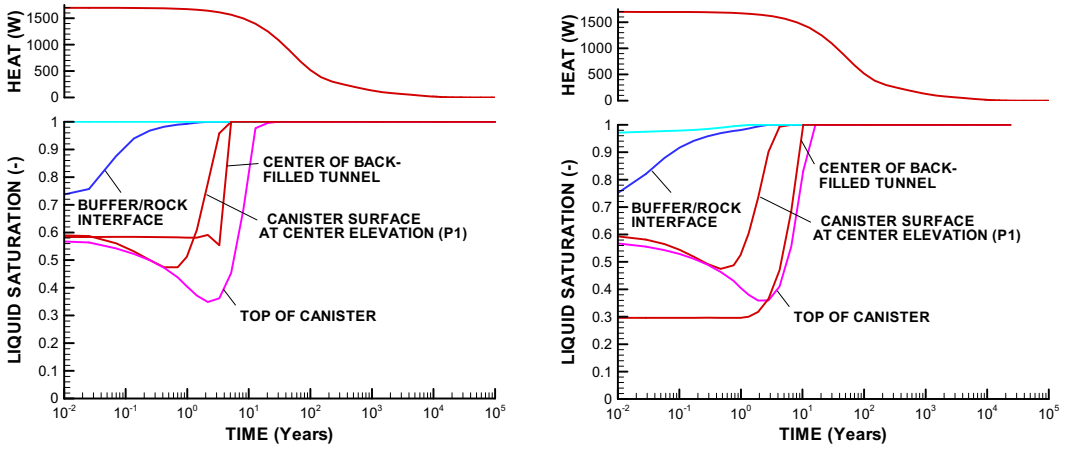

Figure 4.15-2. Variation of backfill properties when intrinsic rock permeability is high ($k = 1 \cdot \times 10^{-16}$ m^2): Evolution of saturation at a repository located at Forsmark when the tunnels are backfilled with (a) 30/70-mixture and (b) Friedland Clay.

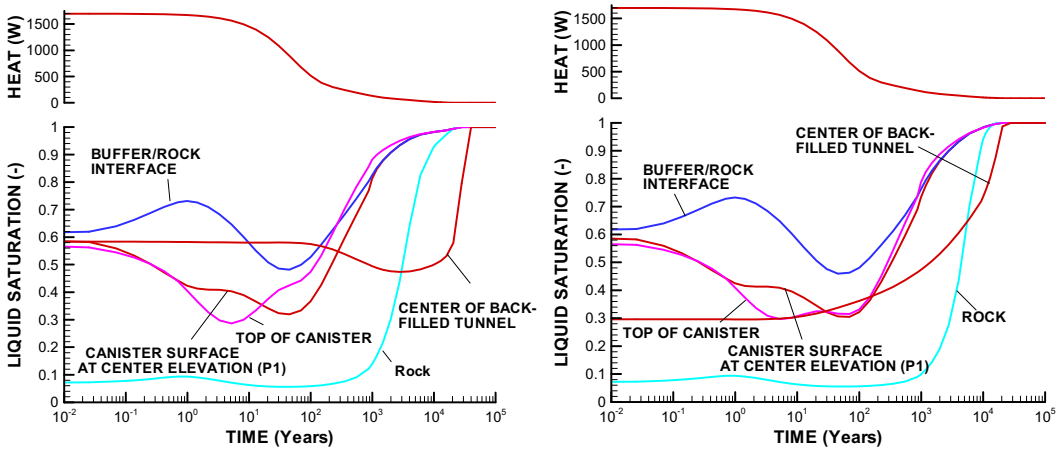

Figure 4.15-3. Variation of backfill properties when intrinsic rock permeability is low ($k = 1\times10^{-20}$ m^2): Evolution of saturation at a repository located at Forsmark when the tunnels are backfilled with (a) 30/70-mixture and (b) Friedland Clay.

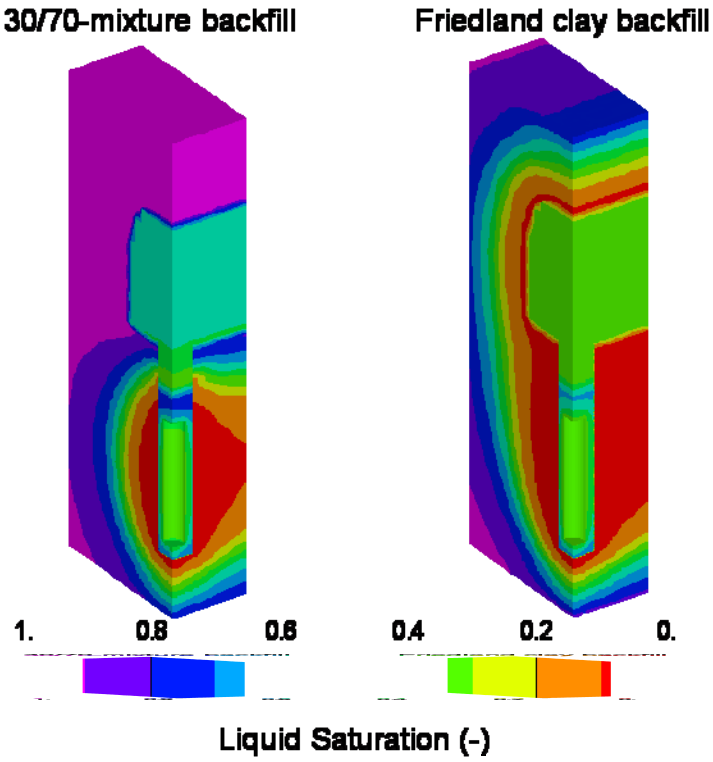

Figure 4.15-4. Variation backfill properties when rock permeability is very low ($k = 1\times10^{-20}$ m^2): Distribution of liquid saturation 1,000 years after emplacement for a repository located at Forsmark when the tunnels are backfilled with (a) 30/70-mixture and (b) Friedland Clay.

4.16 Resaturation from water-bearing fractures in low-permeability rock

In this section, we investigate resaturation from water-bearing fractures in an otherwise low permeability rock matrix ($k = 1.0\times10^{-20}$ m^2). The simulations are conducted by activating selected fractures from those available in the model as shown in Figure 4.1-2. We selected two cases of intersecting fracture geometry:

1) The backfilled tunnel is intersected by a permeable vertical fracture at a lateral distance of 2 m from the center of the deposition hole (Figure 4.16-1a)
2) The lower part of the deposition hole is intersected by a permeable horizontal fracture that is in turn fed by water from a highly permeable vertical fault zone 20 m away from the deposition tunnel (Figure 4.16-1b)

The simulations were conducted for the Forsmark repository alternative, at which inflow from a few discrete fractures might be the more likely because of the very sparse fracture network at that site.

In the model, the fractures are represented by thin solid finite elements with a thickness of 0.05 m. The fracture transmissivity was set to 5×10^{-9} m^2/s, which is an upper limit of fracture transmissivity values used by Börgesson et al. (2006) in their analysis of the effect of intersecting water-bearing fractures. This value of fracture transmissivity is close to the values referred to in SR-Can, SKB 2006a, Section 9.3.8, when estimating the expected resaturation time for both Forsmark and Laxemar repository alternatives. The 5×10^{-9} m^2/s fracture transmissivity corresponds to an equivalent parallel-plate flow aperture of 18.2 μm calculated using the cubic law. In addition we assumed that the suction pressure was two orders of magnitude lower in the fractures than in the matrix. This was simulated by reducing the van Genuchten retention parameter, P_0, from 5.5 MPa to 0.055 MPa. Because of lack of data on retention properties of fractures, the two-order-of-magnitude reduction was chosen arbitrarily, but is consistent with Yucca Mountaindata as shown in Figure 3.2-3.

The results in the following sections (4.16.1 and 4.16.2), will be presented as a comparison of the cases with and without intersecting water-bearing fractures in an otherwise low-permeability rock matrix. Thus, we investigate the impact of intersecting water-bearing fractures.

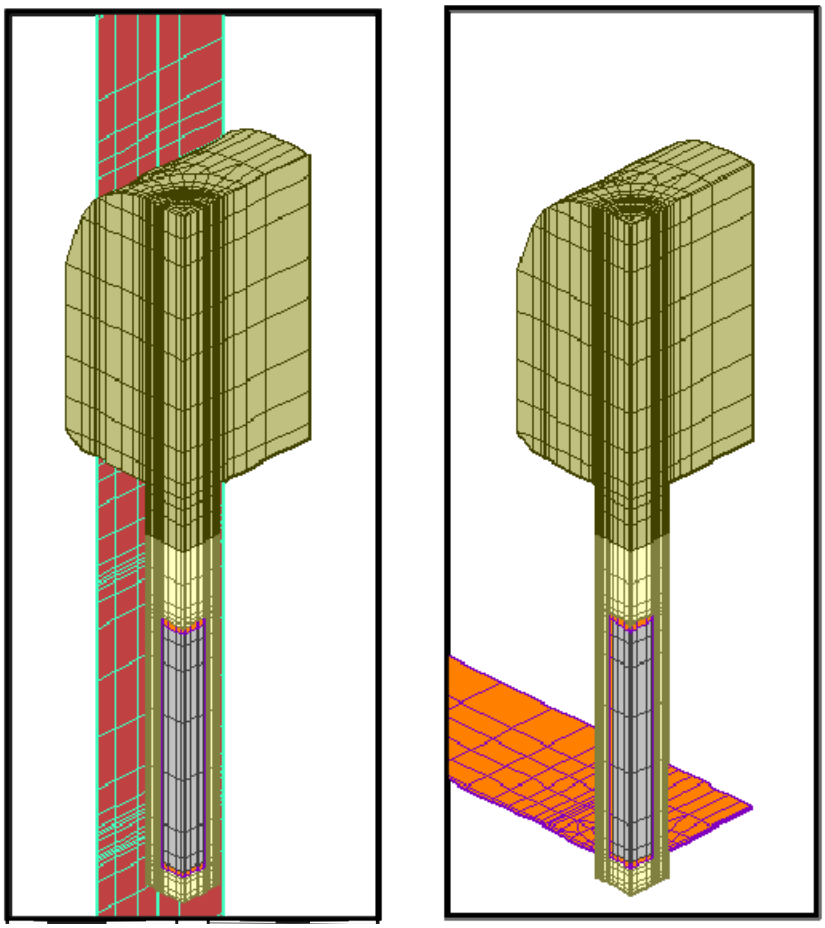

Figure 4.16-1. Two cases of near-field geometry of permeable fractures in a very low permeable matrix ($k = 1\times10^{-20}$ m^2): (a) The backfilled tunnel is intersected by a permeable vertical fracture at a lateral distance of 2 m from the center of the deposition hole, and (b) the lower part of the deposition hole is intersected by a permeable horizontal fracture that is fed by water from a vertical fracture away from the deposition tunnel.

4.16.1 Vertical fracture intersecting the backfilled tunnel

In this case, the vertical fracture extends all the way from the ground surface to the bottom of the model. However, this could also be envisioned to correspond to a case in which there is a local vertical fracture intersecting the backfilled tunnel, and that fracture is connected to a network of conducting fractures that extends from the ground surface and several hundred meters below the repository.

Figure 4.16-2 shows that if the tunnel is intersected by a permeable water-bearing fracture, the resaturation and swelling can be substantially speeded up. Figures 4.16-3 shows that the backfill will be fully resaturated well in advance of the bentonite. The wetting of the backfill begins where the vertical fracture intersects the tunnel and then resaturates the entire buffer within 30 years. The fracture also has an effect on the saturation of the buffer, which is less dry on the side located closer to the fracture.

The time to full resaturation of the backfill has been shortened from 40,000 years to 20 years, whereas the resaturation of the buffer is shortened to about 100 years (Figure 4.6-2b). The speedier resaturation results in a faster development of the swelling stress in both the backfill and buffer (Figure 4.16-4). However, at the time of the peak temperature (around 10 years), the degree of saturation in the buffer and center of the backfill is very similar to the extremely dry case. This means that although a permeable water-bearing fracture intersects the backfill, the buffer will remain dry past 10 years, and therefore in this case peak temperature would still be relatively high. Moreover, the swelling stress in the buffer is not fully developed until about 200 years (Figure 4.16-4). As a result the swelling stress does not develop before the peak thermal stress, and hence the potential for rock-mass failure is still relatively high.

In summary, the intersecting vertical fracture will result in a substantially faster resaturation compared to the case of an extremely low permeability rock without an intersecting fracture. However, our results show that the fracture intersecting the backfill will have a minor impact on the resaturation of the buffer until about 30 years, when the entire backfill has been resaturated. Thus, the buffer will still be very dry at the time of peak temperature, and the swelling stress in the buffer would not be fully developed before thermal peak. Hence, the benefit of support swelling stress on the rock walls cannot be assumed.

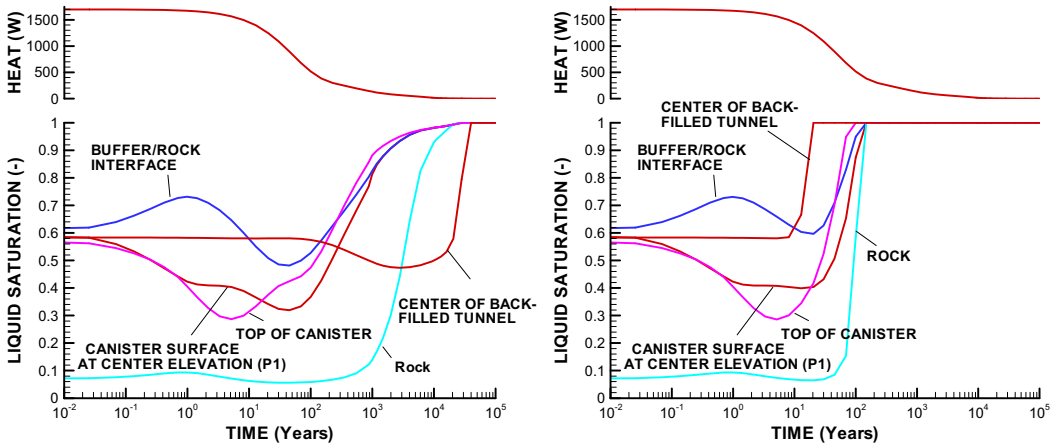

Figure 4.16-2. Impact of a vertical water-bearing fracture intersecting the backfill on the evolution of saturation for a repository located at Forsmark: (a) case of no intersection fracture and (b) case of a vertical water-bearing fracture intersecting the backfill.

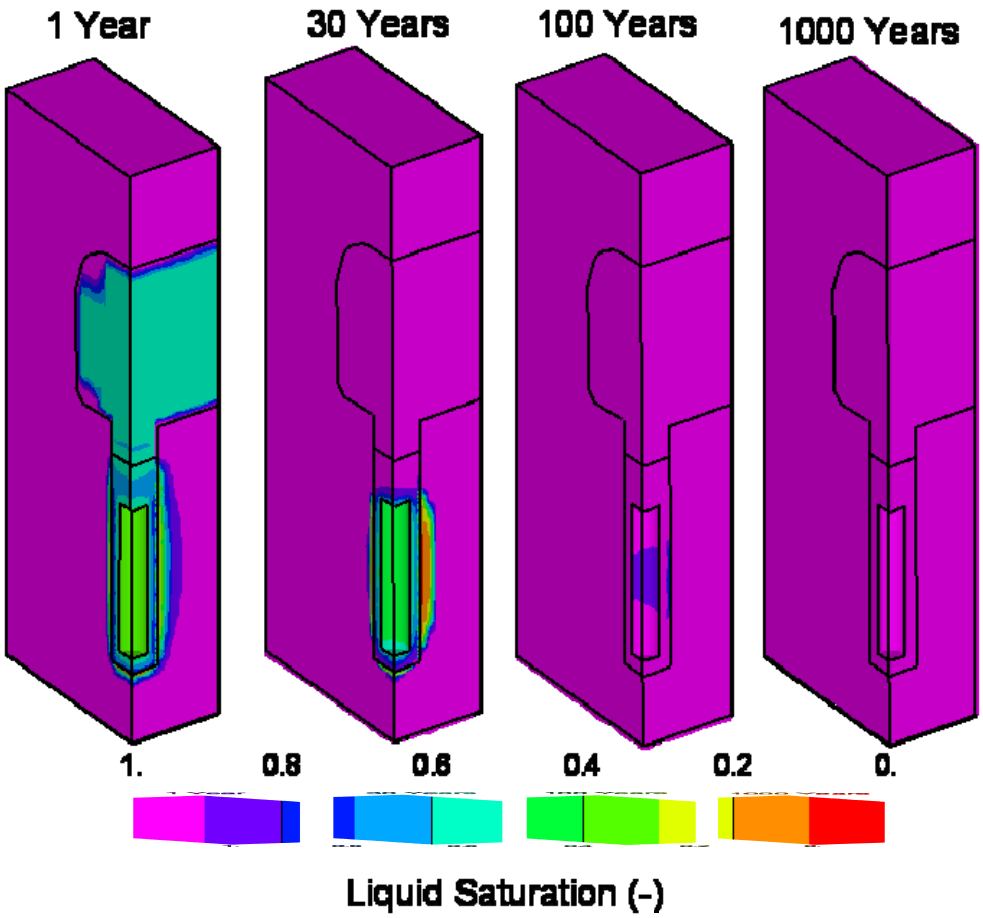

Figure 4.16-3. Distribution of liquid saturation for a repository located at Forsmark for the case of a vertical water-bearing fracture intersecting the backfill in an otherwise low-permeability rock matrix.

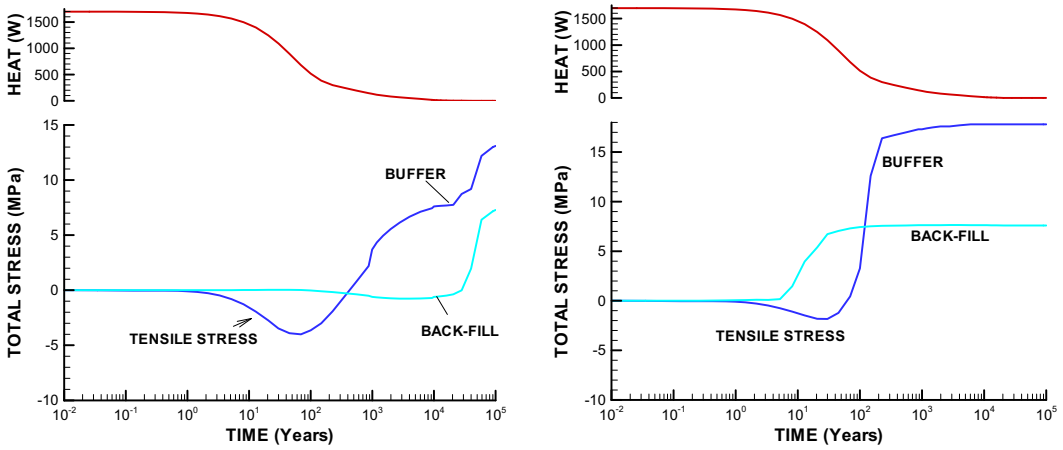

Figure 4.16-4. Impact of a vertical water-bearing fracture intersecting the backfill on the evolution of swelling stress in the buffer and backfill for a repository located at Forsmark: (a) case of no intersection fracture and (b) case of a vertical water-bearing fracture intersecting the backfill.

4.16.2 Horizontal fracture intersecting the deposition hole

In this case, a horizontal fracture extends to a highly permeable vertical fault zone located at the mid-distance between two repository tunnels. That is, the horizontal fracture is connected to the permeable zone at a distance of about 20 m from the deposition hole.

Figure 4.16-5 shows that the intersecting water-bearing fracture substantially speeds up the resaturation processes in both the backfill and the buffer. Figure 4.16-5 indicates that the buffer would be fully resaturated at about 200 years. Moreover, Figure 4.16-6 shows that the resaturation of the buffer takes place gradually from the bottom up, and that the upper parts of the buffer are still very dry at 100 years. The backfill is resaturated once the buffer is resaturated, but it takes about 600 years for the backfill to become fully saturated.

The speedier resaturation from the fracture intersecting the buffer results in a faster development of the swelling stress in both the backfill and buffer (Figure 4.16-6). However, it takes several hundred years for the swelling stress to develop in the buffer and up to 1,000 years in the backfill. This means that the swelling stress does not develop before peak thermal stress, and hence the benefit of support swelling stress on the rock walls cannot be assumed in this case.

In summary, the overall conclusions from the case of a horizontal fracture intersecting the buffer are similar to the case of a vertical fracture intersecting the backfilled tunnel (Section 4.16.3). The presence of the horizontal fracture intersecting the buffer will result in a substantially faster resaturation compared to the case of an extremely low-permeability rock without an intersecting fracture. However, the buffer will still be very dry at the time of peak temperature, and the swelling stress in the buffer would not be fully developed before thermal peak.

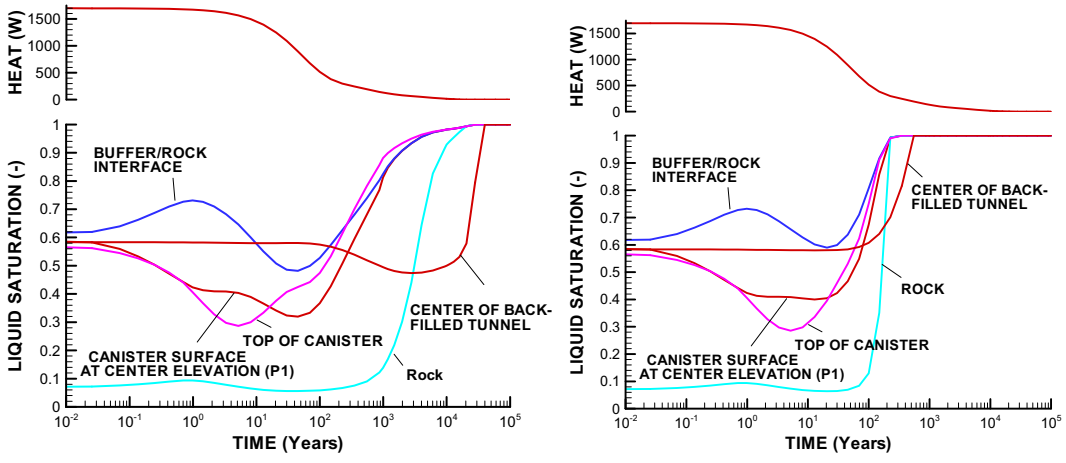

Figure 4.16-5. Impact of a horizontal water-bearing fracture intersecting the buffer on the evolution of saturation: (a) case of no intersecting fracture and (b) case of a horizontal water-bearing fracture intersecting the buffer.

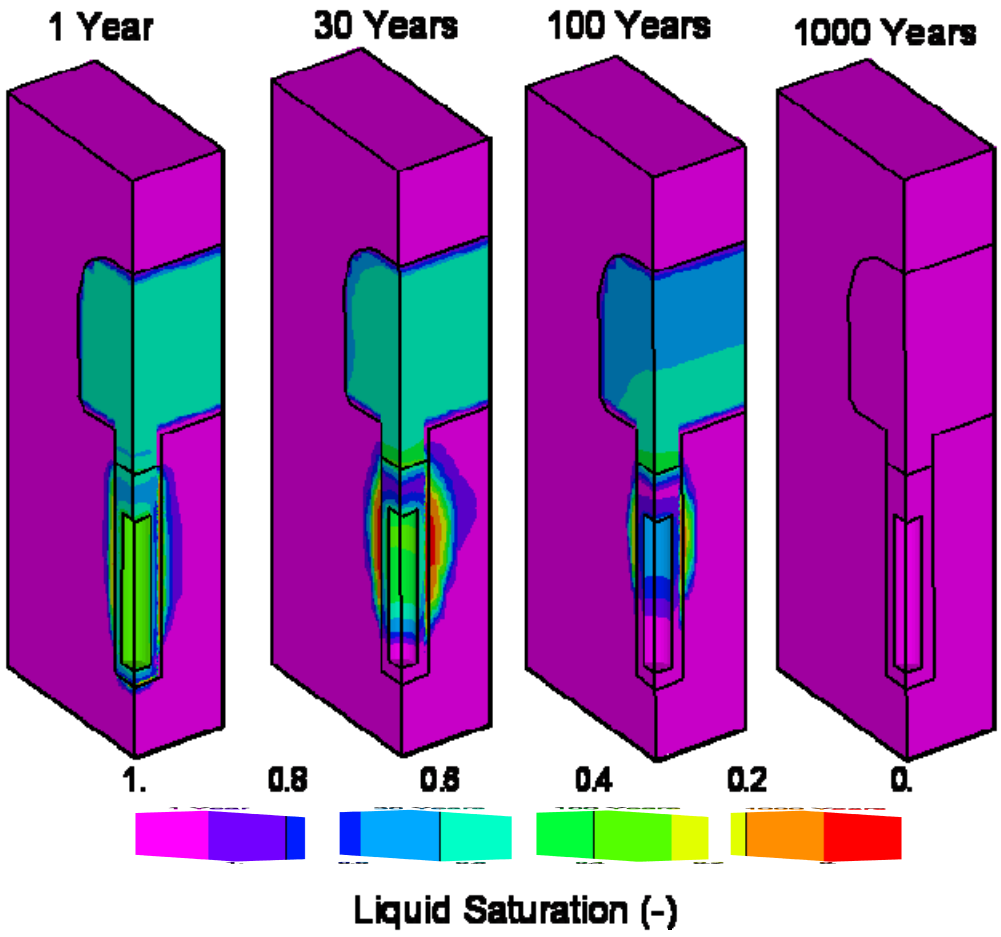

Figure 4.16-6. Distribution of liquid saturation for a repository located at Forsmark for the case of a horizontal water-bearing fracture intersecting the buffer in an otherwise low rock permeability rock matrix.

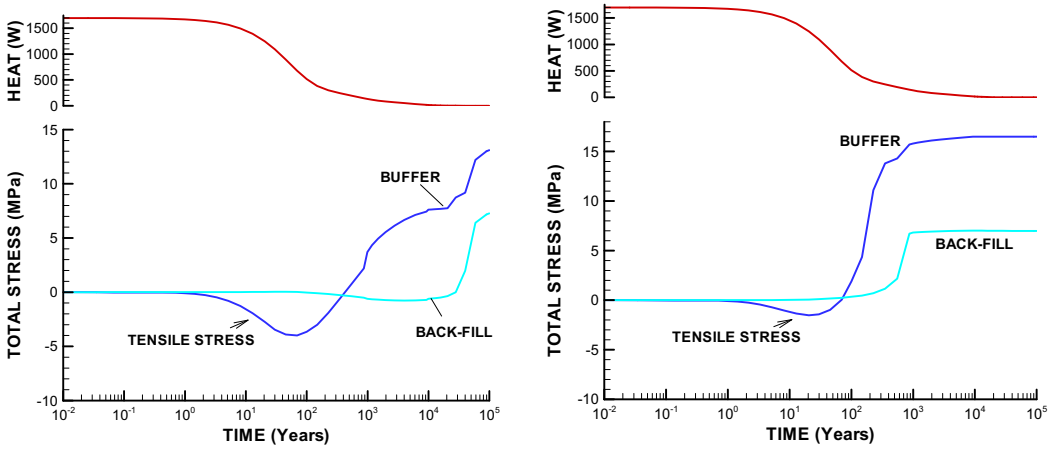

Figure 4.16-7. Impact of a vertical water-bearing fracture intersecting the backfill on the evolution of swelling stress in the buffer and backfill for a repository located at Forsmark: (a) case of no intersection fracture and (b) case of a vertical water-bearing fracture intersecting the backfill.

5 FRACTURE REACTIVATION AND PERMEBILITY CHANGE

THM-induced fracture reactivation and associated permeability changes within the rock are driven by thermal stresses. The evolution of thermal stresses within the rock were calculated for a number of different cases in Section 4. Away from the immediate surroundings of the deposition hole and the tunnel (i.e., at distances larger than a few meters into the rock), the thermal stress evolution depends only on heat decay function and the thermal-mechanical properties of the rock. Away from the tunnels and deposition holes, the temperature and thermal-stress evolutions are independent of issues related to resaturation of the buffer, and hence independent of the properties of the buffer. Thus, the thermal stress evolution can be predicted or bounded confidently by using appropriate values of thermal and thermal-mechanical properties of the rock. However, it is much more difficult to predict how much permeability might change as a result of the expected evolution of thermal stress.

We can divide possible THM-induced fracture reactivation and permeability changes in to two types of reactivation:

1) Changes in permeability as a result of changes in stress normal across fractures (normal stress reactivation).
2) Changes in permeability by changes in shear stress along fractures (shear reactivation).

These two processes may occur simultaneously and may partly offset each other. During the thermal period at a repository, the first processes are expected to cause a decrease in permeability, especially in the vertical direction as stresses in the horizontal direction are expected to increase, and hence aperture and total permeability of subvertical fractures are expected to decrease. The second processes could cause the permeability to increase if shear reactivation and associated shear dilation of connected fractures occurs. Such shear reactivation could occur if the shear stresses acting on the fractures exceed a critical value for shear failure. The resulting changes in permeability of rock mass include both changes in the mean value and distribution of permeability. For example, Min et al. (2004) showed by a discrete fracture analysis that shear reactivation will cause the flow to concentrate along reactivated fractures, along which the flow may increase by orders of magnitude.

In what follow of this section, we discuss the potential for changes caused by the two processes in the light of SKB work in this area. A full prediction of permeability changes at both sites would require much more effort in a far-field repository scale model and is outside the scope of this study.

5.1 Potential permeability changes with changes in normal stress across fractures

The simulation results shows that stresses normal to fractures are going to increase during the thermal period, except perhaps close to tunnels and deposition holes, where stresses normal to fractures could increase as a result of excavation. Bounds for possible permeability changes may be estimated based on the nonlinear stress-versus-permeability relationship of fractures. For example, Figure 5.1-1 illustrates how

permeability could change, and how the permeability changes might be bounded at different depths. For example it is shown that at a depth of about 500 m (between 100 m and 1 km in Figure 5.1-1), the fractures might be near their residual aperture and permeability may not change much upon increasing normal stress. On the other, if the fractures are unloaded, for example near a tunnel, the permeability could increase substantially. This is also in agreement with the calculated results obtained by the SKB. Away from the immediate surroundings of the tunnels, and deposition holes, permeability may decrease a little because of thermal compressive stress, which would tend to compress fractures to smaller apertures. However, this permeability reduction would be limited, because fractures at the depth of the repository horizon are near their residual value.

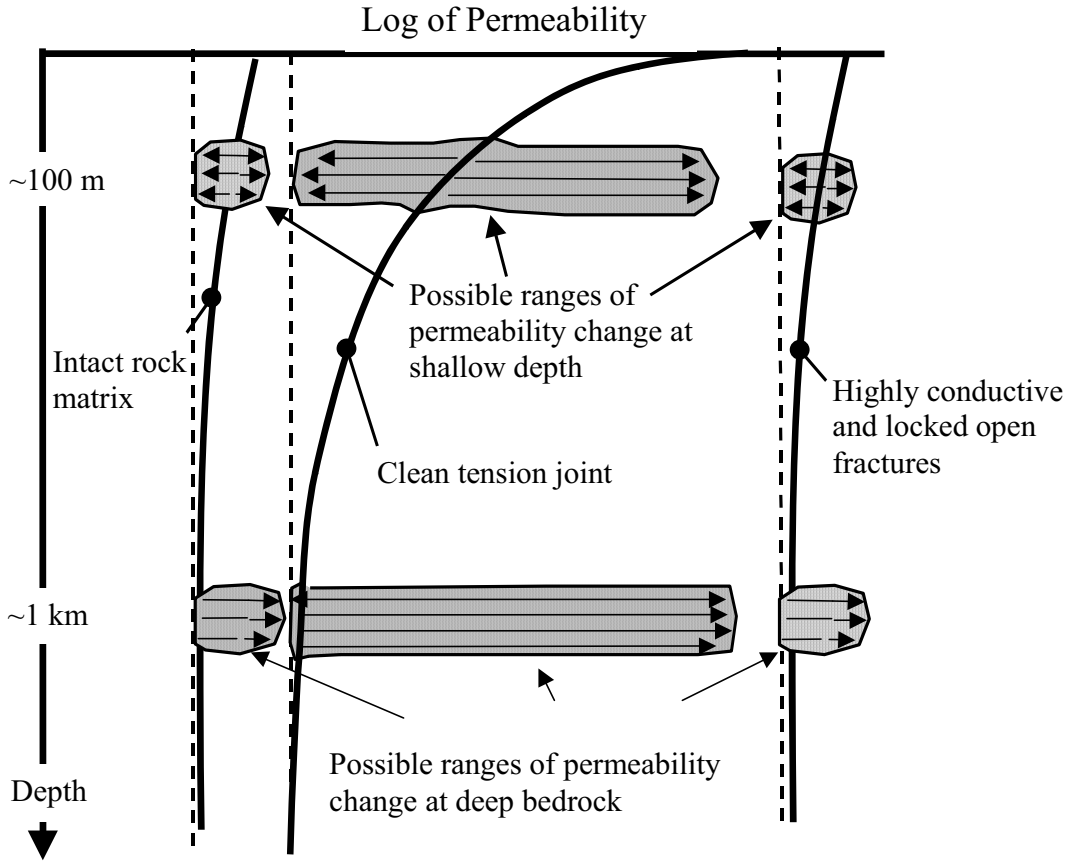

Figure 5.1-1. Schematic picture showing possible permeability changes at shallow and deep locations in fractured bedrock. The solid lines represent the depth- (or stress)-permeability function for intact rock, clean tension joint and highly conductive and locked open fractures. The dashed lines represent residual permeabilities at high compressive stress (from Rutqvist and Stephansson, 2003).

In general, we believe that SKB's evaluation of permeability by normal stress, at least in terms of mean permeability change, may be reasonable. However, the results of SKB are valid for the case of clean tension joints evaluated from laboratory tests on volcanic tuff samples. The stress permeability function for granite might be similar for a clean fracture. However, in the field, there is a wide range of fractures, including clean tension joints, as well major shear fractures that might be "locked open," as shown in Figure 5.1-1. More importantly, there might be fractures that are partially filled with minerals that could clog completely (to zero permeability) upon increased normal stress. One example of such behavior is the results of Makurat et al. (1990) on the NGI *in situ* block experiment in Stripa, which showed that fracture permeability could decrease to zero when stresses normal to the fracture increased over a certain threshold stress.

Ideally, the stress-versus-permeability relationship should be determined by *in situ* experiments. Rutqvist et al. (1997) presented such *in situ* experiments for KLX02 at Laxemar. The *in situ* hydromechanical properties were inferred from a so-called hydraulic jacking test (also called a step-rate test) conducted in single boreholes. Hydraulic jacking tests were conducted by a step-wise increase of the fluid pressure. At each step, the well pressure was kept constant for a few minutes until the flow was steady (Figure 5.1-2a). The numerical analysis of these injection tests shows that the flow rate at each pressure step is strongly dependent on the fracture aperture and normal stiffness of the fracture in the vicinity of the borehole, where the pressure changes the most (Figure 5.1-2b). Figure 5.1-2c shows field-test results of a hydraulic jacking test on a fracture at 267 m depth, in the crystalline fractured rock at Laxemar (Rutqvist et al. 1997). At the first cycle of step-wise increasing pressures, the flow rate increases as a nonlinear function of pressure. A temporal peak-pressure is obtained at a flow rate of 1.3 liters/minute before the pressure begins to decrease with an increasing flow rate. A shear-slip analysis of the particular fracture, which was inclined to the principal *in situ* stresses, indicated that these irreversible fracture responses could be caused by a shear slip, as the fluid pressure reduced the shear strength of the fracture. The subsequent step-pressure cycle took a different path because of the change in hydromechanical properties resulting from shearing and fracturing.

The overall results from the hydraulic jacking tests conducted at Laxemar showed that the pressure sensitivity of the fractures is strongly dependent on the initial hydraulic permeability. The permeability of the most conductive fractures is relatively insensitive to injection pressure, whereas the permeability of the least conductive fractures can be strongly dependent on the injection pressure. From the borehole-televiewer image, the most conductive fractures appear to be open fractures that are incompletely cemented, indicating flow channels in a fracture that are "locked open" by shear dislocation or mineral filling (Rutqvist et al. 1997).

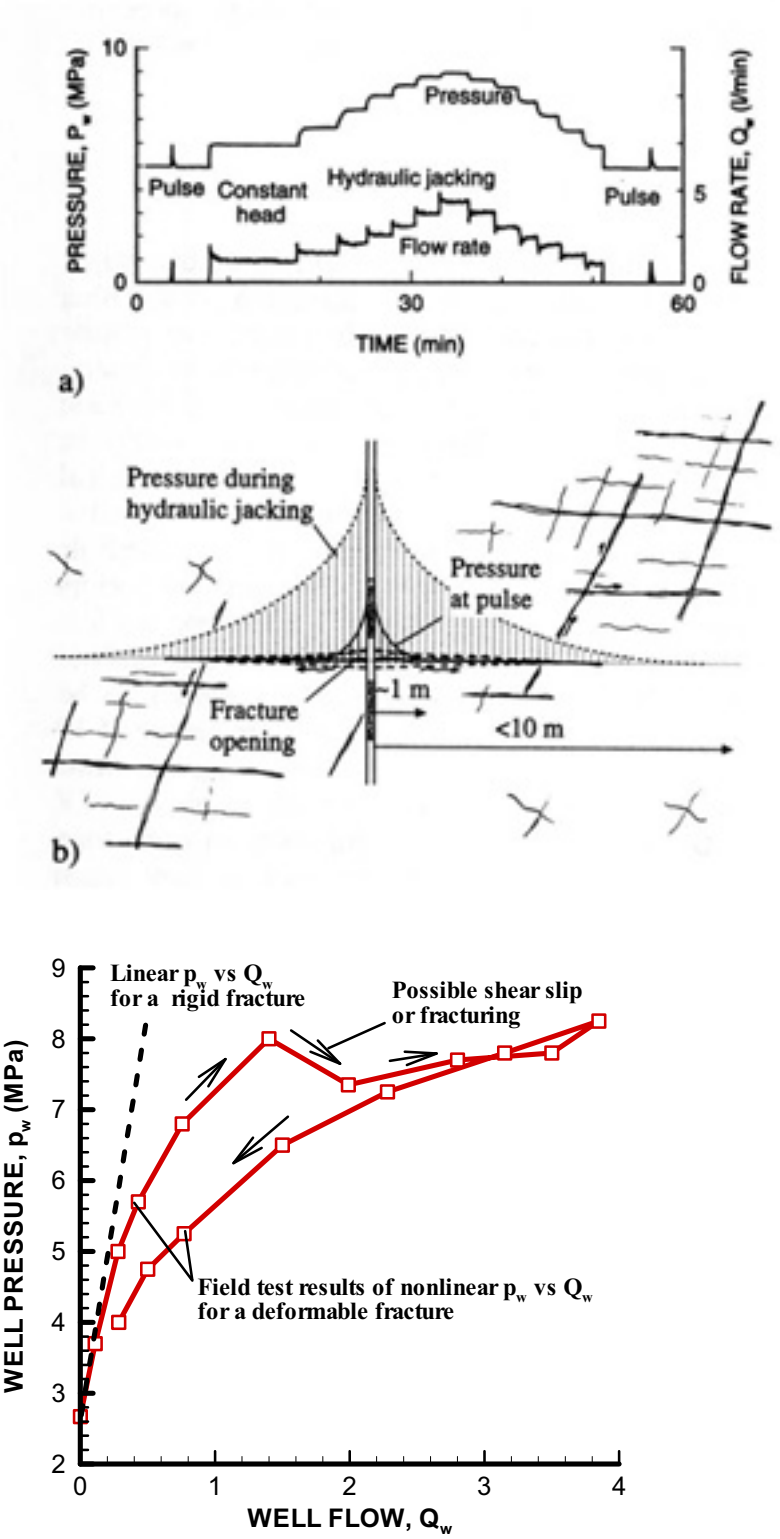

Figure 5.1-2. *In situ* determination of normal stress versus transmissivity relationship using a combination of pulse, constant head, and hydraulic jacking tests: (a) schematic representation of pressure and flow versus time, (b) the radius of influence in each test, and (c) results of hydraulic jacking test (Rutqvist et al. 1997).

Figure 5.1-3 shows the stress-versus-transmissivity relationships derived from the *in situ* hydraulic jacking tests at KLX02 at Laxemar. These fractures were tested at a depth of about 250 to 300 m and were all located near high-flow zones along the KLX02 borehole. The tested fractures represent different types of fractures. For example, the fracture at 315 m is a single fracture that is highly permeable, but might be locked open by previous shear displacements, as its transmissivity is relatively insensitive to stress. The tests at 316 and 336 indicated a fracture transmissivity that is very sensitive to changes in normal stress; the transmissivity would go to zero at high stress. This could be explained by fracture mineral filling that would tend to clog the fracture at high normal stress. The stress-versus-transmissivity relationship used for the SR-Can by Hökmark et al. (2006) is somewhat similar to that of the fractures located at 266 and 267 m in Figure 5.1-3. Thus, from an initial effective stress of about 10 MPa, the transmissivity may increase by one order of magnitude upon unloading or could decrease to a factor of about 50% upon loading. However, fractures in Figure 5.1-3 may represent relatively permeable fractures, as the injection tests were conducted near high flow zones of the KLX02 borehole.

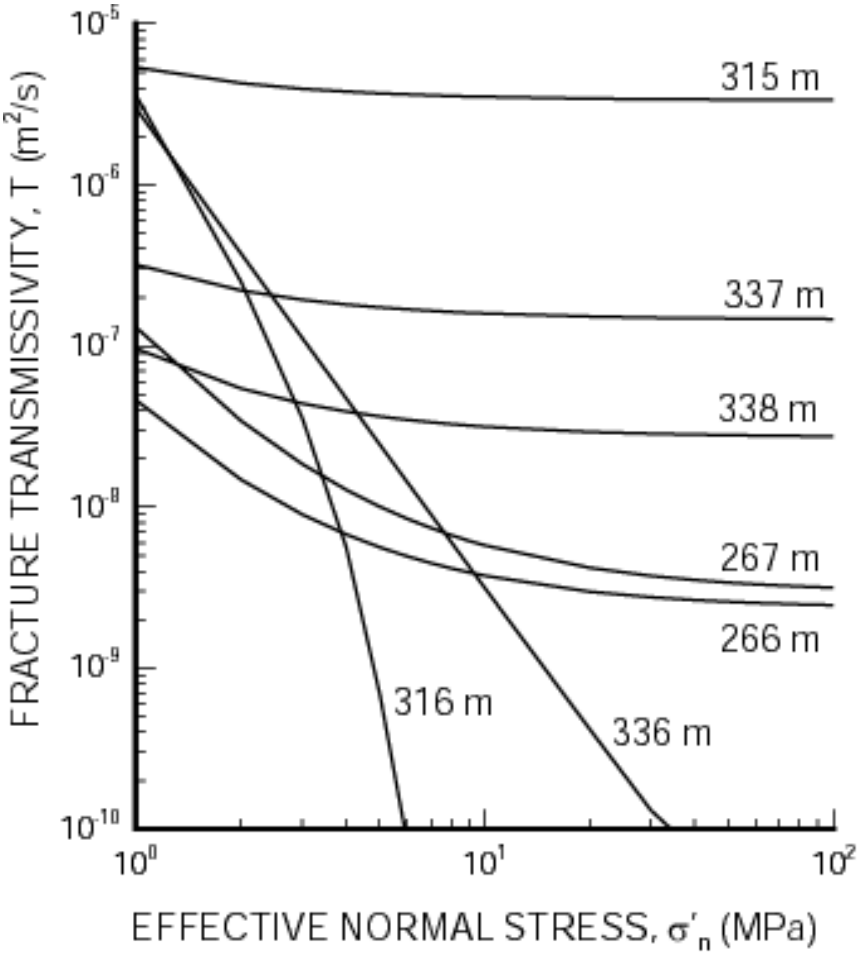

Figure 5.1-3. Transmissivity-versus-stress relationship estimated from *in situ* hydraulic jacking tests on single fractures at the KLX02 borehole at Laxemar.

5.2 Potential for permeability change by shear reactivation along fractures

To evaluate the potential for shear reactivation, we perform an analysis of the effective principal stress path. As discussed in Section 3.5, many studies have shown that fractures favorably oriented for shear-slip, so-called critically stressed fractures, tend to be active groundwater flow paths (Barton et al., 1995; Ferill et al., 1999; Rutqvist and Stephansson, 2003). Importantly, a correlation between shear stress and hydraulic conducting fractures has also been reported for the rock mass at Äspö Hard Rock Laboratory (Talbot and Sirat, 2001). Talbot and Sirat (2001) correlated the number of wet fractures to different stress regimes in the current stress field. Most wet fractures are subhorizontal in the stress regime prone to thrusting in the upper few hundred meters, and subvertical with NW trending in the underlying stress regime prone to strike slip faulting. Barton et al. (1995) in studying the correlation between shear stress and hydraulic conducting fractures at the lithospheric plate boundary in California, found that water-conducting fractures correlated with the maximum shear stress for a coefficient of friction, ranging from $\mu = 0.6$ to 1.0. Based on these observations, we will study how the principal effective stress path evolves in relation to stress conditions corresponding to $\mu = 0.6$ to 1.0.

From the site descriptive models of Forsmark (SKB 2005) and Laxemar (SKB 2006b) it appears that no attempt has been made to investigate the potential correlation between water conductive fractures and the stress field. The stress field at Laxemar might be similar to that of Äspö, and therefore we may expect similar correlation between the stress regime in Laxemar as found by Talbot and Sirat (2001) for Äspö. In the site descriptive model for Forsmark, it is stated that open, partly open, and sealed fractures occur in all the different orientation sets. However, there is a concentration of open and partly open fractures in the subhorizontal fracture set and a concentration of sealed fractured in steeply dipping sets (Forsmark site descriptive report, SKB 2005, Section 5.2.7). Because the stress field at Forsmark can be characterized as prone to thrust faulting, this indicates that there is indeed a correlation between *in situ* stress and water conducting fractures also at Forsmark.

Figure 5.2-1 presents the results of the predicted stress paths at the depth of the repositories (400 m for Forsmark and 500 m for Laxemar), assuming the initial stress field according to the ideal base case. First of all we can observe that the initial stress field would correspond to the conditions of a coefficient of friction to $\mu = 1.0$. This corresponds to a stress ratio (ratio of maximum to minimum compressive effective stress) of 5.8. That is, the maximum principal effective stress is 5.8 times the minimum principal effective stress. The initial stress regime at Forsmark would be prone to reverse faulting, whereas the initial stress regime at Laxemar would be prone to strike slip faulting. The interpreted stress ratio of 5.8 appears to be high, which may indicate that many fractures are indeed critically stressed for shear.

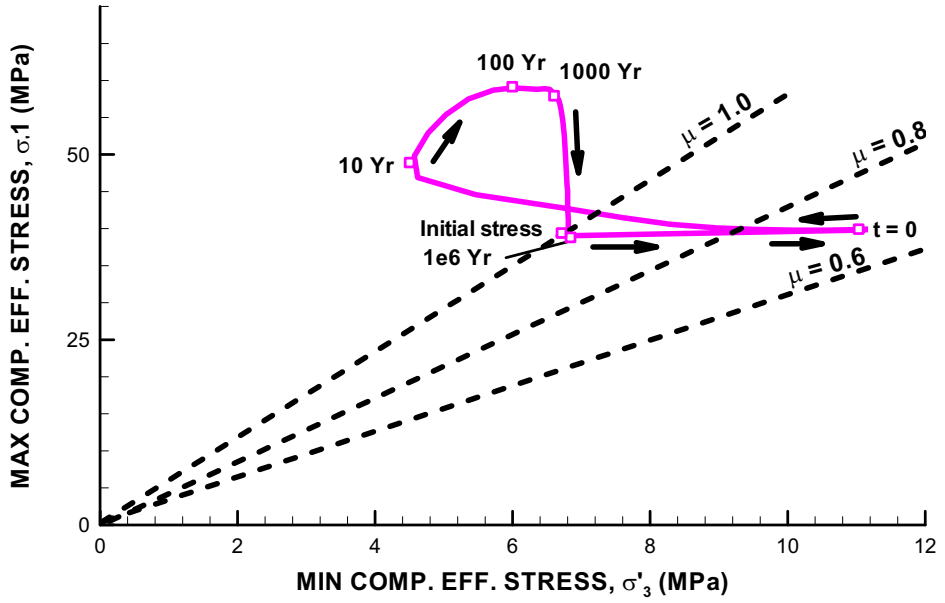

(a) Forsmark

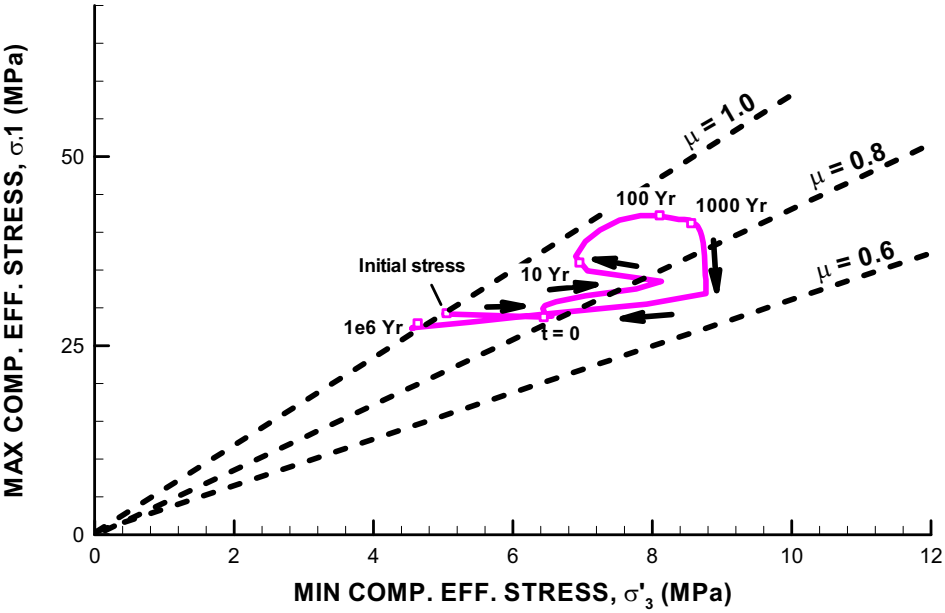

(b) Laxemar

Figure 5.2-1. Evolution of the principal stress path in the rock mass at the depth of the repository in comparison to different frictional coefficients that are likely to induce shear slip along existing fractures (μ = 0.6 to 1.0), for a repository located at (a) Forsmark and (b) Laxemar.

Figure 5.2-1 shows that the principal stress path is quite different for the two sites. This difference is caused by the difference in the initial stress regime. At both sites, the stress path initially moves away from the conditions of high effective-stress ratio (from initial stress to t = 0). This is caused by the initial dewatering and reduction in fluid pressure during the excavation of the tunnel, which tends to increase the minimum compressive stress. However, after emplacement, the water pressure recovers, and thermal stresses increase in the horizontal direction. This causes the principal stresses to move towards a condition of likely failure, with the highest potential for shear failure occurring between 10 to 1,000 years. Figure 5.2-1 also shows that the stress ratio becomes much higher at Forsmark compared to Laxemar. At Forsmark, the initial thrust faulting stress regime implies that shallowly dipping fractures would be most prone to shear, a tendency amplified during the heating phase as the horizontal stress increases. At Laxemar, on the other hand, the increased horizontal stress during heating causes the stress regime to shift from the initial strike-slip faulting to thrust faulting.

Another way of analyzing the evolution of the stress path is shown in Figure 5.2-2. We recognize that the magnitude of the initial stress field is uncertain. However, if we assume that the initial stresses are limited by friction, and we assume that the rock mass is critically stressed for shear, we may evaluate changes in stress state and investigate whether the stress state changes in such a way that further shear slip would be likely or unlikely. Figure 5.2-2 shows that further shear reactivation is more likely at Forsmark than at Laxemar, but shear reactivation would also be likely for a coefficient of friction μ = 0.8 or 0.6. At booth sites, fracture reactivation during the heating phase would preferably take place in shallowly dipping fractures. Such fracture reactivation could increase the permeability of already open critically stressed fractures, and may reactivate sealed fractures that could open new flow paths connected to water-conducting fractures.

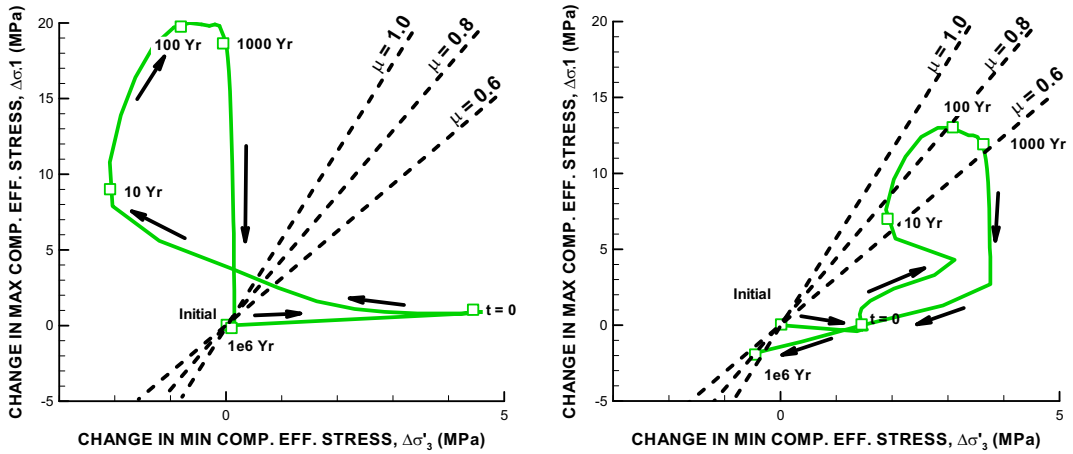

Figure 5.2-2. Evolution of the principal stress path (changes relative to initial conditions of a critically stressed rock mass) at the depth of the repository in comparison to different frictional coefficients that are likely to induce shear slip along existing fractures (μ = 0.6 to 1.0) for a repository located at (a) Forsmark and (b) Laxemar.

5.3 Estimating overall changes in permeability by fracture reactivation

In this report, we do not provide a complete analysis of permeability changes and its potential impact on radionuclide transport. Based on our discussion and analysis in Sections 5.1 and 5.2, we can draw some general conclusions regarding expected or potential changes in permeability.

It is clear that permeability in subvertical and steeply dipping fractures is going to decrease around the repository, because of the increase compressive horizontal stresses. The decrease in the mean may be limited to 50% of the original permeability at the level of the repository. However, the magnitude permeability decrease is expected to vary widely, from almost no change (in locked open fractures) to several orders of magnitude (in fractures partially filled with soft minerals), depending on the fracture properties. On the other hand, the increasing compressive horizontal stress will lead to increased shear stresses on shallowly dipping fractures, which could slip and dilate leading to increase permeability (Figure 5.3-1). The magnitude of increase in permeability of those fractures that slip may also be strongly dependent on their *in situ* conditions, but could be several orders of magnitude. A fracture that is initially sealed with mineral filling may show the strongest increase during shear, with the seal broken down and possibly opening up a new flow path. Fractures that have been previously sheared, probably the most conductive fractures in the field, may keep opening during additional shear, but may not increase their permeability much further, as they may already be fully dilated. The fractures may not slip immediately, because fracture plane cohesion might prevent them from slipping. However, a high shear stress will be sustained for several thousand years, which means that fracture slip may occur on fractures exposed to a shear-to-normal stress ratio as low as 3, corresponding to a coefficient of friction of 0.6. Thus, according to this conservative bound, we can conclude that there is a very high potential for shear reactivation during the thermal period. Moreover, permeability changes by shear reactivation would be permanent, unless sealing by fracture mineral precipitation offsets them.

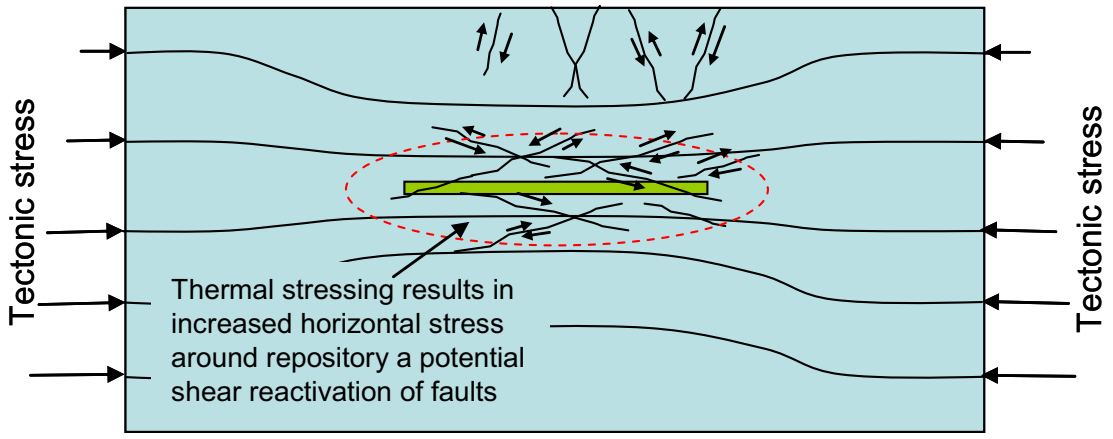

Figure 5.3-1. Schematic of potential massive shear reactivation in the fractured rock mass as a result of thermal stressing in a rock mass that might already be critically stresses for shear.

6 SUMMARY OF RESULTS AND DISCUSSION

In this section, we discuss the results of our analysis in Section 4 and 5 in the light of the four main items related to SKB's THM analysis overviewed in Section 3.

6.1 Thermal evolution and peak temperature

Our analysis shows that the peak temperature would not exceed 80°C for an ideal case if the resaturation is timely, which it would be if the properties of the bentonite are indeed those determined by SKB from short-term laboratory experiments. However, our analysis also indicates that if unexpectedly severe drying of the buffer would occur as a result of dry rock conditions and conservatively bounded bentonite properties, it is possible that a peak temperature very close to 100°C could be achieved in the buffer. Specifically, we show that if the inner part of the buffer would be dried to less than 20%, then the peak temperature may well exceed 100°C. SKB's analysis needs to assure that such extreme drying will not occur. In fact, SKB's own three-dimensional model analysis shows that the buffer may dry to 20% (Börgesson et al., 2006, Figure 7-14), but in that case the resaturation was relatively fast due to an assumed nearby constant fluid-pressure boundary. We realize that the assumed upper bound of the thermal diffusion coefficient may be too conservative. However, the experimental data for determining this very important parameter seems to be quite limited and conducted at a different initial void ratio and different initial saturation than the expected *in situ* conditions at emplacement. Therefore, thermal diffusivity and thermal conductivity parameters need to be further validated against longer term and larger scale experiments, perhaps under dry rock conditions. Meanwhile, we believe that conservatively bounded input properties, rather than average properties, should be considered in the safety assessment.

6.2 Hydrological evolution and resaturation time

Our analysis shows that the time to full resaturation of the buffer and backfill would be about 10 years for an ideal case of a relatively high rock-mass permeability. However, our analysis indicates a substantially longer resaturation time than SKB's assessment when the permeability of the rock is low. Our analysis shows that if the rock permeability is low, the time to full resaturation is strongly dependent on the distance to the outer hydrostatic constant pressure boundaries. For example, for an extremely (but not unrealistic) low rock hydraulic conductivity of $k = 1\times10^{-13}$ m/s, our analysis shows that it would take 30,000 to 40,000 years to full resaturation, whereas SKB's analysis indicates that it would take 570 years. SKB analysis is conducted with a constant pressure boundary located 12 m from the deposition hole, which is much closer than in our analysis in, which the boundaries are placed far away. Consequently, SKB's assessment of time to resaturation is valid only for the case of an assumed distance to the constant pressure boundary of 12 m.

Our analysis agrees with that of SKB's concerning the resaturation of the buffer from the backfill of type 30/70. Thus, if the rock has a very low permeability or is even completely impermeable, the buffer will resaturate to above 90% by water feeding from the overlying backfill, if the 30/70 backfill option is adopted. However, this will take several thousand years, due to a very low permeability for water flow within the backfill at emplacement. Moreover, water sucked into the buffer would cause a decrease in saturation of the overlying backfill, and hence no swelling stress would

develop in the backfill for a very long time. Thus, the safety-function indicator for a swelling stress of at least 0.1 MPa in the backfill might not be achieved for up to 100,000 years. Moreover, if the backfill shrinks as it is desaturated by suction from the buffer, gaps may open at the backfill and rock interface.

Our analysis also shows that if the thermal diffusion coefficient D_{TV} is higher than the value assumed by SKB, a stronger-than-expected drying of the buffer may occur, which would in turn delays the resaturation process. The thermal diffusion coefficient is a very important parameter for the evolution of saturation within the buffer. A small change in this parameter may have a big impact on the resaturation time. As discussed in Section 5.1, until further validation of this parameter, a conservative rather than average matched value should be adopted in the safety assessment.

Our analysis shows that the retention properties of the rock and its relation to the retention properties of the buffer and backfill are important for the resaturation process. A lowering of the retention curve by an order of magnitude caused a delayed resaturation for up to one order of magnitude for a low intrinsic rock permeability. On the other hand, the relative-permeability function of the rock appears to have very small impact on the resaturation process. Because of the strong impact of the rock's retention curve, greater efforts should be taken to evaluate the *in situ* retention properties of the fractured rock.

Our analysis shows that the choice of backfill material between 30/70 mixture and Friedland Clay will have a minor impact on the resaturation processes, at least when the permeability of the rock is relatively high. There is, however, one fundamental difference between the two backfill alternatives, which might be important for the safety assessment. In the case of Friedland Clay, the initial saturation is only 30%, leading to high suction pressure (slightly higher than in the bentonite buffer). This means that if the rock were completely impermeable, the buffer would never resaturate by water from the overlying backfill, but would remain dry at the initial saturation of 60%, or slightly lower.

Our analysis shows that water-bearing fractures intersecting the backfill or buffer can substantially speed up the resaturation time in an otherwise low-permeability rock. However, the analysis indicates that the buffer would still not resaturate until after several hundred years. As a result, the buffer would still be very dry and have a low thermal conductivity at the time of peak temperature, and swelling stress would not be developed before the peak thermal stress. Moreover, the resaturation from an intersecting fracture would be limited by the water supply provided by the contact area between the bentonite and the intersecting water-bearing fracture. The assumed condition with a hydraulic contact in a 5 cm thick fracture element around the entire periphery of the tunnel or deposition hole, is not the most conservative case. In reality, the contact area may be limited to a flow channel or intersecting fractures leading to a point supply of water.

6.3 Mechanical evolution, EDZ and rock spalling around openings

Our analysis agrees with SKB's in that there would be a high risk for spalling around the deposition holes for a repository at both Forsmark and Laxemar. Our analysis

indicates that the potential for spalling or tensile failure around the deposition holes is much higher at Laxemar than Forsmark, assuming that SKB's interpretation of the stress field is accurate. The higher potential for spalling at Laxemar is a result of lower rock-mass strength and the fact that the *in situ* stress field at Laxemar appears to be more anisotropic in the horizontal plane (i.e. $\sigma_H \geq \sigma_h$) than at Forsmark. A contributing factor to the high potential for spalling at Laxemar is also the fact that in our analysis, we conservatively assumed that the maximum principal stress is oriented normal to the emplacement tunnels at Laxemar. Such a conservative assumption is justified by the fact that SKB chose to orient the emplacement tunnels at a Laxemar repository without consideration of the *in situ* stress field, and hence some of the tunnels would be close to being perpendicular to the maximum principal *in situ* stress. Our analysis shows that the potential for spalling could be greatly reduced if the tunnels at Laxemar were oriented with their axis along the direction of the maximum principal stress. This consideration would be especially effective at Laxemar, where the *in situ* stress field is thought to be much more anisotropic than at Forsmark. For a repository at Forsmark, our analysis indicates that the amount of spalling might be rather limited, although there is still a high potential for the assumed *in situ* stress condition. One great uncertainty in the analysis of the potential for rock spalling is the magnitude of the initial stress field. It is therefore wise of SKB to assume that spalling could occur, since it cannot be guaranteed that it will not occur. Moreover, if Laxemar is selected as a repository site, the orientation of the tunnels relative to the *in situ* stress field should be reconsidered, because this might greatly reduce the potential for rock failure around the deposition holes.

Our analysis shows that tensile stress will develop in the side walls of the emplacement tunnels. At Forsmark, such tensile stress would develop after emplacement and closure during the thermal period, and is a result of increased horizontal thermal stress in combination with swelling stress within the backfill. At Laxemar, tension would occur at excavation, due to unfavorable orientation of the tunnels relative to the *in situ* stress field. The tension in the rock wall would either tend to create new tensile fractures that would be oriented horizontally or open up pre-existing horizontal fractures. This would induce a zone of substantially increased permeability along the tunnels. Moreover, such fracturing would tend to connect an otherwise discontinuous EDZ, creating a continuous EDZ along the tunnel.

Our analysis assumes that the long-term strength of the rock mass is about 50% of the short-term strength of a small-scale core sample. This is consistent with Martin (2005) and with the assumptions made by SKB. It is assumed that the *in situ* strength observed (for example) at the pillar stability experiment at Äspö Hard Rock Laboratory is in fact the long-term rock-mass strength. It is not at all certain that the observed *in situ* rock-mass strength will be valid over thousands of years. Thus, our analysis may not be the most conservative one with regard to failure potential.

6.4 THM induced fracture reactivation and permeability change

Our analysis shows that increasing horizontal stresses around the repository region will induce a reduction of permeability in steeply dipping fractures, but may also cause shear reactivation along shallowly dipping fractures that could open up new flow paths. In steeply dipping fractures, the decrease in mean permeability may be limited to 50% of the original, at the level of the repository. However, the magnitude

of permeability decrease is expected to vary widely, from almost no change (looked open fractures) to several orders of magnitude (open fractures filled with soft mineral filling), depending on the fracture properties.

Our analysis shows that because the stress field is highly anisotropic on both sites, fractures may be critically stressed already at the initial state of stress. In fact, our analysis indicates that using long-term frictional limits, the stress field might be less anisotropic than SKB's interpretation of the initial stress field. Our analysis shows that during the heating phase, the horizontal stresses will increase substantially and remain high for several thousand years. Increasing the horizontal stresses, while the vertical stress remains almost constant will result in increased shear stress that will reactivate shallowly dipping fractures. Figure 3.4-2 shows how such shear reactivation might induce increased permeability and channeling flow. Note that permeability changes by shear reactivation would be irreversible, meaning that they would remain over the entire compliance period if not offset by mineral precipitation. The potential for such widespread fracture shear reactivation must be considered in the safety assessment, because it might impact the flow and transport of radionuclides in the bedrock. In our analysis, we did not make an estimate of the possible changes in the rock-mass permeability (mean and distribution) that such massive shear reactivation could induce. Such estimates might be difficult, but could possibly be conservatively bounded.

7 CONCLUSIONS

In this report, we have scrutinized SKB's work related to THM processes through review and independent modeling. The purpose of this modeling is not just to verify SKB's analyses of THM processes, but to identify issues that might have been overlooked, to test assumptions, and to evaluate how sensitive their results are to such assumptions. With our model analysis, we could indeed verify many of SKB's results. However, based on the review and independent modeling conducted in this report, we have also identified the following areas of weaknesses, where we believe further work and clarifications are needed:

- SKB's analysis of peak temperature may not be the most conservative one, since extreme drying of the buffer under dry conditions and unexpectedly high thermal diffusion coefficient have not been sufficiently considered. Further analysis are necessary to show that extreme drying of the buffer to below 20% could not occur or that such drying would not result in a peak temperature higher than 100°C.

- SKB's analysis of the thermal-hydrological evolution of the buffer is strongly dependent on the thermal diffusivity coefficient, which determines how much the buffer will be dried during the heating phase. The parameter appears to have been determined from laboratory experiments at different conditions (e.g., different void ratio) from the expected *in situ* conditions at emplacement. This parameter needs further verification, possibly through large-scale *in situ* tests; meanwhile, conservatively bounded estimates should be used.

- SKB's analysis of the resaturation processes suffers from a reliance on nearby hydraulic boundary conditions, which may tend to underestimate the time to full resaturation, especially when rock permeability is low. For the same reason, the impact of rock permeability on the resaturation processes may be underestimated.

- SKB's analysis of the resaturation processes does not consider the impact and uncertainties in the retention and relative permeability properties of rock, rock fractures, and interfaces—such as the interface between rock and bentonite. Moreover, the potential effect of desaturation of the rock by tunnel ventilation during operation phase is not considered. Field studies should be conducted to evaluate desaturation around tunnels and the evaluated retention and relative permeability properties of the fractured rock.

- SKB's analysis indicates that even if the rock has an extremely low permeability, and buffer would not be resaturated from the rock, the buffer would still be almost completely resaturated by water supply from the overlying backfill. This is true in the case of 30/70 backfill, but might take thousands of years. For a backfill with Friedland Clay, the initial suction in the backfill would be higher than that in the buffer, and therefore the buffer would never resaturate by water supply from the backfill. Thus, further studies or reconsideration of the backfill design may be necessary to assure buffer resaturation from the backfill in extremely dry rock conditions.

- SKB's analysis indicates that intersecting water-bearing fractures will play an important role in assuring a timely resaturation of the backfill and buffer. However, in the case of low-permeability matrix rock with one intersecting fracture, the resaturation in part of the buffer may still be slow (taking several hundred years), because the total water supply would be limited by the contact area between bentonite and water-bearing fractures. The conditions assumed in the analysis (a 5 cm thick fracture element surrounding the tunnel) is not the most conservative. Rather, the case involving water supply from a small channel within a fracture or fracture intersection should be considered.

- SKB's analysis of rock failure identifies a high potential for spalling around the deposition holes for repository alternatives at both Forsmark and Laxemar. However, a strong potential for tensile failure in the side-wall of tunnels, and its consequence for forming a continuous damaged zone along the tunnels, is not identified.

- SKB's analysis first indicated that spalling would not be a problem at the Laxemar 500 m level, and tunnels were therefore oriented without consideration of the stress field. Later, SKB found that spalling would most likely occur during the operation phase. The potential for rock failure around tunnels and deposition holes is strongly dependent on the orientation of the tunnels relative to the stress field. Therefore, the decision not to consider the stress field in the repository layout of the Laxemar alternative should be reconsidered.

- SKB's analysis of spalling and rock failure does not address the potential for time-dependent strength degradation. It might be assumed that the long-term *in situ* strength is the same as the relatively short-term *in situ* strength observed (for example) at the pillar stability experiments in Äspö. This may or may not be the case. However, this question is not addressed at all in the SR-Can.

- SKB's analysis of the likelihood for mechanically induced permeability changes in the far field does not consider the possibility of large-scale shear reactivation. Many fractures at the site might already be critically stressed for shear. However, no attempt has been made to investigate the potential correlation between water-conducting fractures and *in situ* stress regime, either at Forsmark or Laxemar, even though such a correlation has been found at Äspö. During the thermal period, shear stresses around the repository will increase. Potential permeability changes due to such shear reactivation, and its importance for radionuclide transport, needs to be evaluated.

- SKB's analysis evaluates potential far-field changes in mean permeability as a result of fracture closure during the heating phase. However, permeability will change differently in different types of fractures (e.g., clean tension fractures or filled fractures) and some fracture may shear. Thus, both mean permeability and the distribution of permeability will change, perhaps leading to more concentrated flow in fast flow paths. This possibility has not been assessed or discussed in SR-Can.

The results presented in this report and the above conclusions are based on our review and analysis related to SR-Can, but should also be considered by the SKB when defining their work scope on coupled THM processes for the upcoming SR-Site assessment. Thus, further site specific analyses of these important aspects for the performance of a Swedish deep geological repository for spent nuclear fuel should be conducted.

8 REFERENCES

Barton C A, Zoback M D and Moos D (1995) Fluid flow along potentially active faults in crystalline rock. Geology 23:683:686.

Bäckblom G., Christiansson R., and Lagerstedt L. (2004). Choise of rock excavation methods for one Swedish deep repository for spent nuclear fuel. SKB R-04-62. Swedish Nuclear Fuel and Waste Management Co, Stockholm, Sweden.

Börgesson, L., ABAQUS. In Stephansson, O., Jing, L., and Tsang, C.-F. editors, *Coupled Thermo-hydro-mechanical Processes of Fractured Media*. Developments in Geotechnical Engineering, Elsevier, 1996, 79, pp. 565–570.

Börgesson L. and Hernelind J. (1999). Coupled thermo-hydro-mechanical calculations of the water saturation phase of a KBS-3 deposition hole. Influence of hydraulic rock properties on the water saturation phase. SKB TR-99-41. Swedish Nuclear Fuel and Waste Management Co, Stockholm, Sweden.

Börgesson L., Fälth B. and Hernelind J. (2006). Water saturation phase of the buffer and backfill in the KBS-3V concept. Special emphasis given to the influence of the backfill on the wetting of the buffer. SKB TR-06-14. Swedish Nuclear Fuel and Waste Management Co, Stockholm, Sweden.

Chijimatsu M., Fujita T., Sugita Y. and Taniguchi W. (2000). Evaluation of coupled thermo-hydro-mechanical phenomena in the near field for geological disposal of high-level radioactive waste. Japan Nuclear Fuel Cycle Institute (JNC), Technical Report JNC TN8400 2000-008.

Data Report (2006). Data report for safety assessment SR-Can. SKB TR-06-25. Swedish Nuclear Fuel and Waste Management Co, Stockholm, Sweden.

Dershowitz W., Wallman O., and Kindred S. (1991). Discrete fracture modeling for the Stripa site characterization and validation drift inflow predictions. Stripa Project Technical Report 91-16. Swedish Nuclear Fuel and Waste Management Co, Stockholm, Sweden.

Ferrill D, Winterle J, Wittmeyer G, Sims D, Colton S and Armstrong A (1999) Stressed rock strains groundwater at Yucca Mountain, Nevada. GSA Today, Geological Society of America, May 1999.

Finsterle S. and Pruess K. (1995). Solving the estimation-identification problem in two-phase flow modeling. Water Resources Research, 31. pp. 913-924.

Hökmark H. and Fälth B. (2003). Thermal dimensioning of the deep repository. Influence of canister spacing, canister power, rock thermal properties and near-field design on the maximum canister surface temperature. SKB TR-03-09. Swedish Nuclear Fuel and Waste Management Co, Stockholm, Sweden.

Hökmark H., Fälth B. and Wallroth T. (2006). T-H-M couplings in rock. Overview of importance to the SR-Can assessment. SKB R-06-88. Swedish Nuclear Fuel and Waste Management Co, Stockholm, Sweden.

Itasca (2003). 3DEC – 3-Dimensional Distinct Element Code, User's Guide. Itasca Consulting Group Inc. Minneapolis, USA.

Jaeger, J. C. and Cook, N. G. W. (1979), *Fundamentals of Rock Mechanics.* Chapman and Hall, London.

Liu H.H., Rutqvist J., Zhou G. and Bodvarsson G.S. (2004). Upscaling of normal stress-permeability relationship for fracture network obeying the fractional levy motion. In: Stephansson O, Hudson JA, Jing L, editors. Coupled T-H-M-C Processes in Geo-Systems: Fundamentals, Modelling, Experiments and Applications. Elsevier Geo-Engineering Book Series, Oxford, pp. 263–268.

Makurat A, Barton N and Rad N S (1990) Joint conductivity variation due to normal and shear deformation. In: Barton N and Stephansson (eds) Rock Joints pp 535-540

Martin D. (2005). Preliminary assessment of potential underground stability (wedge and spalling) at Forsmark, Simpevarp and Laxemar sites. SKB report R-05-71. Swedish Nuclear Fuel and Waste Management Co, Stockholm, Sweden.

Min KB, Rutqvist J., Tsang C.-F., and Jing L. (2004). Stress-dependent permeability of fracture rock masses: a numerical study. *Int. J. Rock mech. & Min. Sci,* **41,** 1191-1210.

Olivella S, Gens A, Carrera J, Alonso EE. (1995). Numerical formulation for a simulator (CODE_BRIGHT) for the coupled analysis of saline media. Engineering Computations, 13:87–112.

Olivella, S. and Gens, A. (2000) Water phase change and vapour transport in low permeability unsaturated soil with capillary effects. In review for publication in *Transport in Porous Media*, 40, pp. 219-241.

Rutqvist J, Tsang C-F, Ekman D and Stephansson O (1997) Evaluation of in situ hydromechanical properties of rock fractures at Laxemar in Sweden. In Proc 1st Asian Rock Mechanics Symposium ARMS 97, Seoul, Korea, pp. 619-624

Rutqvist J., Börgesson L., Chijimatsu M., Kobayashi A., Nguyen T. S., Jing L., Noorishad J., and Tsang C.-F. (2001). Thermohydromechanics of Partially Saturated Geological Media – Governing Equations and Formulation of Four Finite Element Models. *Int. J. Rock mech. Min. Sci.* 38, 105-127.

Rutqvist J, Wu Y-S, Tsang C-F and Bodvarsson G (2002) A modeling approach for analysis of coupled multiphase fluid flow, heat transfer, and deformation in fractured porous rock. Int. J. Rock Mech. Min. Sci. 39:429-442

Rutqvist J. and Stephansson O. (2003). The role of hydromechanical coupling in fractured rock engineering. Hydrogeology Journal 11, p. 7–40.

SKB (2005). Preliminary site description Forsmark area – version 1.2. SKB R-05-18. Swedish Nuclear Fuel and Waste Management Co, Stockholm, Sweden.

SKB (2006a). Long-term safety for KBS-3 repository at Forsmark and Laxemar – a first evaluation. Main report of the SR-Can project. SKB TR-06-09. Swedish Nuclear Fuel and Waste Management Co, Stockholm, Sweden.

SKB (2006b). Preliminary site description Laxemar area – version 1.2. SKB R-06-10. Swedish Nuclear Fuel and Waste Management Co, Stockholm, Sweden.

Talbot C.J. and Sirat M. (2001) Stress control of hydraulic conductivity in fractured-saturated Swedish bedrock. Engineering Geology 61:145-153.

Vargaftik N.B. Tables of the thermophysical properties of liquids and gases. John Wiley and Sonce, New York (1975).

Wladis D., Jönsson P. and Wallroth T. (1997) Regional characterization of hydraulic properties or rock using well test data. SKB TR 97-29. Swedish Nuclear Fuel and Waste Management Company, Stockholm, Sweden.

APPENDIX A: DESCRIPTION OF THE ROCMAS CODE

A1 THE ROCMAS CODE

ROCMAS is a finite element program developed at LBNL for analysis of coupled thermo-hydro-mechanical (THM) processes in partially saturated geological media (Noorishad and Tsang, 1996, Rutqvist *et al.*, 2001). It is continuum based, capable of modeling porous soil and ubiquitously fractured rock, with an option for representing discrete fractures.

A1.1 Basic approach and assumptions

In ROCMAS, the formulation of coupled thermohydroelasticity in terms of Biot's theory of consolidation (Biot, 1941) is extended to partially saturated media through Philip and de Vries' (1957) theory for heat and moisture flow in soil. In this theory, three phases (solid, liquid, and gas) are present. However, it is assumed that the gas pressure P_g is constant and equal to atmospheric pressure throughout the porous medium. As a consequence, vapor transport occurs only through molecular diffusion driven by a gradient in vapor concentration (density), while advection of vapor with bulk gas flow is neglected. The vapor density in the medium is governed by Kelvin's relation, assuming thermodynamic equilibrium for pore liquid in contact with its vapor, and phase transitions occur as evaporation-condensation processes. During heat transfer, coexisting fluid and solid components are assumed to be in local thermal equilibrium (i.e., locally they are at the same temperature). The mechanical behavior of the porous media consists of the gas, liquid and solid-matter responses to local pressure and the overall material (skeleton) response to effective stresses. Fractures are treated as a "porous medium" separate from the rock matrix and would be discretely defined by special fracture elements in a finite-element mesh. Therefore, the basic balance equations are the same for rock matrix and fracture materials, while some of the constitutive relations differ. With this approach and these assumptions, three balance equations—water mass balance, energy conservation and linear momentum balance—and a number of constitutive relations are required for a full description of the THM state. These equations are derived and presented in details below.

A1.2 General Balance Equations

The water mass-balance equation for the coupled hydraulic and mechanical system is obtained by combining water mass balance equations (for water vapor and liquid water) with the solid mass-balance equation. Considering the grain compressibility, but neglecting a few small terms related to the grain density changes caused by internal fluid pressure and temperature, the following coupled water mass-balance equation is derived (Rutqvist et al., 2001a):

$$\phi \frac{\partial}{\partial t}\left(S_l \rho_l + S_g \rho_v\right) + \left(S_l \rho_l + S_g \rho_v\right)\alpha \frac{\partial \varepsilon_v}{\partial t} = -\nabla \cdot \left(\mathbf{q}_{rl} + \mathbf{q}_{rv}\right) \qquad \text{(A-1)}$$

where ϕ is porosity, S_l and S_g are liquid and gas saturation, ρ_l and ρ_v are liquid water and vapor densities, α is Biot's effective stress parameter, ε_v is volumetric strain, and $\mathbf{q}_{rl}$ and $\mathbf{q}_{rv}$ are flux densities for liquid and vapor flow.

Assembling the contributions to energy storage and heat flow over all phases results in the following form of the energy conservation equation (Rutqvist et al., 2001a)

$$\frac{\partial}{\partial t}\left[(1-\phi)\rho_s h_s + \phi\left(h_l S_l \rho_l + h_v S_g \rho_v\right)\right] = -\nabla \cdot \left(\mathbf{i}_m^h + h_l \mathbf{q}_{rl} + h_v \mathbf{q}_{rv}\right) \quad \text{(A-2)}$$

where the storage content in the gas phase is dominated by the vapor, and mechanical energy conversion is neglected. In Equation (A-2) h_s, h_l, *and* h_v are specific enthalpies (per unit mass of the phase), and $\mathbf{i}_m^h$ is the apparent heat conduction over all phases.

The final balance equation is the law of conservation of linear momentum, which in the absence of an inertia term reduces to the static stress equilibrium for macroscopic total stresses:

$$\nabla \cdot \boldsymbol{\sigma} + \rho_m \mathbf{g} = 0 \quad \text{(A-3)}$$

where σ is the total stress tensor, $\mathbf{g}$ is a vector for the acceleration resulting from gravity, and ρ_m is the average density of the mixture:

$$\rho_m = (1-\phi)\rho_s + \phi S_l \rho_l + \phi S_g \rho_g \quad \text{(A-4)}$$

Hence, neglecting the air mass balance, Equations (A-1) to (A-3) are the basic balance equations in ROCMAS.

A1.3 Constitutive equations and constraints

Neglecting the effects of osmotic suction and adsorbed liquid water, the liquid saturation S_l is assumed to be a function of capillary pressure P_c and temperature, and the following relations apply:

$$S_l = S_l(P_c, T) \quad \text{(A-5)}$$

$$P_c = P_g - P_l \quad \text{(A-6)}$$

$$S_g = 1 - S_l \quad \text{(A-7)}$$

where P_l is liquid water pressure, P_g is total gas pressure, and S_g is gas saturation. With the assumption of atmospheric gas pressure (and thus $P_l \approx -P_c$), the liquid water and vapor flux is obtained as:

$$\mathbf{q}_{rl} = -\rho_l \frac{\mathbf{k} k_{rl}}{\mu_l}\left(\nabla P_l - \rho_l g \nabla z\right) \quad \text{(A-8)}$$

and

$$\mathbf{q}_{rv} = -D_v \mathbf{I} \nabla \rho_v \quad \text{(A-9)}$$

which has been derived assuming that ρ_g is constant. Assuming a local thermodynamic equilibrium between liquid water and its vapor, the vapor density can be obtained through Kelvin's relationship for relative humidity, r_H, of the moist air in a porous media (Bear and Bachmat, 1991) as

$$\rho_v = \rho_{vS}(T) RH = \rho_{vS} \exp\left(\frac{P_l}{\rho_l R_v T}\right) \quad \text{(A-10)}$$

where ρ_{vS} is the temperature-dependent saturated vapor density and R_v is the specific gas constant for water vapor. The vapor gradient in Equation (A-9) is further expanded using Equation (A-10), leading to the following expression for the vapor flux:

$$\mathbf{q}_{rv} = -\rho_l \left(D_{Pv} \mathbf{I} \nabla P_l + D_{Tv} \mathbf{I} \nabla T \right) \tag{A-11}$$

where

$$D_{Pv} = \frac{D_v \rho_v}{\rho_l^2 R_v T} \tag{A-12}$$

is the isothermal vapor diffusivity, and

$$D_{Tv} = f_{Tv} D_v \left(\frac{RH}{\rho_l} \frac{\partial \rho_{vS}}{\partial t} - \frac{\rho_v P_l}{\rho_l^2 R_v T^2} \right) \tag{A-13}$$

is the thermal vapor diffusivity.

All the parameters in Equations (A-12) and (A-13) are known from other constitutive relations except for f_{Tv}, a thermal diffusion enhancement factor (Philip and de Vries, 1957), and the effective molecular diffusion coefficient, D_v, which should be experimentally determined. The effective molecular diffusion coefficient is calculated using an empirical relation for molecular diffusion of water vapor and reduction factors taking into account the porous media properties, using the following expression:

$$D_v = \tau S_g \phi 2.16 \times 10^{-5} \left(T_{abs} / 273.15 \right)^{1.8} \tag{A-14}$$

where τ is a tortuosity factor.

The permeability of a porous soil depends on its porosity and an empirical relative-permeability function as

$$\mathbf{k} = \mathbf{k}(\phi) \cdot k_r(S_l) \tag{A-15}$$

where $\mathbf{k}(\phi)$ is the hydraulic permeability tensor of the porous media (in soil literature denoted as *intrinsic permeability*) and k_r is the relative-permeability function for liquid and flow. For a fractured rock, the hydraulic permeability may be dominated flow in the fracture system and related to stress or strain, rather than porosity, thus

$$\mathbf{k}(\phi) = \mathbf{k}(\boldsymbol{\sigma}', \boldsymbol{\varepsilon}) \tag{A-16}$$

Heat conduction is governed by Fourier's law, which is written as

$$\mathbf{i}_m^h = -\lambda_m \mathbf{I} \nabla T \tag{A-17}$$

where λ_m is the apparent macroscopic thermal conductivity over all phases, which in a porous material may be strongly dependent on liquid water content.

The thermal properties of the porous media in the formulation of ROCMAS are derived based on the work by de Vries (1958). The specific enthalpies in Equation (A-2) is expressed in terms of specific heat and temperature as:

$$h_s + h_l = C_S \left(T - T_0 \right) + C_l \left(T - T_0 \right) \tag{A-18}$$

$$h_v = h_{Pv} + h_{L0} = C_{Pv} (T - T_0) + L_0 (T_0) = C_{Pl} \left(T - T_0 \right) + L(T) \tag{A-19}$$

where L_0 is the latent heat of vaporization of liquid water at T_0.

The total energy flux in Equation (A-2) is then written as:

$$\mathbf{q}_h = -\lambda \mathbf{I} \nabla T + C_{Pl} (T - T_0) \mathbf{q}_{rl} + \left[C_{Pl} \left(T - T_0 \right) + L(T) \right] \mathbf{q}_{rv} \tag{A-20}$$

where the first term represents pure conduction, and the second and third terms are enthalpy transport by liquid and vapor flow, respectively. Following de Vries (1958, 1987), we substitute Equation (A-11) into Equation (A-20) to derive the following expression:

$$\mathbf{q}_h = -\left(\lambda + \rho_l L D_{Tv}\right)\mathbf{I}\nabla T - \rho_l L D_{Pv}\mathbf{I}\nabla P + C_{pl}\left(\mathbf{q}_{rl} + \mathbf{q}_{rv}\right)\left(T - T_0\right) \qquad \text{(A-21)}$$

In practice, the conductivity of the porous media may be experimentally determined as a function of saturation, including the effects of pure conduction and latent heat transport under thermal gradient:

$$\lambda + \rho_l L D_{Tv} = \lambda_m(S_l) \qquad \text{(A-22)}$$

With the basic assumption of small strain, the total strain tensor, $\boldsymbol{\varepsilon}$, and volumetric strain, ε_V, is defined as usual:

$$\boldsymbol{\varepsilon} = \frac{1}{2}\left(\nabla\mathbf{u} + \left(\nabla\mathbf{u}\right)^{\mathbf{tr}}\right) \qquad \text{and} \qquad \varepsilon_v = \nabla\cdot\mathbf{u} \qquad \text{(A-23)}$$

where $\mathbf{u}$ is the displacement vector and tr denotes the transpose of the tensor.

A modified effective stress law effective stress law can be derived in terms of Biot's parameters as:

$$\mathrm{d}\,\boldsymbol{\sigma} = \mathrm{d}\,\boldsymbol{\sigma}' - \alpha\mathbf{I}S_l\,\mathrm{d}\,P \qquad \text{(A-24)}$$

where the average pore pressure is calculated using the volume average of each phase and assuming a negligible gas pressure. The mechanical constitutive behavior is expressed as

$$\mathrm{d}\,\boldsymbol{\sigma} = \mathbf{D} : \left(\mathrm{d}\,\boldsymbol{\varepsilon} - \mathrm{d}\,\boldsymbol{\varepsilon}_T - \mathrm{d}\,\boldsymbol{\varepsilon}_{sw}\right) = \mathbf{D} : \left(\mathrm{d}\,\boldsymbol{\varepsilon} - \mathbf{I}\beta_T dT - \mathbf{I}\beta_{sw}\,\mathrm{d}\,S_l\right) \qquad \text{(A-25)}$$

where $\mathbf{D}$ is the tangential stiffness matrix, $\boldsymbol{\varepsilon}$, $\boldsymbol{\varepsilon}_T$, $\boldsymbol{\varepsilon}_{\mathrm{sw}}$ are tensors of total, thermal, and swelling strains, respectively.

A1.4 Field equations and solution approach

The final field equations are derived by substituting the flux terms and stress terms in Equations (A-8), (A-11), (A-21), and (A-24), and the basic balance equations [Equations (A-1), (A-2) and (A-3)], and expanding the storage terms in terms of primary variables. The three following governing equations—expressed in terms of strain, ε, fluid pressure, P, and temperature, T—are obtained:

$$C_{Pe}\frac{\partial\varepsilon_V}{\partial t} + C_{PP}\frac{\partial P}{\partial t} + C_{PT}\frac{\partial T}{\partial t} + \nabla\cdot\left(\mathbf{K}_{\mathbf{PP}}\nabla P\right) + \nabla\cdot\left(\mathbf{K}_{\mathbf{PT}}\nabla T\right) = J_P \qquad \text{(A-26)}$$

$$C_{TP}\frac{\partial P_l}{\partial t} + C_{TT}\frac{\partial T}{\partial t} + \nabla\cdot\left(\mathbf{K}_{\mathbf{Tp}}\nabla P\right) + \nabla\cdot\left(\mathbf{K}_{\mathbf{TT}}\nabla T\right) + \mathbf{V}_{\mathbf{TT}}\cdot\nabla T + J_T \qquad \text{(A-27)}$$

$$\nabla\cdot\left(\mathbf{C}_{\mathbf{ee}}\frac{\partial\boldsymbol{\varepsilon}}{\partial t}\right) + \nabla\cdot\left(\mathbf{C}_{\mathbf{eP}}\frac{\partial P}{\partial t}\right) + \nabla\cdot\left(\mathbf{C}_{\mathbf{eT}}\frac{\partial T}{\partial t}\right) = J_e \qquad \text{(A-28)}$$

which are the fluid flow, heat transfer, and force balance equations, respectively.

The final governing equations [Equations (A-26) to (A-28)] are discretized using a standard Galerkin finite element solution approach to obtain a set of matrix equations as

$$\begin{bmatrix} \mathbf{0} & \mathbf{0} & \mathbf{0} \\ \mathbf{0} & \overline{\mathbf{K}}_{\mathbf{PP}} & \overline{\mathbf{K}}_{\mathbf{PT}} \\ \mathbf{0} & \overline{\mathbf{K}}_{\mathbf{TP}} & \overline{\mathbf{K}}_{\mathbf{TT}} \end{bmatrix} \begin{Bmatrix} \overline{\mathbf{u}} \\ \overline{\mathbf{P}} \\ \overline{\mathbf{T}} \end{Bmatrix} + \begin{bmatrix} \overline{\mathbf{C}}_{\mathbf{uu}} & \overline{\mathbf{C}}_{\mathbf{uP}} & \overline{\mathbf{C}}_{\mathbf{uT}} \\ \overline{\mathbf{C}}_{\mathbf{Pu}} & \overline{\mathbf{C}}_{\mathbf{PP}} & \overline{\mathbf{C}}_{\mathbf{PT}} \\ \mathbf{0} & \overline{\mathbf{C}}_{\mathbf{TP}} & \overline{\mathbf{C}}_{\mathbf{TT}} \end{bmatrix} \frac{\partial}{\partial t} \begin{Bmatrix} \overline{\mathbf{u}} \\ \overline{\mathbf{P}} \\ \overline{\mathbf{T}} \end{Bmatrix} = \begin{Bmatrix} \overline{\mathbf{J}}_{\mathbf{u}} \\ \overline{\mathbf{J}}_{\mathbf{P}} \\ \overline{\mathbf{J}}_{\mathbf{T}} \end{Bmatrix} \qquad \text{(A-29)}$$

where coefficient matrices, $\overline{\mathbf{K}}_{\mathbf{PP}}$ etc, contains appropriate finite-element shape functions and transformation matrices (see Noorishad and Tsang (1996)), and $\overline{\mathbf{u}}$, $\overline{\mathbf{P}}$, and $\overline{\mathbf{T}}$ are nodal parameters.

The discrete equations are integrated in time from t to t + Δt, using a finite difference scheme. However, because many practical problems have a large time-constant difference between the fluid-flow equation and the heat equation, we use an interlaced solution approach. In this method, the hydromechanical equations are first solved directly and thereafter the heat equation is solved for an appropriate time step. After time integration, the Jacobian is derived in a Newton-Raphson or modified Newton-Raphson formulation, and the linearized equations are solved with a direct solver.

A2 REFERENCES

Bear, J. and Bachmat, Y., *Introduction to Modeling of Transport Phenomena in Porous Media*. p. 553. Kluwer Academic Publisher, Netherlands (1999).

Bernabe Y. The effective pressure law for permeability in Chelmford granite and Barre granite. Int J Rock Mech Min Sci & Geomech Abstr 23:267-275 (1986).

Brace W F, Walsh J B and Frangos W T. Permeability of granite under high pressure. J Geophys Res 73:2225-2236 (1968).

Biot, M.A., General theory of three dimensional consolidation. *J. Applied Physics*, 12, 155–164 (1941).

Chijumatsu M., Fujita T., Sugita Y. and Ishikawa H. Coupled thermo-hydro-mechanical experiment at Kamaishi mine. Laboratory rock property tests. Power reactor and nuclear fuel development corporation (PNC). TN8410 96-060 (1996).

de Vries, D.A, Simultaneous transfer of heat and moisture in porous media. *Trans. Am. Geophys. Un*. 39, 909–916 (1958).

de Vries, D.A., The theory of heat and moisture transfer in porous media revisited. *Int. J. Heat. Mass. Tranfer.* 30, 1343–1350 (1987).

Fujita T., Sugita Y., Chijimatsu M. and Ishikawa H. Coupled thermo-hydro-mechanical experiment at Kamaishi mine. Mechanical properties of fracture. Power reactor and nuclear fuel development corporation (PNC). TN8410 96-059 (1996).

Fujita T., Chijimatsu M., Ishikawa H., Suzuki H. and Matsumoto K. Coupled thermo-hydro-mechanical experiment at Kamaishi mine. Fundamental properties of bentonite

OT-9607. Power reactor and nuclear fuel development corporation (PNC). TN8410 97-071 (1997).

Hoek E and Brown E. T. Practical estimates of rock mass strength. *Int. J. Rock mech. Min. Sci.* 34, 1165-1186 (1997).

JNC. H12: Project to Establish the Scientific and Technical Basis for HLW Disposal in Japan. Second progress report on research and development for the geological disposal of HLW in Japan. Five volumes. Japan Nuclear Cycle Development Institute. (2000).

Noorishad, J., and Tsang, C.-F., ROCMAS-simulator: A Thermohydromechanical Computer Code. In Stephansson, O., Jing, L., and Tsang, C.-F. editors. *Coupled Thermo-hydro-mechanical Processes of Fractured Media*. Developments in Geotechnical Engineering, Elsevier. 79, pp. 551–558 (1996).

Philip J.R. and de Vries D.A. Moisture movement in porous material under temperature gradients. EOS Trans., AGU, 38(2) 222-232 (1957).

Rutqvist J., Noorishad J. and Tsang C.-F. Coupled Analysis of a Thermohydromechanical Experiment in Rock at Kamaishi Mine-Final Report. Swedish Nuclear Power Inspectorate (SKI) Technical Report 99:50. Also a Lawrence Berkeley National Laboratory Technical Report, LBNL-44203. p. 103, (1999).

Rutqvist J., Börgesson L., Chijimatsu M., Kobayashi A., Nguyen T. S., Jing L., Noorishad J., and Tsang C.-F. Thermohydromechanics of Partially Saturated Geological Media – Governing Equations and Formulation of Four Finite Element Models. *Int. J. Rock mech. Min. Sci.* 38, 105-127 (2001).

APPENDIX B: VALIDATION AND CALIBRATION OF THE BENTONITE MODEL AGAINST LABORATORY EXPERIMENTS ON MX-80 BENTONITE

B1 INTRODUCTION

This appendix presents calibration and validation of the ROCMAS bentonite model against laboratory experiments on MX-80 bentonite samples. The ROCMAS code, including its setup for THM analysis of bentonite, is presented in Rutqvist et al. (2001) and in Appendix A of this report. In this appendix, we first present validation of the bentonite properties used by SKB and in some cases derive improved THM properties by model calibration against results of laboratory experiments.

B2 BENTONITE PROPERTIES USED BY SKB

Many of the bentonite properties used by SKB were originally developed and presented in Börgesson and Hernelind (1999). Most of those properties were derived for a bentonite buffer that will be conditioned at a void ratio e = 0.77, having a dry-density of 1570 kg/m^3, and with an initial liquid saturation $S_l = 0.66$.

The water-retention curve of the bentonite follows a modified van-Genuchten function that was fitted to data of MX-80 bentonite from Börgesson and Hernelind (1999) (see Figure B-1). The following equation provided a reasonable match to the experimental data:

$$S_l = 0.01 + (0.99)\left[1 + \left(s/18\cdot 10^6\right)^{1.5}\right]^{-0.333}\left[1 - s/400\cdot 10^6\right]^{1.5} \quad \text{(B-1)}$$

where s is suction (= - P_c in this model).

The permeability of MX-80 depends on its porosity and an empirical relative-permeability function as

$$\mathbf{k} = \mathbf{k}(\phi)\cdot k_r(S_l) \quad \text{(B-2)}$$

where $\mathbf{k}(\phi)$ is the hydraulic permeability tensor of the porous media (in soil literature denoted as *intrinsic permeability*) and k_r is the relative-permeability function for liquid and flow. From Börgesson and Hernelind (1999) we first adopted

$$\mathbf{k}_r = S^3 \quad \text{(B-3)}$$

In ROCMAS, the vapor flux is calculated according to the following expression:

$$\mathbf{q}_{rv} = -\rho_l\left(D_{Pv}\mathbf{I}\nabla P_l + D_{Tv}\mathbf{I}\nabla T\right) \quad \text{(B-4)}$$

where

$$D_{Pv} = \frac{D_v\rho_v}{\rho_l^2 R_v T} \quad \text{(B-5)}$$

is the isothermal vapor diffusivity, and

$$D_{Tv} = f_{Tv}D_v\left(\frac{RH}{\rho_l}\frac{\partial\rho_{vS}}{\partial t} - \frac{\rho_v P_l}{\rho_l^2 R_v T^2}\right) \quad \text{(B-6)}$$

is the thermal vapor diffusivity.

All the parameters in Equations (B-5) and (B-6) are known from other constitutive relations except for f_{Tv}, a thermal diffusion enhancement factor (Philip and de Vries, 1957), and the effective molecular diffusion coefficient, D_v, which should be experimentally determined. The effective molecular diffusion coefficient is calculated using an empirical relation for molecular diffusion of water vapor and reduction factors taking into account the porous media properties, using the following expression:

$$D_v = \tau S_g \phi 2.16 \times 10^{-5} \left(T_{abs}/273.15\right)^{1.8} \tag{B-7}$$

where τ is a tortuosity factor.

However, SKB do not use Equation (B-6) and (B-7), to calculate thermal diffusion, but rather an empirical function developed by Börgesson and Hernelind (1999) is used for the thermal vapor diffusion coefficient of the bentonite:

$$D_{Tv} = 0.7 \cdot 10^{-11} \qquad \text{for } 0.3 < S_l < 0.7 \tag{B-8a}$$

$$D_{Tv} = 0.7 \cdot 10^{-11} \cos^6\left(\frac{S_l - 0.7}{0.3}\frac{\pi}{2}\right) \qquad \text{for } S_l < 0.7 \tag{B-8b}$$

$$D_{Tv} = 0.7 \cdot 10^{-11} \sin^6\left(\frac{S_l}{0.3}\frac{\pi}{2}\right) \qquad \text{for } S_l > 0.3 \tag{B-8c}$$

This function was developed and back-calculated by Börgesson and Hernelind (1999) by model simulations of vapor flow experiments under thermal gradient.

In ROCMAS, the mechanical constitutive behavior is expressed as

$$\mathrm{d}\boldsymbol{\sigma} = \mathbf{D} : \left(\mathrm{d}\boldsymbol{\varepsilon} - \mathrm{d}\boldsymbol{\varepsilon}_T - \mathrm{d}\boldsymbol{\varepsilon}_{sw}\right) = \mathbf{D} : \left(\mathrm{d}\boldsymbol{\varepsilon} - \mathbf{I}\beta_T dT - \mathbf{I}\beta_{sw}\,\mathrm{d}S_l\right) \tag{B-9}$$

where $\mathbf{D}$ is the tangential stiffness matrix, and $\boldsymbol{\varepsilon}$, $\boldsymbol{\varepsilon}_T$, $\boldsymbol{\varepsilon}_{sw}$ are tensors of total, thermal, and swelling strains, respectively.

For analysis of SR-Can, a simplified linear swelling model is used to represent swelling and development of swelling stress in the bentonite buffer. In this model, the swelling stress is calculated as:

$$\Delta\sigma' = 3K\beta_{sw}\Delta S_l \tag{B-10}$$

To determine the change in stress for a given change in saturation, we need to know the bulk modulus, K, and moisture swelling coefficient β_{sw}. We estimated these two parameters from experimental data for MX-80, presented in Börgesson and Hernelind (1990). First a moisture swelling coefficient of $\beta_{sw} \approx 0.4$ was determined by fitting to data from unconfined drying shrinkage test. Moreover, experimental data in Börgesson and Hernelind (1999) indicates a swelling stress of 6 to 8 MPa when a sample is wetted to full saturation from an initial saturation of 61%. With a target swelling stress of 8 MPa, a representative "average" bulk modulus for this linear model is calculated using Equation (B-10) as:

$$K = \frac{1}{3}\frac{\Delta\sigma'_m}{\Delta S_l}\frac{1}{\beta_{SW}} = \frac{1}{3}\frac{8\cdot 10^6}{0.39}\frac{1}{0.4} \approx 17 MPa \tag{B-11}$$

The approach of modeling swelling can be considered a rational engineering approach to simulate the evolution of swelling stress and strain during the resaturation of the buffer.

The thermal conductivity of the bentonite is saturation dependent and the following function was fitted to experimental data in Börgesson and Hernelind (1999):

$$\lambda = 0.3 \qquad \text{for } S_l < 0.25 \qquad \text{(B-12a)}$$

$$\lambda = 0.3 + (S_l - 0.25) * 1.8 \qquad \text{for } S_l > 0.25 \text{ and } S_l < 0.8 \qquad \text{(B-12b)}$$

$$\lambda = 1.3 \qquad \text{for } S_l > 0.8 \qquad \text{(B-12c)}$$

Some of the bentonite properties presented above have been determined directly from laboratory measurements, whereas others have been determined by numerical back-analyses of laboratory tests. The ones determined by back-analysis might be dependent on the numerical model and model approach used. Therefore, it is important to run the same experiments using the ROCMAS code.

B3 MODELING OF SMALL-SCALE LABORATORY TESTS

This section presents modeling of small-scale laboratory tests with experimental data from Börgesson and Hernelind (1999).

B3.1 Water uptake test

The water uptake tests can be used to validate and back-calculate the relative-permeability function, for a given (independently determined) water-retention curve. Figure B-2 presents the modeling results of two different infiltration tests, at different initial void ratio and initial saturation using experimental results from Börgesson and Hernelind (1999). The results indicate that the relative-permeability function defined in Equation (B-3) is reasonably accurate, although an exponent equal to 4 might give a better match than an exponent of 3.

B3.2 Thermal gradient tests

The thermal gradient test (Börgesson and Hernelind, 1999) can be used to back-calculate the thermal vapor diffusion parameters. First the test was simulated with the SKB's parameters given in Section B2. The results in Figure B-3a indicate that the modeling do not match the experimental results at the hot end (drying part) but does somewhat better on the wetting part. An alternative simulation with D_{tv0} increased from 0.7×10^{-11} $m^2/s,K$ to 1.5×10^{-11} $m^2/s,K$ matches the hot end (drying part) very well, but overestimates the final (steady state) wetting at the hot end.

As an alternative test, we try to use the original ROCMAS approach for modeling of thermal diffusion, where D_{TV} is determined through Equations (B-6) and (B-7). The results in Figure A-4 indicate a reasonably match to measured responses.

B3.3 Swelling pressure test

Experimental data in Börgesson and Hernelind (1999) indicates a swelling stress of 6 to 8 MPa when a sample is wetted to full saturation from an initial saturation of 61%. This is for a sample with initial void ratio of 0.77. As described above, a moisture swelling coefficient of $\beta_{sw} \approx 0.4$ was determined by fitting to data from an unconfined drying shrinkage test. Moreover, a bulk modulus of about 17 MPa was back-

calculated for a target swelling pressure of about 8 MPa. Figure B-5 shows a numerical simulation of a swelling pressure test measured for the water uptake in a confined test chamber. The simulation was conducted for an initial saturation of about 61%. The swelling pressure reaches about 7 MPa, after about 3 months of infiltration.

B4 MODELING OF CEA MOCK-UP TEST

This section presents modeling of two THM mock-up tests that have been performed on vertical cylindrical columns of compacted MX-80 bentonite by the Atomic Energy Company (CEA) in France (Figure B-6).

B4.1 Experimental setup

Two different initial water contents were used to form the samples. Each test was composed of two phases. In Phase 1, heat was applied to one end of the column while the temperature at the other end was kept constant at 20ºC. A maximum temperature of 150ºC was applied. Phase 2 started after thermal equilibrium had been achieved and involved the gradual hydration of the sample. A constant water pressure was applied to the end opposite to the one where the temperature variation was prescribed. Constant volume conditions were ensured in the two phases of the test.

The following parameters were measured during the tests:

- Temperatures
- Relative humidity
- Pore pressure
- Total axial stress
- Total radial stress

Samples had a diameter and a height of 203 mm. The samples were tightly enclosed in a PTFE sleeve. To minimize heat losses, the cells were insulated with a heat-proof envelope. Experiments were not gas tight. Heat was applied at the bottom plate, whereas hydration proceeds from the top of the sample.

B4.2 Bentonite properties

The dry density of MX-80 in the mock-up test is different from that of the small scale laboratory tests presented in Section B3. The dry density of MX-80 in the SKB laboratory tests is 1.67 g/cm^3, whereas in the mock-up test it is approximately 1.8 g/m^3. The void ratio for the mock-up test is about 0.6 compared to 0.77 for the previous laboratory tests. The mock-up test may not be accurately simulated with the water-retention curve defined in Equation (B-1). Relative humidity would be completely different for a given saturation level. Therefore, we adopt a water-retention curve matched to data derived for the relevant void ratio. A reasonable match to the data could be obtained using a standard van Genuchten function, with P_0 = 40 MPa, and β = 1.67. Moreover, the denser bentonite will have a higher swelling pressure and a lower intrinsic permeability. For a void ratio of 0.6, the swelling pressure could be estimated to be about 20 to 25 MPa and permeability around 2 to 4×10^{-21} m^2. The increased swelling pressure can be simulated in the current ROCMAS model by increasing the β_{sw} from 0.4 to 0.8.

Another property that might be affected is the thermal vapor diffusion coefficient, D_{TV}. However, in comparing the simulated results using D_{TV} based on Equation (B-12) to those from using Equations (B-6) and (B-7), we found that Equation (B-12)

could not reproduce the measured evolution in the mock-up test. Equations (B-6) and (B-7), on the other hand, gives a reasonable good agreement in moisture evolution for the mock-up test.

Figure B-7 presents the simulated evolution of temperature, relative humidity, and axial stress, for Cell 1 and 2. The simulation was conducted in a simplified model that did not include the axisymmetric geometry of the test, but was merely a vertical column of elements. The difference in Cell 1 and Cell 2 experiments is that Cell 2 starts at an initially higher initial saturation. The relative humidity is calculated using:

$$RH = \exp\left(\frac{P_l}{\rho_l R_v T}\right) \tag{B-13}$$

where R_v is the specific gas constant for water vapor.

The measured data presented in Gatabin and Billaud (2005) are rather scattered, except for the temperature data. Therefore, we cannot match the measured data at every point. However, a comparison of the simulated and measured data shows that the model matches the experiments quite well in general terms as follows:

- The temperature for both Cell 1 and Cell 2 is very well matched and stays approximately constant during Phase 2 in both experiments and simulations.
- The general evolution of saturation agrees quite well for both Cell 1 and 2. Experiments and simulation shows similar general behavior with a drying to about 30 and 40% during Phase 1 for Cell 1 and 2, respectively, and then a gradual wetting during Phase 2. The rate of gradual wetting during Phase 2 is controlled by permeability.
- The general evolution and magnitude of axial stress is in general agreement between modeling and experiments, with a maximum stress of about 10 and 6 MPa, for Cell 1 and 2, respectively.

In Cell 2, the experiments indicated a steady saturation for phase 2 rather than a gradual in increase. This can be reproduced in the modeling by lowering the bentonite's permeability slightly. In this case, we used 4×10^{-21} m^2.

B5 SUMMARY AND CONCLUSIONS

This appendix presents calibration and validation of the ROCMAS bentonite model against laboratory experiments on MX-80 bentonite samples. Generally good agreements were obtained for all tests. Based on this analysis, it appears that the thermal diffusivity according to the original ROCMAS setup based on Equations (B-6) and (B-7) is preferable, since this setup produced a good match to experimental data for both small scale laboratory tests and the mock-up tests. Alternatively, the thermal diffusivity defined according to Equation B-8 could be used, provided that upper and lower bounds are used to match either the drying or wetting parts in the experiments.

B6 REFERENCES

Börgesson L. and Hernelind J. Coupled thermo-hydro-mechanical calculations of the water saturation phase of a KBS-3 deposition hole. Swedish Nuclear Fuel and Waste Management Co. Technical Report TR-99-41. (1999).

Philip J.R. and de Vries D.A. Moisture movement in porous material under temperature gradients. EOS Trans., AGU, 38(2) 222-232 (1957).

Gatabin C., and Billaud P. Bentonite THM mock-up experiments. Sensors data report. CEA, France. (2005).

Rutqvist J., Börgesson L., Chijimatsu M., Kobayashi A., Nguyen T. S., Jing L., Noorishad J., and Tsang C.-F. Thermohydromechanics of Partially Saturated Geological Media – Governing Equations and Formulation of Four Finite Element Models. *Int. J. Rock mech. Min. Sci.* 38, 105-127 (2001).

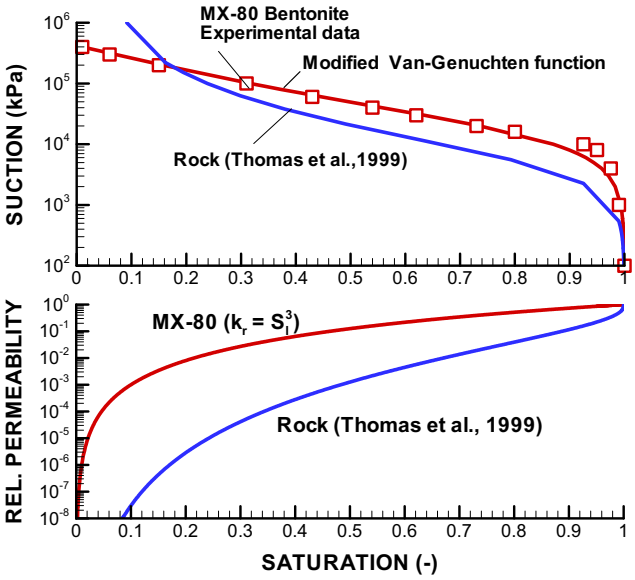

Figure B-1. Water-retention and relative-permeability functions assigned to the bentonite buffer and the surrounding rock. The red squares are experimental values measured on a small sample of MX-80 bentonite, whereas the lines indicate the functions used in the modeling.

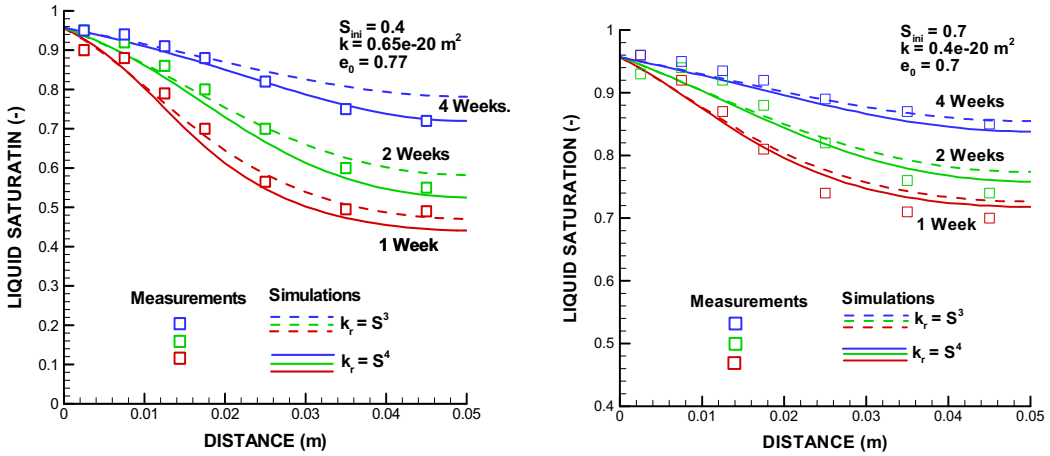

Figure B-2. Results from modeling of water uptake test

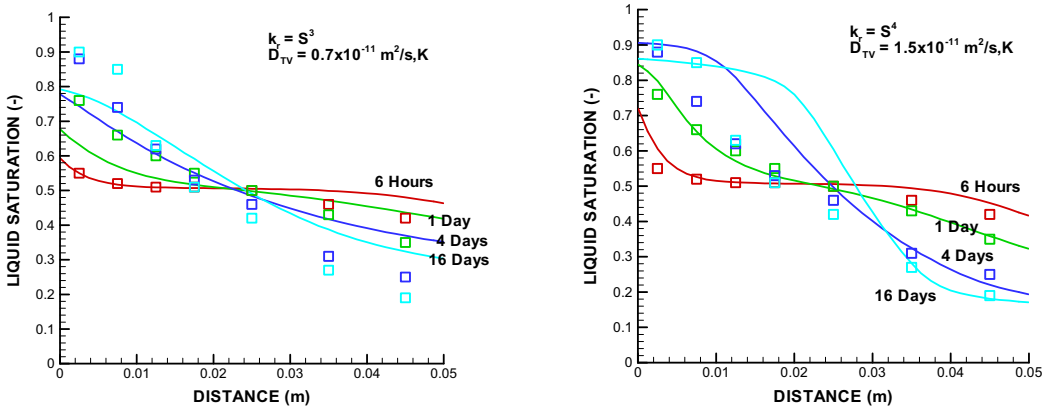

Figure B-3. Results of modeling of thermal gradient test using Börgesson-Hernelind (1999) empirical function for D_{Tv}.

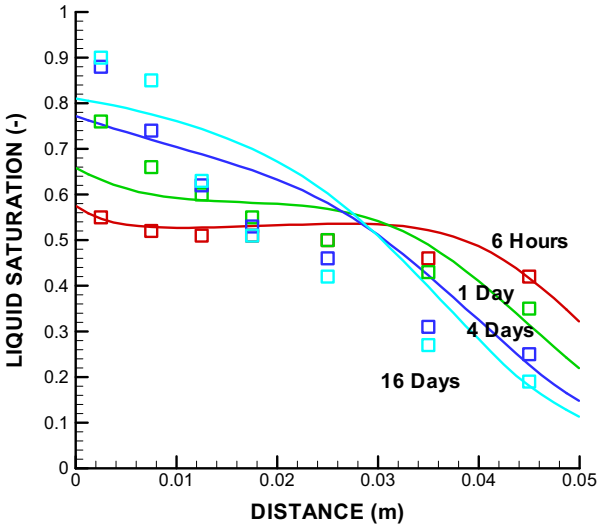

Figure B-4. Results of modeling of thermal gradient test using ROCMAS original D_{TV} functions defined by Equations (B-6) and (B-7). A tortuosity factor of 1.0 and $f_{tv} = 1.0$ are assumed in these simulations.

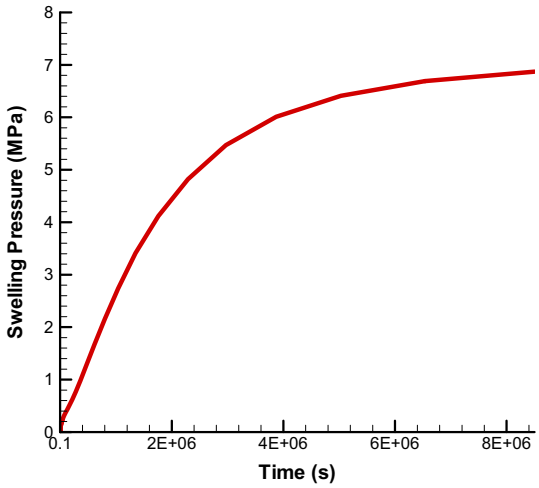

Figure B-5. Simulated swelling stress for a water uptake test in a confined chamber.

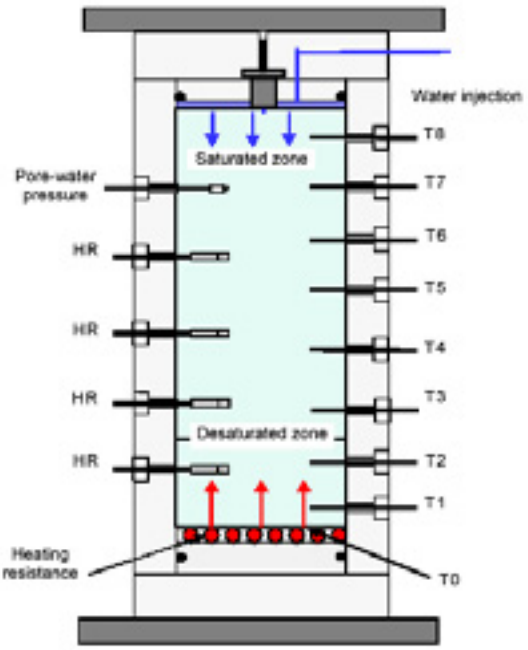

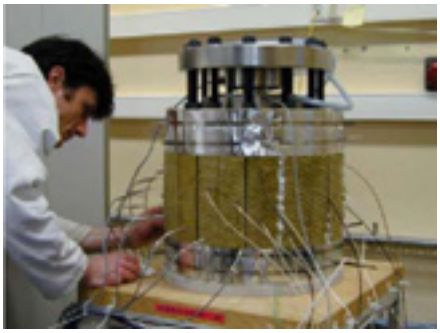

Measurements of temperature, relative humidity, radial and axial stress during heating and infiltration

Figure B-6. Layout of CEA mock-up test on MX-80 bentonite (Catabin and Billaud, 2005).

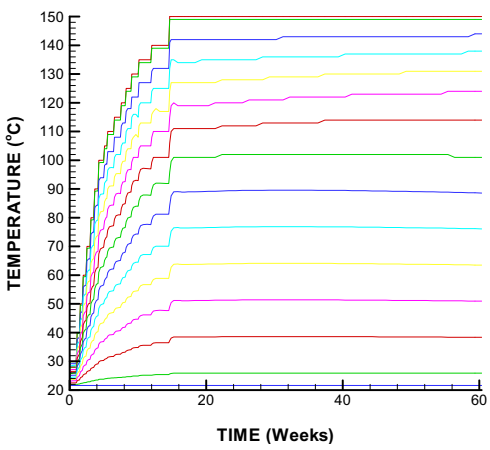

(a) Temperature for Cell 1

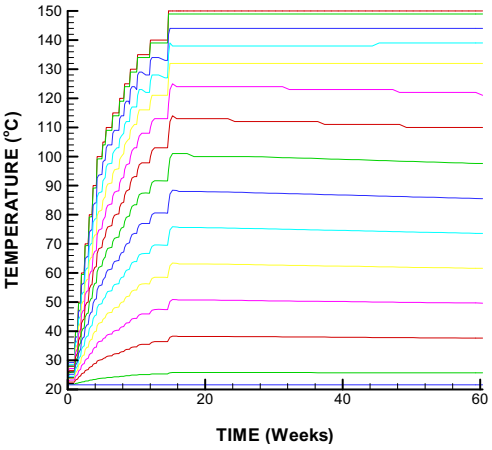

(b) Temperature for Cell 2

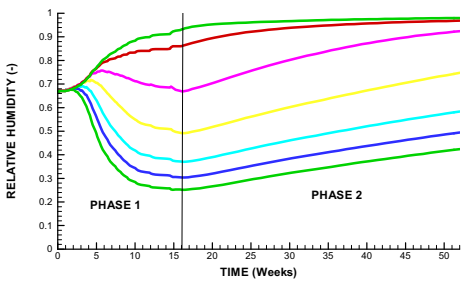

(c) Saturation for Cell 1

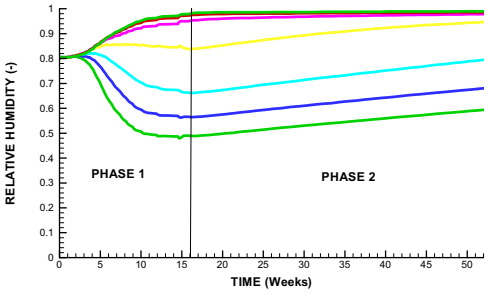

(d) Saturation for Cell 2

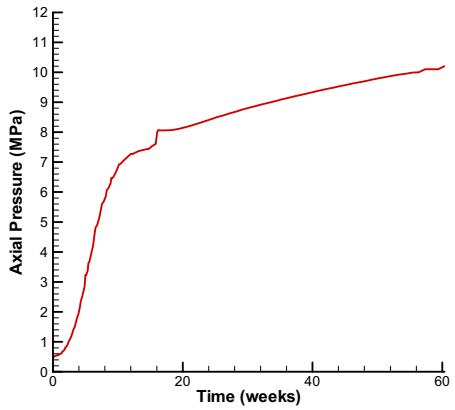

(e) Axial stress for Cell 1

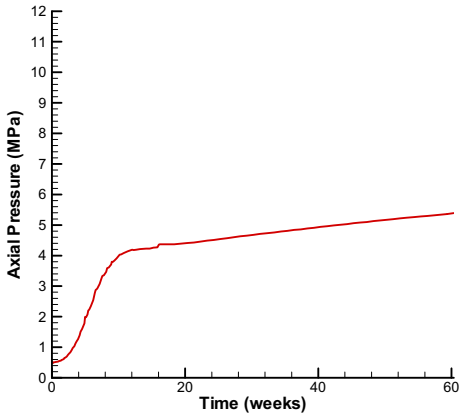

(f) Axial stress for Cell 2.

Figure B-7. Simulated results of CEA mock-up test using ROCMAS

www.ski.se

STATENS KÄRNKRAFTINSPEKTION
Swedish Nuclear Power Inspectorate

POST/POSTAL ADDRESS SE-106 58 Stockholm
BESÖK/OFFICE Klarabergsviadukten 90
TELEFON/TELEPHONE +46 (0)8 698 84 00
TELEFAX +46 (0)8 661 90 86
E-POST/E-MAIL ski@ski.se
WEBBPLATS/WEB SITE www.ski.se